

5. VELOCITY STRUCTURE OF THE LOWER OCEANIC CRUST: RESULTS FROM HOLE 735B, ATLANTIS II FRACTURE ZONE¹

Gerardo J. Iturrino², Benoit Ildefonse³, and Greg Boitnott⁴

ABSTRACT

Laboratory compressional wave (V_p) and shear wave (V_s) velocities were measured as a function of confining pressure for the gabbros from Hole 735B and compared to results from Leg 118. The upper 500 m of the hole has a V_p mean value of 6895 m/s measured at 200 MPa, and at 500 meters below seafloor (mbsf), V_p measurements show a mean value of 7036 m/s. V_s mean values in the same intervals are 3840 m/s and 3857 m/s, respectively. The mean V_p and V_s values obtained from log data in the upper 600 m are 6520 and 3518 m/s, respectively. These results show a general increase in velocity with depth and the velocity gradients estimate an upper mantle depth of 3.32 km. This value agrees with previous work based on dredged samples and inversion of rare element concentrations in basalts dredged from the conjugate site to the north of the Atlantis Bank. Laboratory measurements show V_p anisotropy ranging between 0.4% and 8.8%, with the majority of the samples having values less than 3.8%. Measurements of velocity anisotropy seem to be associated with zones of high crystal-plastic deformation with predominant preferred mineral orientations of plagioclase, amphiboles, and pyroxenes. These findings are consistent with results on gabbros from the Hess Deep area and suggest that plastic deformation may play an important role in the seismic properties of the lower oceanic crust. In contrast to ophiolite studies, many of the olivine gabbros show a small degree of anisotropy. Log derived V_s anisotropy shows an average of 5.8% for the upper 600 m of Hole 735B and tends to decrease with depth where the overburden pressure and the age of the crustal section suggests closure of cracks and infilling of fractures by alteration

¹Iturrino, G.J., Ildefonse, B., and Boitnott, G., 2002. Velocity structure of the lower oceanic crust: results from Hole 735B, Atlantis II Fracture Zone. *In* Natland, J.H., Dick, H.J.B., Miller, D.J., and Von Herzen, R.P. (Eds.), *Proc. ODP, Sci. Results*, 176, 1–71 [Online]. Available from World Wide Web: <http://www-odp.tamu.edu/publications/176_SR/VOLUME/CHAPTERS/SR176_05.PDF>. [Cited YYYY-MM-DD]

²Borehole Research Group, Lamont-Doherty Earth Observatory of Columbia University, PO Box 1000, Route 9W, Palisades NY 10964, USA. iturrino@ldeo.columbia.edu

³Laboratoire de Tectonophysique, ISTEEM, CNRS UMR5568, Université Montpellier II, 34095 Montpellier, Cédex 5, France.

⁴New England Research, Inc., 76 Olcott Drive, White River Junction VT 05001, USA.

minerals. Overall the results indicate that the average shear wave splitting in Hole 735B might be influenced by preferred structural orientations and the average value of shear wave splitting may not be a maximum because structural dips are $<90^\circ$. The maximum fast-wave orientation values could be influenced by structural features striking slightly oblique to this orientation or by near-field stress concentrations. However, flexural wave dispersion analyses have not been performed to confirm this hypothesis or to indicate to what extent the near-field stresses may be influencing shear wave propagation. Acoustic impedance contrasts calculated from laboratory and logging data were used to generate synthetic seismograms that aid in the interpretation of reflection profiles. Several prominent reflections produced by these calculations suggest that Fe-Ti oxides and shear zones may contribute to the reflective nature of the lower oceanic crust. Laboratory velocity attenuation (Q) measurements from below 500 m have a mean value of 35.1, which is consistent with previous vertical seismic profile (VSP) and laboratory measurements on the upper 500 m.

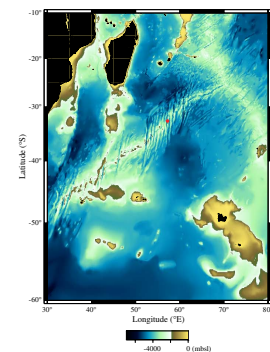
INTRODUCTION

Through the last three decades, one of the main scientific goals of both the Deep Sea Drilling Project (DSDP) and the more recent Ocean Drilling Program (ODP) has been to drill deep into the Earth to study the composition and structure of the lower oceanic crust and upper mantle. The return to Hole 735B during ODP Leg 176 resulted in the deepening of the previous depth of 500 meters below seafloor (mbsf), achieved during ODP Leg 118, to the deepest penetration of a lower oceanic crust segment ever accomplished, at 1508 mbsf. The 86.3% core recovery of gabbroic rocks achieved during both legs (Robinson, Von Herzen, et al., 1989; Dick, Natland, Miller, et al., 1999) provided an excellent opportunity to study lower crustal rocks analogous to ophiolitic sequences and assess the seismic nature of oceanic Layer 3. These combined drilling results make Hole 735B a significant accomplishment in understanding the nature of the oceanic crust because we are now able to describe the physical properties and the magmatic, structural, and metamorphic history of a block of the lower ocean crust that formed at a very slow-spreading ridge.

Site 735 is located at $32^\circ43.40'S$, $57^\circ16.00'E$ (Fig. F1) on the rift mountains along the eastern transverse ridge of the Atlantis II Fracture Zone, which is a 210-km-long left-lateral offset of the Southwest Indian Ridge (SWIR). At ~ 80 Ma, the SWIR became the western segment of the Indian Ocean triple junction as a direct result of the initial breakup of Gondwanaland (Norton and Sclater, 1979; Fisher and Sclater, 1983; Sclater et al., 1981; Tapscott et al., 1980). A subsequent northeastern migration of the triple junction created a series of transform systems that include the Atlantis II Fracture Zone. Since ~ 34 Ma, the spreading rate along the SWIR has been an ultra-slow half-rate of 0.8 cm/yr (Fisher and Sclater, 1983; Dick et al., 1991). This slow-spreading environment has caused segmented magmatic events that are responsible for along-strike changes in the structure and stratigraphy of the thin crustal sections in this area and provides excellent targets to drill deep crustal sections.

Hole 735B was drilled on a shoal platform, known as the Atlantis Bank, in ~ 700 m of water. It is believed that this platform, which is 5 km long in a north-south direction and 2 km wide, is part of a series of uplifted blocks that lie on a ridge parallel to the transform valley. These

Fig. F1. Location of Hole 735B, p. 23.



irregularly shaped blocks are defined by steep slopes attributed to normal faulting and may represent simple horsts uplifted relative to both the rift valley floor at which this crust originated and the adjacent oceanic crust to the east. Similar topographic features have been previously found in fracture zones and are commonly underlain by upper mantle and lower crustal rocks (Engel and Fisher, 1969, 1975; van Andel et al., 1971; Bonatti, 1978; Bonatti and Hamlyn, 1978; Bonatti and Crane, 1982; Karson and Dick, 1983). The age of the crust at this site, based on magnetic anomalies (Dick et al., 1991) and a zircon U-Pb isotopic age date (Stakes et al., 1991), is ~11.5 Ma.

The lithostratigraphic units recovered from Hole 735B (Fig. F2) are mainly metagabbros, olivine gabbros, gabbros, Fe-Ti oxide gabbros, gabbro-norites, and troctolitic gabbros (Robinson, Von Herzen, et al., 1989; Dick, Natland, Miller, et al., 1999). Several prominent shear zones are present, with the uppermost 40 m of the hole (Unit I) showing the most intense deformation, whereas the bottommost 900 m of the hole has significantly less deformation and a more uniform composition. The unusually high core recovery for the entire 1500-m section represents more igneous rock recovery than that on any previous DSDP or ODP leg. Therefore, this hole provides an unprecedented opportunity to determine the physical properties of the lower crust, calibrate results with compositional and structural variations, and refine previous models of the seismic stratigraphy of oceanic Layer 3.

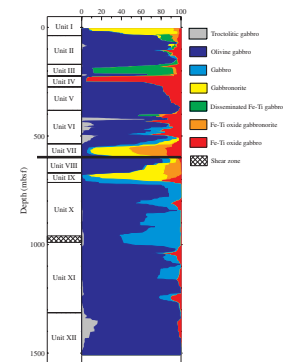
Here we present results from laboratory measurements from the entire section and downhole logging data from the upper 600 m of Hole 735B in an attempt to understand the factors controlling the seismic signature of the lower oceanic crust. Logging data are available only from the top 600 m because 1400 m of drilling pipe was lost during Leg 176 as a result of severe weather conditions, and only the upper 600 m of the hole was cleared of the obstruction prior to abandoning the site.

NATURE OF SEISMIC LAYER 3

In the past, the nature of the oceanic basement has been deduced mainly from studies of ophiolite complexes (Gass, 1968; Church and Stevens, 1971; Moores and Vine, 1971; Christensen and Salisbury, 1975; Karson et al., 1984), remote geophysical surveys, and studies made from dredged or cored samples from the ocean floor. During the last three decades, our knowledge of the oceanic seismic structure has improved dramatically from the simple three-layer model of Raitt (1956, 1963) that was based on first arrival information. Advances in shooting, recording, and wireline logging technology have provided the means to recognize subdivisions within oceanic Layers 2 and 3, which were first interpreted as horizontal layers of constant velocities (Hussong et al., 1969; Shor et al., 1969; Sutton et al., 1971; Fox et al., 1973; Lister and Lewis, 1974; Peterson et al., 1974; Houtz and Ewing, 1976). Furthermore, results from synthetic seismograms and inversion techniques suggested that the velocity structure of the oceanic crust may be more accurately described in terms of velocity gradients instead of constant velocity layers (Helmberger and Morris, 1969; Kennett and Orcutt, 1976; Orcutt et al., 1977; Spudich and Orcutt, 1980).

Largely because of these studies, the igneous oceanic crust is typically thought of as comprising an upper crust (Layer 2) characterized by a rapid increase in seismic velocity with depth and a thicker lower crust (Layer 3) that is distinguished from Layer 2 by both a higher compres-

F2. Schematic diagram showing the lithostratigraphy of Hole 735B as a function of depth, p. 24.



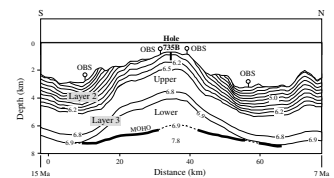
sional wave velocity and a much smaller vertical velocity gradient. However, a direct correlation between the seismic layering and the in situ lithologic and physical properties of the oceanic crust has never been established. The transition between seismic Layers 2 and 3 has been interpreted as a change in igneous rock textures from doleritic (diabase) sheeted dikes to gabbro, an increase in metamorphic grade from greenschist to amphibolite facies metamorphism (Christensen, 1970; Fox et al., 1973; Christensen and Salisbury, 1975; Salisbury and Christensen, 1978; Spudich and Orcutt, 1980), or a change in crustal bulk porosity with depth (Lort and Matthews, 1972; Spudich and Orcutt, 1980; Becker, 1985). Recent interpretations of seismic refraction studies on the southern flank of the Costa Rica Rift have proposed that the seismic Layer 2/3 boundary is located within the sheeted dike complex (Detrick et al., 1994). This interpretation correlates with gradual downward changes in crustal porosity and alteration, with no apparent association with the lithologic transition from the sheeted dikes to gabbro.

Seismic reflection studies (Mutter et al., 1985; McCarthy et al., 1988; Géli and Renard, 1994) have shown that the structure of the North Atlantic oceanic crust is more complex than the previously mentioned layered model. Studies from ocean basins reveal a close interplay between brittle faulting in the upper crust and magmatism and intrusion at depth. These reflection profiles show basement-cutting faults that in some instances can be traced downdip into packages of laminated high-amplitude reflections confined within 1 s of the Moho reflection. In some cases, these deeper reflection packages dip as much as 20° to 40° and thicken downward before terminating abruptly at the subhorizontal Moho reflection, whereas in other instances they penetrate through what appears to be the upper mantle. It has been suggested (Mutter et al., 1985; McCarthy et al., 1988) that although the lower crustal events can be interpreted as downdip equivalents of basement-cutting faults, their high amplitudes and laminated character may be a result of constructive interference through a package of interlayered mafic-ultramafic cumulates crystallized along the walls of the magma chamber at the time of crustal accretion. Furthermore, the apparent continuation of upper crustal faults into these layered sets of mafic-ultramafic material suggests a spatial correlation between faulting and magmatism.

In the proximity of Hole 735B, seismic refraction measurements (Muller et al., 1997) found an overall crustal thickness north and south of Atlantis Bank of 4 km and Layer 2 having a normal thickness of ~2 km (Fig. F3). However, a projection from a seismic line 1 km to the west of the Atlantis Bank shows that beneath this area, the depth to the Moho is 5 ± 1 km below seafloor (Fig. F3). In contrast, dredged samples (Dick et al., 1991) and inversion of rare element concentrations in basalts dredged from the conjugate site to the north of the Atlantis Bank (Muller et al., 1997) suggest a crustal thickness of 3 ± 1 km.

The results from Hole 735B provide the opportunity to test these hypotheses and models using downhole and physical properties measurements. Although several attempts to drill and log deep into the oceanic crust have been previously made (Kirkpatrick, 1979; Salisbury et al., 1980; Salisbury, 1983; Cann and Von Herzen, 1983; Salisbury et al., 1985), this potential was more fully realized in results from Hole 735B, DSDP Hole 504B in the Costa Rica Rift, and the findings from the Hess Deep area during Leg 147.

F3. P-wave seismic velocity model, p. 25.



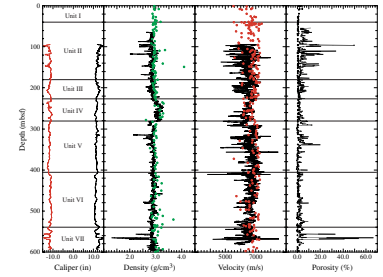
LABORATORY MEASUREMENTS

Crack porosity, composition, density, alteration, and mineral orientation are the most important factors responsible for significant variations in seismic velocities. A comparison between downhole logs and laboratory physical properties measurements obtained at atmospheric pressure shows a favorable correlation between the two types of data (Fig. F4). This correspondence is mainly attributed to the newer generation of logging tools (Dick, Natland, Miller, et al., 1999) used during Leg 176 for the downhole measurements and the higher data quality produced. In spite of these results, velocities at in situ pressures are often quite different from measurements at atmospheric pressure (Birch, 1960; Iturrino et al., 1991); therefore, it is important that velocity data used for crustal studies be obtained at elevated pressures. For example, seismic anisotropy can originate from either preferred mineralogical alignments or structural features.

For this study, compressional wave (V_p) and shear wave (V_s) velocities were measured at the New England Research Laboratories (see “Appendix,” p. 21) using the pulse transmission method (Birch, 1960; Christensen, 1965, 1985) under hydrostatic conditions up to confining pressures of 200 MPa. The upper pressure limit was chosen because previous experiments on Leg 118 samples (Iturrino et al., 1991) have shown that this upper limit minimizes the effects of cracks on velocities by closing the intergranular pore spaces and fracture openings, thus giving information on preferred mineral orientation in the oceanic crust. In many cases, microcracks develop by releasing the in situ stresses when the samples are brought to the surface from deep crustal sections (Iturrino et al., 1995). The 200-MPa limit also equates to the approximate in situ pressure of the lower oceanic crust in a more traditional 6-km section. V_p , V_s , and seismic attenuation measurements from core data are presented in Table T1, and the methods are described in “Appendix,” p. 21.

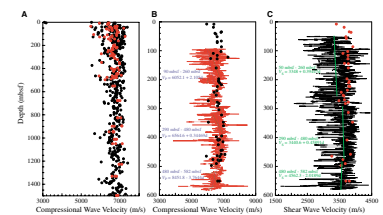
A comparison between atmospheric pressure compressional wave velocity values and in situ pressure measurements show some discrepancies. For this comparison, only measurements made in the same samples were used, in situ pressures were estimated from the effect of the water column, changes in pressure with depth due to the overburden rock column were estimated, and velocity values between velocity vs. pressure intervals were interpolated. In most instances, atmospheric pressure measurements display higher velocity values than those obtained from high-pressure measurements (Fig. F5A). Common measurements made in the upper 500 m (48 total samples) show that the average compressional wave velocity at atmospheric pressure is 6760 ± 387 m/s, whereas the average V_p for the in situ measurements is 6602 ± 279 m/s. Below 500 m, the average V_p at atmospheric pressure for eight samples is 6659 ± 212 m/s and 6820 ± 154 m/s for the in situ pressure measurements. Velocity discrepancies in the upper 500 m of the hole may be due to (1) difficulties in picking first arrivals on deformed and altered samples at atmospheric pressures, where in many cases, the first break is not sharp and may lead to earlier time picks or (2) a faulty calibration of the old velocity system used during Leg 118. Below 600 m, the atmospheric pressure velocity values seem to be more reliable as they are lower than in situ measurements. A comparison of the in situ pressure compressional wave velocity (Fig. F5B) and shear wave velocity measurements (Fig. F5C) with log data in the upper 600 m shows a bet-

F4. Caliper, compressional wave velocity, bulk density, and porosity logs as a function of depth, p. 26.



T1. Index properties, compressional wave and shear wave velocities, attenuation, mineralogy, and deformation information, p. 42.

F5. Compressional wave and shear wave velocity as a function of depth, p. 27.



ter correlation between the two types of data. A compressional wave velocity gradient for the entire set of in situ measurements is defined by

$$V_p = 6554.5 + 0.24833d \text{ with } R = 0.34,$$

where d represents the depth in mbsf.

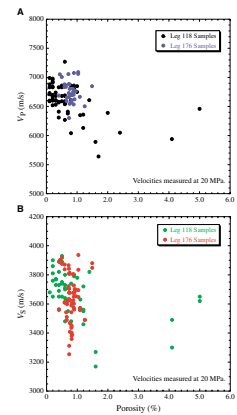
As with all shallow oceanic drill holes, fracture porosity is a major factor influencing the velocity structure of Hole 735B. Compressional wave velocity measurements obtained at low pressures indicate that there is a decrease in seismic velocities with increasing crack porosity for the gabbros of Hole 735B (Fig. F6A). However, compressional wave velocities do not show a strong relationship for porosity values >1%. The samples from Leg 176 do not show as large a range in porosities as the samples from shallower in the section, possibly because of bias sampling, or more likely, because porosity generally decreases with depth. However, velocities are still significantly affected by the closure of microcracks as the velocity vs. pressure data indicate (Table T1). Shear wave velocity measurements show that porosity has a similar effect on V_s (Fig. F6B); however, the overall result is diminished and the differences may be due to structural influences as previously described (Iturrino et al., 1991).

Anisotropy

Anisotropy is becoming more important in the interpretation of oceanic seismic data (Shor et al., 1973; Stephen, 1981; White and Whitmarsh, 1984; Shearer and Orcutt, 1985, 1986). For this study, variations in compressional wave velocities and shear wave splitting are examined in detail. In ideal cases, there are two simple styles of alignment in earth materials (horizontal and vertical), and laboratory studies suggest that they give rise to two types of anisotropy. In the horizontal style, or layered case, elastic properties may vary vertically, such as from layer to layer, but not horizontally. Such a material is called transversely isotropic with a vertical axis of symmetry. Waves generally travel faster horizontally, along layers, than vertically. The simplest case of the second type of anisotropy corresponds to a material with aligned vertical weaknesses such as cracks or fractures, or with unequal horizontal stresses. Elastic properties vary in the direction crossing the fractures but not along the plane of the fracture. Such a material is called transversely isotropic with a horizontal axis of symmetry or azimuthal anisotropy. Waves traveling along the fracture direction (but within the competent rock) generally travel faster than waves crossing the fractures.

Laboratory velocity measurements can assess the effects of both types of symmetry on anisotropy by careful sampling along the orientations of planes of weakness (see "Appendix," p. 21), especially when shear waves are measured. However, in a borehole, the maximum shear wave splitting is controlled by transverse isotropy with a horizontal axis of symmetry although, as in most cases with dipping structures, anisotropy can still result from a nonhorizontal symmetry axis where a maximum anisotropy could not be obtained. In the sections below, an assessment of compressional wave velocity anisotropy and shear wave splitting is provided for laboratory and downhole measurements.

F6. Effect of crack porosity on both compressional wave and shear wave velocities, p. 28.



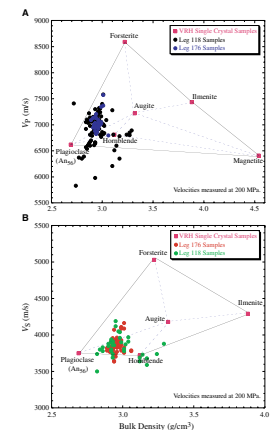
Compressional Wave Velocities

The core samples from Leg 176 have a mean compressional wave velocity of 7036 ± 161 m/s measured at 200 MPa. This value is higher than the 6895 ± 307 m/s mean value of the upper 500 m of Hole 735B (Iturrino et al., 1991). The consistently higher compressional wave velocity values below 500 m correspond to a general decreasing trend in alteration with depth (Dick, Natland, Miller, et al., 1999) as well as a decrease in Fe-Ti oxides and the abundance of olivine gabbros (Fig. F2).

Even though most oceanic rocks contain large percentages of highly anisotropic minerals, they tend to be isotropic or nearly isotropic because of the random orientation of their main mineral constituents. Velocities for a mineral aggregate with a random orientation can be calculated from the minerals' elastic constants. Voigt (1928) and Reuss (1929) averages assume uniform strain and stress, respectively, and give high and low limits for the aggregate velocity. Commonly, the Voigt-Reuss-Hill average (VRH), which is the mean of the Voigt and Reuss averages (Hill, 1952), is used as the velocity for a monomineralic rock with random mineral orientation (Birch, 1961). The gabbros of Hole 735B with random mineral orientation should fall in a triangular field defined by the VRH averages of the main mineral constituents.

A velocity-density plot at 200 MPa, shown in Figure F7A, indicates that the seismic properties of most of the samples from Hole 735B fall in a region controlled by the VRH averages for plagioclase (An_{56}), olivine, hornblende, and augite (Christensen, 1982). The samples that fall outside of these limits are those which show the highest degree of deformation at the top of the section (Iturrino et al., 1991). At 200 MPa, Leg 176 samples show a very small amount of V_p anisotropy that ranges from 0.4% to 8.8%, with the majority of the samples having values less than 3.8% (Table T1). Compressional wave velocities were measured twice in the sample having the highest degree of V_p anisotropy (176-735B-142R-3, 86–88 h') and the results show a variation in anisotropy between 5.9% and 8.8%. Compositional variations between the individual samples from this core may explain the fact that velocity anisotropy is high while the samples plot within the VRH area defined by the main mineral constituents. This is evident by the 0.1 g/cm³ density difference between the samples (Table T1). Alteration can also cause deviations from the field defined by the VRH averages that will not be related to intrinsic anisotropic properties. Some of the samples from Leg 176 have a high degree of background alteration. However, in the majority of the cases, olivine and clinopyroxene are replaced by amphibole, and plagioclase is recrystallized as secondary plagioclase (Dick, Natland, Miller, et al., 1999). Therefore, the velocities from the main alteration mineral constituents should fall close within the limits defined by the VRH averages. Most of these results, in combination with thin section examinations of samples found in Units II through Unit XII, show either weak plastic deformation or random mineral orientation with distinct igneous textures (Dick, Natland, Miller, et al., 1999). Thus, these observations imply that there is no pervasive mineral orientation that would cause significant V_p anisotropy especially below 600 mbsf. These results differ from ophiolite studies where gabbros with abundant olivine show a strong preferred mineral orientation (Christensen, 1978; Salisbury and Christensen, 1978).

F7. Velocity and density relationship for samples from Hole 735B, p. 29.



Shear Wave Velocities

Most of the laboratory shear wave measurements fall in a similar VRH field defined by plagioclase, olivine, hornblende, and augite (Fig. F7B). However, when compared to the V_p vs. density plot, there is a shift to the field mostly dominated by plagioclase, hornblende, and augite. This shift may be due to either a lack of abundant VRH data that will constrain the V_s limits or to other factors besides compositional variations affecting V_s . Without complete thin section and chemical analyses, it is difficult to determine which one is the case. However, most of the Leg 176 samples have low V_s anisotropy values (Table T1), suggesting that they should fall within a field defined by the main mineral constituents. Samples that fall outside this field are mainly from the top of Hole 735B, where up to 7% V_s anisotropy has been previously recorded (Iturrino et al., 1991). In most cases, the V_s anisotropy was caused by a large degree of deformation in mylonitic zones (Fig. F8). Only one of the Leg 176 samples shows significant shear wave splitting (176-735B-142R-3, 86-88, h'). This sample does not have any visible fabric, but it is short, has a high velocity value, and contains large crystals that are nearly the length of the sample itself. Grain size may very well explain these variations in V_s as well as the observed V_p anisotropy.

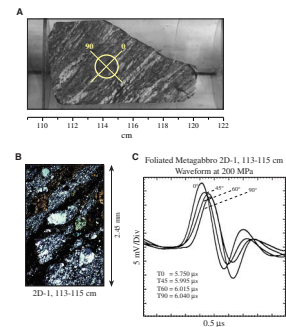
Seismic Wave Attenuation

Seismic wave attenuation (Q^{-1}) is a measure of the energy lost in a propagating wave through the conversion to frictional heat, also known as intrinsic attenuation, and extrinsic effects such as scattering. Intrinsic effects are generally attributed to loss of energy that decays exponentially in both frequency and propagation distance due to intergranular fluid flow associated with the propagation of an elastic wave (Kuster and Toksöz, 1974; Toksöz et al., 1979; Wepfer and Christensen, 1989; Goldberg et al., 1992). Scattering losses are the result of formation heterogeneities (Aki and Richards, 1980; Richards and Menke, 1983).

Computed values of Q_p , Q_{S1} , and Q_{S2} for each sample are presented in Table T1 for compressional waves and two orthogonal shear waves (S1 and S2). Computations were performed following the method of Toksöz et al. (1979) and are briefly described in "Appendix," p. 21. The results are reported for increasing confining pressures of 60, 100, 150, 200 MPa and a decreasing pressure interval of 60 MPa. Overall, most of these results fall within the range of previously reported values obtained at Hole 735B from laboratory and logging data (Goldberg et al., 1991, 1992; Swift and Stephen, 1992). Leg 176 samples with $Q \leq 100$ at 200 MPa have a mean Q_p value of 35.1 ± 20.1 (Table T2) compared to values of 32 ± 29 from previous laboratory work (Goldberg et al., 1991, 1992). Q values calculated from analyses of spectral ratios and amplitude decay on seismograms from the VSP experiment performed during Leg 118 range from 3 to 26 (Swift and Stephen, 1992). The values of Q_{S1} and Q_{S2} have averages of 22 ± 12.7 and 21 ± 7.9 (Table T2).

The agreement with the previously reported laboratory and log values from the top of the hole (Goldberg et al., 1991, 1992; Swift and Stephen, 1992) suggests that there is a general uniform trend in Q for this entire 1500-m section of lower oceanic crust. This is further emphasized by the Q_p values from 1497 mbsf, which range from 8.5 to 23.5 (Table T1). Overall, the Leg 176 samples also show a general trend of in-

F8. Deformation in mylonitic zones, p. 30.



T2. Statistical analyses of Q_p , Q_{S1} , and Q_{S2} measurements, p. 70.

creasing Q with confining pressure (Table T1), suggesting that the closure of microcracks is influencing the overall attenuation values. Some of the samples within an individual core exhibit a large amount of Q_p anisotropy between vertical and horizontal measurements that do not necessarily correspond to large variations in velocity or Q_s (Fig. F9). In addition, several samples have Q values greater than 100. These values may indicate some variations with depth; however, some degree of caution should be used particularly when measuring Q in short and fast samples such as these. The procedure assumes that losses and waveform distortions due to geometric spreading and coupling between the sample and core-holder are identical for the reference material and each sample. Potentially significant problems arise due to variations in sample length and impedance, as well as poorly understood coupling phenomena, which are observed to be pressure dependent even for high Q standards such as aluminum. Observed amplitude spectra are also not always consistent with the underlying assumption of a constant Q material because of evidence of significant disruption of the waveforms due to scattering and sample heterogeneities.

DOWNHOLE MEASUREMENTS

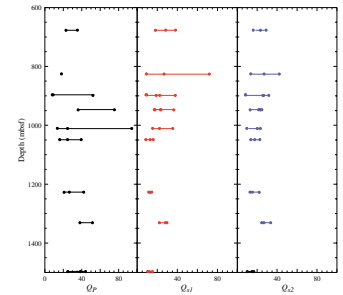
Density, Compressional Wave Velocity, and Porosity

As previously shown in Figure F4, high-quality logging data from the upper 600 m of Hole 735B were obtained during Leg 176. In the upper 600 m of Hole 735B, density values range from 1.47 to 3.27 g/cm³, with a mean value for the entire logged section of 2.88 ± 0.14 g/cm³. Low values are related to fractures filled with seawater, especially at the top and bottom of the logged interval. The olivine gabbros of Unit V exhibit a range of values from 2.25 to 2.98 g/cm³, with a mean of 2.88 g/cm³, whereas the oxide gabbros of Unit IV show a range of values from 2.95 to 3.27 g/cm³, with a mean of 3.09 g/cm³. Variations in the density profile mostly correspond to variations in oxide mineralogy (Fig. F2) and increases in porosity (Fig. F4).

The porosity measurements in the same interval show variations between 0.03% and 57.37%, with a mean value for the entire section of $3.2\% \pm 5.2\%$. High values generally correspond to fractures and correlate with low peaks in the density log. Several isolated zones corresponding to high porosity and low density occur in the upper 450 m of the hole and were previously documented as high permeability zones from results of Packer experiments (Robinson, Von Herzen, et al., 1989). Below 450 mbsf, several zones showing a decrease in density and an increase in porosity are apparent, especially between 555 and 570 mbsf. This interval has been identified as a zone bounded by two faults.

The sonic logs recorded with the Dipole Sonic Imager (DSI) tool represent the first use of this tool in a lower oceanic crust environment and the first set of good-quality sonic data in Hole 735B. The logs were processed postcruise using a Baker Atlas software package for processing the compressional, shear, and Stoneley waveforms. Compressional wave and shear wave results are presented here. V_p has a mean value of 6520 ± 418 m/s, and variations correlate well with changes in both porosity and density measurements. An apparent low-velocity, low-density zone at the top of lithostratigraphic Unit V, which also correlates with high-porosity and caliper readings (Dick, Natland, Miller, et

F9. Diagram showing variations in Q_p , Q_{S1} , and Q_{S2} vs. depth in Hole 735B below 600 m, p. 31.



al., 1999), is responsible for the reflector identified during Leg 118 at this depth (Swift et al., 1991). In general, V_p gradients increase with depth (Fig. F5B) except for the bottommost 100 m of the logged interval. The sharpest increase is observed between 90 and 260 mbsf as deformation decreases downhole. Between 290 and 480 mbsf, the velocities are high and relatively constant. Below 480 mbsf, there is a decreasing trend in velocities marked by the presence of large fractures and increase deformation. The velocity gradient for the entire logged section is defined by $V_p = 6373 + 0.43016d$ with $R = 0.15$. A more complete analysis will be discussed in the following sections.

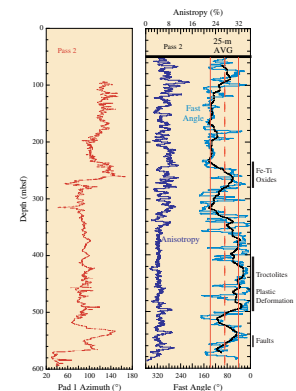
Shear Wave Velocities

The deployment of the DSI tool in Hole 735B also marked the first opportunity to measure high-resolution shear wave velocity and V_s anisotropy profiles in a lower oceanic basement environment. The DSI utilizes a directional source and receivers. The dipole source behaves much like a piston, creating a pressure increase on one side of the hole and a decrease on the other. This causes a small flexing of the borehole wall, which directly excites compressional and shear waves in the formation. Propagation of this flexural wave is coaxial with the borehole, whereas displacement is at right angles to the borehole axis and in line with the transducer. The source operates at low frequencies, usually below 4 kHz, where excitation of these waves is optimal.

The DSI tool can record fast and slow shear waves when the x-dipole mode is selected prior to deployment (see “Appendix,” p. 21). Using the software package from Baker Atlas, data from Hole 735B were analyzed for orientation and degree of anisotropy indicated by the amount of birefringence. After identifying the fast and slow directions, quality curves ($S1_{ISO}$ and $S2_{ISO}$) were used for the anisotropy estimate ($S1_{ISO}/S2_{ISO}$) and the anisotropy azimuth ($S1S2$). The relative difference between the $s1/s2$ residue error ($s1$ and $s2$ are the fast shear wave and slow shear wave polarization angles, respectively) and the wave data-fitting residue error for an isotropic formation is $S1_{ISO}/S2_{ISO}$. The bigger this value, the higher the confidence in the estimated anisotropy. In determining the anisotropy azimuth, the $s1$ angle is determined as the one whose wave data residue error is the smallest. If, however, the $s1$ error minimum is comparable to the $s2$ minimum, it is difficult to determine which is the fast angle and which is the slow orientation. Therefore, the relative difference between the $s1$ and $s2$ residue errors gives a quality indicator for the determined $s1$ angle and it is stored in the $S1S2$ curve. The bigger this ratio, the more reliable the $s1$ angle. Caliper curves (Fig. F4) were also used for determining borehole enlargements and assessing data quality. For more details, refer to “Appendix,” p. 21.

The V_s profile shows average velocities slightly increasing with depth from 50 to 260 mbsf (Fig. F5C). The interval from 290 to 480 mbsf also shows a slight increase with depth although average velocities are higher than the previous interval (Fig. F5C). Similar to the V_p profile, the V_s gradients show a general decrease in the bottommost 100 m of the logged interval. The average velocity gradient for the entire logged section is defined by $V_s = 3353.5 + 0.43139d$ with $R = 0.17$. The velocity analyses based on DSI data also show a mean shear wave velocity of 3518 ± 393 m/s and an average V_s anisotropy of 5.8% for the upper 600 m of Hole 735B (Fig. F10). V_s anisotropy tends to decrease with depth

F10. Downhole logs showing the FMS pad 1 azimuth, the fast angle azimuth, and the average anisotropy, p. 32.



where the overburden pressure and the age of the crustal section suggests closure of cracks and infilling of fractures by alteration minerals.

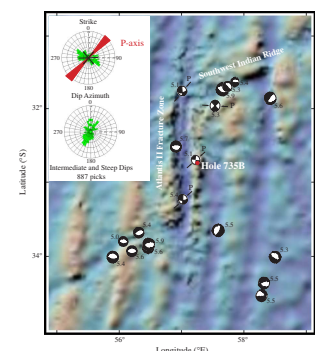
The fast-angle azimuth and the average anisotropy determined from DSI analyses also show some interesting results. The mean orientation of the fast-angle azimuth for the entire logged section of Hole 735B is 89° and the maximum and minimum standard deviation values of a 20 point average curve are 138° and 40° , respectively, in what appears to be a bimodal distribution (Fig. F10). The maximum fast-angle azimuth tends to be 138° to an approximate depth of 245 mbsf (Fig. F10). Below this depth, the results show more scatter and an average minimum fast-angle azimuth of 40° from north. Large variations in fast-angle azimuth are also observed in lithostratigraphic Unit IV (from 224 to 272 mbsf). However, the pad 1 azimuth orientation of the Formation MicroScanner (FMS) tool tends to indicate that the magnetization of this Fe-Ti oxide-rich unit may be affecting the orientation of these measurements at this particular interval.

Several factors could be contributing to the observed anisotropy. As discussed earlier, the maximum shear wave splitting in a borehole is controlled by transverse isotropy with a horizontal axis of symmetry or from a nonhorizontal symmetry axis where a maximum anisotropy could not be obtained. V_p anisotropy and shear wave splitting has been observed in laboratory velocity measurements because of preferred mineral orientations in isolated intervals. However, laboratory samples do not take into account the effects of large oriented fractures that may be contributing to the observed variations, especially steep (60° – 90°) to intermediate (30° – 60°) dipping fractures. In addition, stress concentrations can influence the velocity field in the vicinity of the borehole. A recent study of dipole anisotropy measurements (Winkler et al., 1998) has shown that in both experimental and theoretical cases, stress concentrations affect the velocity field around the borehole and consequently, dipole anisotropy measurements. In a borehole, low frequency flexural waves will have a relatively deep penetration; therefore, they will be sensitive to the far-field stresses. In contrast, waves traveling at higher frequencies will be primarily sensitive to near-field stress concentrations because of their shallow penetration depth, and the fast dipole direction will be aligned perpendicular to the far-field maximum stress.

In an attempt to assess the nature of shear wave splitting in Hole 735B, the average, maximum, and minimum fast-wave orientations were compared to the strike of steep and intermediate dipping foliations and fractures that were obtained from the interpretation of FMS images. Most of the fracture dip azimuths have a bimodal distribution in a conjugate set geometry with dips to the south and north (Fig. F11). In addition, focal mechanisms and earthquake magnitudes (M_w) based on the Harvard Centroid Moment Tensor (CMT) solutions (Cornell University GIS Group, 1998) were used to determine the effect of stress concentrations near the borehole.

The results show that the average fast-wave orientation (88°) correlates with the general strike of steep and intermediate dipping structures (Fig. F11). CMT solutions show that three significant strike-slip events have been recorded along the Atlantis II Fracture Zone, with one of the events being in the near vicinity of Hole 735B (Fig. F11). The estimated orientation of the compressional axis for the three events show that the maximum and minimum fast-angle shear wave orientation are approximately perpendicular and parallel to the earthquake P-axis (Fig. F11). The overall results indicate that the average shear wave splitting

F11. Bathymetric map showing the Atlantis II Fracture Zone and surrounding area, p. 33.



in Hole 735B might be influenced by preferred structural orientations and the average value of shear wave splitting may not be a maximum because most dips are $<90^\circ$. Structural features slightly oblique to the maximum fast-wave orientation or near-field stress concentrations could influence the maximum fast-wave orientation values. However, flexural wave dispersion analyses have not been performed to confirm this hypothesis or to indicate to what extent the near-field stresses may be influencing shear wave propagation. At this time, the minimum fast-wave orientation is more difficult to explain because there is no clear indication that preferred structural orientations or stress concentrations are influencing shear wave propagation in this direction. The possibility exists that because anisotropy decreases below 325 mbsf, the DSI velocity analyses have difficulties distinguishing between the fast and slow orientations when the difference between the two is small. However, because the difference between the fast and slow is $>90^\circ$, further analyses need to be performed to fully explain this orientation.

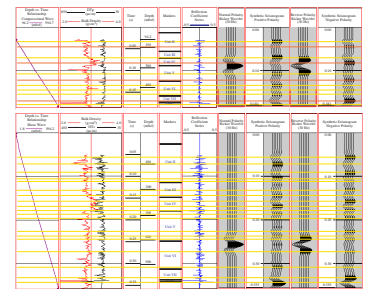
CORE-LOG INTEGRATION

The integration of core and log data has become increasingly important to understand the parameters controlling the seismic nature of the oceanic crust. For this reason, we constructed V_p and V_s synthetic seismograms from the Leg 176 logging data (Fig. F12) and compared the results with previously published synthetic seismograms constructed with core data and VSP results (Iturrino and Christensen, 1991; Swift et al., 1991).

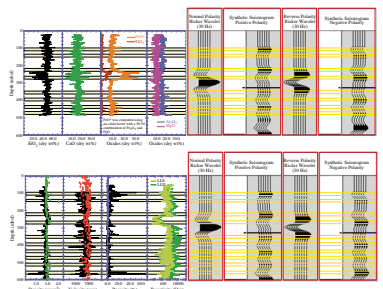
For refraction and reflection studies of the oceanic crust, the frequencies of air gun and explosive sources generally range from 5 to 30 Hz. Synthetic seismograms were calculated using compressional wave and shear wave data obtained with the DSI, the Leg 176 density log, and 30-Hz Ricker wavelets (Ricker, 1953). When calculating both synthetic seismograms using one-dimensional modeling, we assumed that our layered models persisted laterally over distances of a Fresnel zone. Assuming an average velocity of 6520 m/s and a 30-Hz source at a depth of 300 mbsf, the radius of a Fresnel zone would be 117 m. This value falls within the calculated range for the radius of a Fresnel zone obtained with VSP experiments in Hole 735B (Swift et al., 1991). Also, field observations of the well-explored Samail ophiolite plutonic section show that some layer sets can be traced along the strike in northern Oman for distances of ~ 10 km (Pallister and Hopson, 1981). These values and observations, in combinations with wavelengths of 217 and 117 m for the V_p and V_s synthetic seismograms, respectively, suggest the possibility of having laterally continuous igneous and metamorphic units in Hole 735B that can be imaged seismically.

The synthetic seismograms produced with compressional wave velocities show several prominent reflections at approximately 94, 213, 265, and 555 mbsf and several other low-amplitude events located at approximately 137, 343, 380, 425, 462, and 502 mbsf (Fig. F12). The reflection at 94 mbsf is associated with an ~ 20 -m-thick interval characterized by changes in porosity, density, velocity, and composition (Fig. F13). This zone is bounded by high-density and -porosity Fe-Ti oxide intervals with low velocities and SiO_2 , MgO, and Al_2O_3 contents (Fig. F11). The reflections at 213 and 265 mbsf are also produced by a combination of compositional changes associated with Fe-Ti oxides and variations in density and velocity (Fig. F11). The event at 555 mbsf is

F12. Compressional wave and shear wave synthetic seismograms from logging data collected during Leg 176, p. 34.



F13. Correlation between the compressional wave synthetic seismograms and the geochemical, density, velocity, porosity, and resistivity logs obtained in Hole 735B during Legs 118 and 176, p. 36.



associated with a fractured zone where two faults have been identified. The lower-amplitude reflections are related to compositional changes in SiO₂, CaO, and Al₂O₃ content and porosity that seem to affect the compressional wave velocities. Compressional wave synthetic seismograms were also constructed using lower frequency Ricker (10 Hz) and Ormsby (low cut = 2 Hz, low pass = 5 Hz, high pass = 15 Hz, and high cut = 20 Hz) wavelets. The results showed smaller amplitude reflections that correlate with the results from Units II, IV, V, and VII (Fig. F12). The shear wave synthetic seismogram (Fig. F10) shows prominent reflections located at the same depths as those observed in the compressional wave reflection profile, but overall, a more detailed profile was produced due to the shorter wavelengths. This synthetic seismogram seems to be more sensitive to smaller variations in the velocity and density profiles.

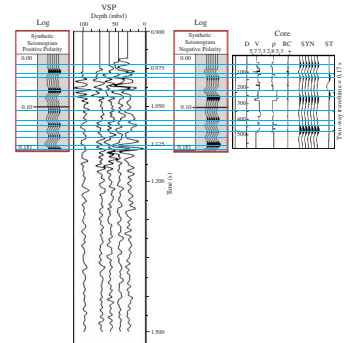
A comparison between the compressional wave synthetic seismograms constructed with the Leg 176 logs and those records from the Leg 118 VSP experiment (Robinson, Von Herzen, et al., 1989; Swift et al., 1991) and laboratory data-derived synthetics seismograms (Iturrino and Christensen, 1991) shows very good agreement between the different types of data (Fig. F14). The normal-polarity log-derived synthetic seismogram correlates well with the top five VSP stacks, especially at depths of 94, 213, 265, and 555 mbsf. The correlation between the weaker reflectors and the VSP data is not as clear because the amplitudes of some reflections in the VSP profiles are not coherent for all receiver depths. It has been suggested that the difficulties in tracing events across the VSP sections may be due in part to phase shifting caused by clipping of the air gun data, interference from the ship, pipe noises when the receiver was clamped close to the bottom-hole assembly, waveform distortion from the applied filters, or differences in power received at different borehole depths (Swift et al., 1991).

The similarities between the core and log synthetic seismograms are remarkable (Fig. F14) considering that the core-derived synthetic seismogram was produced for a 40-layer model with ~100 discrete density and velocity measurements over a 500-m interval. All the prominent reflectors observed in the upper 500 m of Hole 735B of the reversed-polarity log-derived synthetic seismogram correlate with the core data. In addition, a reflector in the core synthetic seismogram at a depth of 55 mbsf seems to correlate with the VSP data. This reflection may indicate the transition between the mylonites and porphyroclastic metagabbros of Unit I into the olivine and olivine-bearing gabbros of Unit II.

SUMMARY AND CONCLUSIONS

During the last few decades, drilling results and geophysical studies have demonstrated that the structural and compositional complexity of the oceanic crust is far greater than that of a simplistic three-layer seismic model. Porosity is a significant contributor to the velocity profile of the upper oceanic crust. Results from Hole 504B show velocities increasing with depth as a direct result of a decrease in porosity (Dick, Erzinger, Stokking, et al., 1992). Consequently, the reflectivity of the top of the sheeted dikes is mainly associated with changes in porosity. For the most part, the overall porosity trend in Hole 735B tends to decrease with depth except for fault zones located at 555 and 570 mbsf. However, high-porosity intervals at the top of the hole and these faulted intervals below show that porosity also plays an important role in the reflectivity of this lower crustal section. In addition, laboratory studies

F14. Correlation between Leg 176 synthetic seismograms produced with logging data collected during Leg 176 and VSP results from the experiment carried out during Leg 118, p. 38.



have shown that cracks tend to reduce laboratory seismic velocities at low pressures even though the porosities for most samples are on the order of tenths of a percent. The same effect has been observed in gabbros from the Hess Deep area (Iturrino et al., 1996), thus emphasizing the need for high-pressure laboratory measurements for comparison with in situ log measurements and seismic records. At higher pressures, laboratory velocity measurements are primarily related to mineralogy. For the most part, low velocities in Hole 735B are attributed to either the presence of Fe-Ti oxides, variations in SiO₂ content, or fractures. The presence of alteration products (i.e., phyllosilicates) in the upper part of Hole 735B also lowers seismic velocities (Iturrino et al., 1991); however, this does not seem to be the case in the bottom 1000 m, where compressional wave velocities remain relatively high, with an average of 7036 ± 161 m/s (Table T3).

The compressional wave velocity gradient based on log data for the upper 600 m of Hole 735B shows that the depth to the upper mantle would be 3.32 km. This calculation is based on a upper mantle velocity of 7800 m/s that was obtained from *P*-wave seismic velocity models based on ocean-bottom seismometer (OBS) data (Fig. F3). The same depth can be obtained using the shear wave velocity gradient for the entire logged section and an upper mantle velocity ($V_s = 4785$ ms) consistent with ophiolite results (Christensen, 1978; Salisbury and Christensen, 1978). These results are consistent with observations from dredged samples (Dick et al., 1991) and inversion of rare element concentrations in basalts dredged from the conjugate site to the north of the Atlantis Bank (Muller et al., 1997) that suggest a crustal thickness of 3 ± 1 km. Using the V_p gradient from in situ laboratory measurements, a depth to the upper mantle of 5.02 km/s is obtained. These depth estimates are closer to the seismic velocity models from Muller et al. (1997) than the results from the logging data. However, because laboratory measurements do not take into account the effects of large fractures on velocity and the seismic models are based on projections that are 1 km west of this area, the estimates from the logging data seem to be more typical of in situ conditions in the Atlantis Bank.

Five prominent reflectors in the synthetic seismograms compare favorably with a VSP section and lithologic variations found in the drill core recovered from Hole 735B. The first reflection, located at a depth of 55 mbsf, appears to correlate with the first reflection on the core-derived synthetic seismogram and the boundary between the foliated metagabbros of Unit I and the olivine-bearing gabbros of Unit II. The second and third reflection sequences appear to mark the top and bottom of the Fe-Ti oxide gabbros of Unit IV and correlate with reflections at these depths in the synthetic seismogram caused by marked changes in density and velocity. The contact between Units IV and V, which may be responsible for the third reflection sequence, is characterized by the presence of mylonitic Fe-Ti oxide gabbros and brecciated gabbros overlying a thick sequence of olivine gabbros. The fourth reflection package is not as clear as the previous sequences but may correspond to the interlayered olivine gabbros, troctolites, altered gabbros, and mylonites found in Unit VI. A seismic reflection between 400 and 475 mbsf in the synthetic seismogram may explain this event. Finally, the last event is attributed to fault zones characterized by high porosity values.

Isolated shear zones also seem to play a very important role in the hydrological and seismological properties as well as in the mineralogical composition of the oceanic crust. As shown in the synthetic seismo-

T3. Average core and log measurements, Hole 735B, p. 71.

grams (Fig. F13), high-porosity, low-velocity features and fairly strong seismic reflectors characterize these shear zones. They also serve as pathways for hydrothermal circulation causing rock alteration that generally produces lower seismic velocities than those in the surrounding unaltered crust. These changes in physical properties allow such shear zones to be imaged seismically and they are strong candidates for producing lower crustal dipping reflectors as those imaged in the Mid-Atlantic Ridge (McCarthy et al., 1988). A fairly good correlation between compositional variations, reflection synthetic seismogram models, and the VSP section for Hole 735B suggests that the reflectivity of the lower oceanic crust may be caused by a combination of deformation and intrusive events. Plastic deformation and mineral orientation due to regional stresses and intrusive events, such as the Fe-Ti oxide sill found in Unit IV, seem to have had a significant effect in the reflectivity of Hole 735B and may very well represent important events along the tectonic evolution of the lower oceanic crust found throughout the ocean basins. Thus, the layering and mineral orientation associated with ductile deformation at the top of magma chambers may also be responsible for the lower crustal reflections observed in seismic sections of the oceanic crust (McCarthy et al., 1988; Becker et al., 1989).

Shear waves have proved to be a powerful tool for studying the properties of the oceanic crust. Several highly deformed samples have shown a large degree of shear wave splitting due to preferred mineral orientations of plagioclase, amphiboles, and pyroxenes along highly deformed intervals. These findings, which are consistent with results of gabbros from the Hess Deep area (Iturrino et al., 1996), suggest that plastic deformation may play an important role on the seismic properties of the lower oceanic crust. The fast-angle azimuth and the average anisotropy determined from DSI analyses also show that, at least on the borehole scale, shear wave splitting may be influenced by preferred structural orientations and that the average value of shear wave anisotropy may not be a maximum because the structures are dipping $<90^\circ$. In addition, shear wave analyses may have the potential for determining the orientation of predominant near-field stresses.

Finally, most of the Q measurements from Hole 735B are consistent with previous VSP results and measurements in samples from the upper 500 m of the hole. Seismic estimates of Q from refraction studies in oceanic crust indicate high attenuation values ($Q_p < 100$) in the topmost 500 m of the crust, whereas Layer 3 has yielded Q values of ~ 300 (Vera et al., 1990), which is 1–2 orders of magnitude higher than the majority of the values reported here. Several samples from the bottom 1000 m of Hole 735B have values in this range (Table T1). This may indicate a less altered, more homogeneous section that may be representative of large portions of the lower oceanic environments. However, experimental limitations may require more intensive laboratory work to determine the effects of scattering and sample heterogeneities on Q .

ACKNOWLEDGMENTS

The authors will like to thank the Sedco and ODP staff of Leg 176 for their hard work and dedication. Dr. David Goldberg (LDEO) and Dr. Gilles Guerin (LDEO) provided many insightful discussions on the subject of physical properties of crystalline rocks. Mr. Howard Glassman (Baker-Atlas) and Mr. Doug Patterson (Baker-Atlas) provided their time and facilities for guiding Dr. Iturrino in the processing of the DSI data.

Dr. Roy Wilkins, Dr. Richard Von Herzen, and an anonymous reviewer improved the quality of this manuscript with their invaluable comments. This research used samples provided by the Ocean Drilling Program (ODP). ODP is sponsored by the U.S. National Science Foundation (NSF) and participating countries under management of Joint Oceanographic Institutions (JOI), Inc. Funding for this research was provided by a USSSP Site Augmentation proposal (OCE-9320477) and a post-cruise USSSP proposal (#F000779).

REFERENCES

- Aki, K., and Richards, P.G., 1980. *Quantitative Seismology Theory and Methods* (Vol. 2): San Francisco (W.H. Freeman).
- Becker, K., 1985. Large-scale electrical resistivity and bulk porosity of the oceanic crust, Deep Sea Drilling Project Hole 504B, Costa Rica Rift. In Anderson, R.N., Honnorez, J., Becker, K., et al., *Init. Repts. DSDP*, 83: Washington (U.S. Govt. Printing Office), 419–427.
- Becker, K., Sakai, H., Adamson, A.C., Alexandrovich, J., Alt, J.C., Anderson, R.N., Bideau, D., Gable, R., Herzig, P.M., Houghton, S.D., Ishizuka, H., Kawahata, H., Kinoshita, H., Langseth, M.G., Lovell, M.A., Malpas, J., Masuda, H., Merrill, R.B., Morin, R.H., Mottl, M.J., Pariso, J.E., Pezard, P.A., Phillips, J.D., Sparks, J.W., and Uhlig, S., 1989. Drilling deep into young oceanic crust, Hole 504B, Costa Rica Rift. *Rev. Geophys.*, 27:79–102.
- Birch, F., 1960. The velocity of compressional waves in rocks to 10 kilobars, 1. *J. Geophys. Res.*, 65:1083–1102.
- , 1961. The velocity of compressional waves in rocks to 10 kilobars, 2. *J. Geophys. Res.*, 66:2199–2224.
- Bonatti, E., 1978. Vertical tectonism in oceanic fracture zones. *Earth Planet. Sci. Lett.*, 37:369–379.
- Bonatti, E., and Crane, K., 1982. Anomalously old uplifted crust near oceanic transforms: result of oscillatory spreading. *Eos, Trans., Am. Geophys. Union*, 63:1100. (Abstract).
- Bonatti, E., and Hamlyn, P.R., 1978. Mantle uplifted block in the western Indian Ocean. *Science*, 201:249–251.
- Cann, J.R., and Von Herzen, R.P., 1983. Downhole logging at Deep Sea Drilling Project Sites 501, 504, and 505, near the Costa Rica Rift. In Cann, J.R., Langseth, M.G., Honnorez, J., Von Herzen, R.P., White, S.M., et al., *Init. Repts. DSDP*, 69: Washington (U.S. Govt. Printing Office), 281–300.
- Christensen, N.I., 1965. Compressional-wave velocities in metamorphic rocks at pressures to 10 kilobars. *J. Geophys. Res.*, 70:6147–6164.
- , 1970. Composition and evolution of the oceanic crust. *Mar. Geol.*, 8:139–154.
- , 1978. Ophiolites, seismic velocities, and oceanic crustal structure. *Tectonophysics*, 47:131–157.
- , 1982. Seismic velocities. In Carmichael, R.S. (Ed.), *Handbook of Physical Properties of Rocks* (Vol. 2): Boca Raton, FL (CRC Press), 1–228.
- , 1985. Measurements of dynamic properties of rocks at elevated temperatures and pressures. In Pincus, H.J., and Hoskins, E.R. (Eds.), *Measurements of Rock Properties at Elevated Pressures and Temperatures*. Spec. Tech. Publ.—ASTM, 869:93–107.
- Christensen, N.I., and Salisbury, M.H., 1975. Structure and constitution of the lower oceanic crust. *Rev. Geophys. Space Phys.*, 13:57–86.
- Church, W.R., and Stevens, R.K., 1971. Early Paleozoic ophiolite complexes of the Newfoundland Appalachians as mantle-oceanic crust sequences. *J. Geophys. Res.*, 76:1460–1466.
- Cornell University GIS Group, 1998. *CMT Seismicity Catalog and Focal Mechanisms*. [Online]. Available from World Wide Web: <<http://atlas.geo.cornell.edu>>. [Cited 2001-06]
- Coyner, K.B., 1984. Effects of stress, pore pressure, and pore fluids on bulk strain, velocity, and permeability in rocks [Ph.D. dissert.]. MIT, Cambridge, MA.
- Detrick, R., Collins, J., and Swift, S., 1994. *In situ* evidence for the nature of the seismic layer 2/3 boundary in oceanic crust. *Nature*, 370:288–290.
- Dick, H.J.B., Erzinger, J., Stokking, L.B., et al., 1992. *Proc. ODP Init. Repts.*, 140: College Station, TX (Ocean Drilling Program).

- Dick, H.J.B., Natland, J.H., Miller, D.J., et al., 1999. *Proc. ODP, Init. Repts.*, 176 [CD-ROM]. Available from: Ocean Drilling Program, Texas A&M University, College Station, TX 77845-9547, U.S.A.
- Dick, H.J.B., Schouten, H., Meyer, P.S., Gallo, D.G., Bergh, H., Tyce, R., Patriat, P., Johnson, K.T.M., Snow, J., and Fisher, A., 1991. Tectonic evolution of the Atlantis II Fracture Zone. *In* Von Herzen, R.P., Robinson, P.T., et al., *Proc. ODP, Sci. Results*, 118: College Station, TX (Ocean Drilling Program), 359–398.
- Engel, C.G., and Fisher, R.L., 1969. Lherzolite, anorthosite, gabbro and basalt dredged from the Mid-Indian Ocean Ridge. *Science*, 166:1136–1141.
- , 1975. Granitic to ultramafic rock complexes of the Indian Ocean Ridge system, western Indian Ocean. *Geol. Soc. Am. Bull.*, 86:1553–1578.
- Fisher, R.L., and Sclater, J.G., 1983. Tectonic evolution of the southwest Indian Ocean since the mid-Cretaceous: plate motions and stability of the pole of Antarctica/Africa for at least 80 Myr. *Geophys. J. R. Astron. Soc.*, 73:553–576.
- Fox, P.J., Schreiber, E., and Peterson, J.J., 1973. The geology of the oceanic crust: compressional wave velocities of oceanic rocks. *J. Geophys. Res.*, 78:5155–5172.
- Gass, I.G., 1968. Is the Troodos Massif, Cyprus, a fragment of Mesozoic ocean floor? *Nature*, 220:39–42.
- Géli, L., and Renard, V., 1994. Ocean crust formation processes at very slow spreading centers: model for the Mohns Ridge, near 72°N, based on magnetic, gravity, and seismic data. *J. Geophys. Res.*, 99:2995–3013.
- Goldberg, D., Badri, M., and Wepfer, W., 1991. Ultrasonic attenuation measurements in gabbros from Hole 735B. *In* Von Herzen, R.P., Robinson, P.T., et al., *Proc. ODP, Sci. Results*, 118: College Station, TX (Ocean Drilling Program), 253–260.
- , 1992. Acoustic attenuation in oceanic gabbro. *Geophys. J. Int.*, 111:193–202.
- Helmberger, D.V., and Morris, G.B., 1969. A travel time and amplitude interpretation of a marine refraction profile: primary waves. *J. Geophys. Res.*, 74:483–494.
- Hill, R., 1952. The elastic behavior of a crystalline aggregate. *Proc. Phys. Soc. London, Sect. A*, 65:349–354.
- Houtz, R., and Ewing, J., 1976. Upper crustal structure as a function of plate age. *J. Geophys. Res.*, 81:2490–2498.
- Hussong, D.M., Nowroozi, A.A., Odegard, M.E., and Sutton, G.H., 1969. Crustal structure under an ocean bottom seismometer using explosive sources. *Eos, Trans., Am. Geophys. Union*, 50:644. (Abstract).
- Iturrino, G.J., and Christensen, N.I., 1991. Reflectivity modeling of the layer 3 gabbroic sequence drilled at the Atlantis II Fracture Zone. *In* Von Herzen, R.P., Robinson, P.T., et al., *Proc. ODP, Sci. Results*, 118: College Station, TX (Ocean Drilling Program), 245–252.
- Iturrino, G.J., Christensen, N.I., Becker, K., Boldreel, L.O., Harvey, P.H.K., and Pezard, P., 1995. Physical properties and elastic constants of upper crustal rocks from core-log measurements in Hole 504B. *In* Erzinger, J., Becker, K., Dick, H.J.B., and Stokking, L.B. (Eds.), *Proc. ODP, Sci. Results*, 137/140: College Station, TX (Ocean Drilling Program), 273–292.
- Iturrino, G.J., Christensen, N.I., Kirby, S., and Salisbury, M.H., 1991. Seismic velocities and elastic properties of gabbroic rocks from Hole 735B. *In* Von Herzen, R.P., Robinson, P.T., et al., *Proc. ODP, Sci. Results*, 118: College Station, TX (Ocean Drilling Program), 227–244.
- Iturrino, G.J., Miller, D.J., and Christensen, N.I., 1996. Velocity behavior of lower crustal and upper mantle rocks from a fast-spreading ridge at Hess Deep. *In* Mével, C., Gillis, K.M., Allan, J.F., and Meyer, P.S. (Eds.), *Proc. ODP, Sci. Results*, 147: College Station, TX (Ocean Drilling Program), 417–440.
- Karson, J.A., Collins, J.A., and Casey, J.F., 1984. Geologic and seismic velocity structure of the crust/mantle transition in the Bay of Islands ophiolite complex. *J. Geophys. Res.*, 89:6126–6138.
- Karson, J.A., and Dick, H.J.B., 1983. Tectonics of ridge-transform intersections at the Kane Fracture Zone. *Mar. Geophys. Res.*, 6:51–98.

- Kennett, B.L.N., and Orcutt, J.A., 1976. A comparison of travel time inversions for marine refraction profiles. *J. Geophys. Res.*, 81:4061–4070.
- Kirkpatrick, R.J., 1979. The physical state of the oceanic crust: results of downhole geophysical logging in the Mid-Atlantic Ridge at 23°N. *J. Geophys. Res.*, 84:178–188.
- Kuster, G.T., and Toksöz, M.N., 1974. Velocity and attenuation of seismic waves in two-phase media, Part II: experimental results. *Geophysics*, 39:607–618.
- Lister, C.R.B., and Lewis, B.T.R., 1974. An ocean bottom seismometer suitable for arrays. *Eos, Trans., Am. Geophys. Union*, 55:357. (Abstract).
- Lort, J.M. and Matthews, D.H., 1972. Seismic velocities measured in rocks of the Troodos igneous complex. *J. R. Astron. Soc.*, 27:383–392.
- McCarthy, J., Mutter, J.C., Morton, J.L., Sleep, N.H., and Thompson, G.A., 1988. Relic magma chamber structures preserved within the Mesozoic North Atlantic crust? *Geol. Soc. Am. Bull.*, 100:1423–1436.
- Moore, E.M., and Vine, F.J., 1971. The Troodos Massif, Cyprus, and other ophiolites as oceanic crust: evaluation and implications. *Philos. Trans. R. Soc. London, Ser. A*, 268:443–466.
- Muller, M.R., Robinson, C.J., Minshull, R.S., and Bickle, M.J., 1997. Thin crust beneath Ocean Drilling Program Borehole 735B at the Southwest Indian Ridge? *Earth Planet. Sci. Lett.*, 148:93–107.
- Mutter, J.C., and North Atlantic Transect (NAT) Study Group, 1985. Multichannel seismic images of the oceanic crust's internal structure; evidence for a magma chamber beneath the Mesozoic Mid-Atlantic Ridge. *Geology*, 13:629–632.
- Norton, I.O., and Sclater, J.G., 1979. A model for the evolution of the Indian Ocean and the breakup of Gondwanaland. *J. Geophys. Res.*, 84:6803–6830.
- Orcutt, J.A., Dorman, L.M., and Spudich, P.K.P., 1977. Inversion of seismic refraction data. In Heacock, J.G. (Ed.), *The Earth's Crust*. Am. Geophys. Union, Geophys. Monogr. Ser., 20:371–384.
- Pallister, J.S., and Hopson, C.A., 1981. Samail ophiolite plutonic suite: field relations, phase variation, cryptic variation and layering, and a model of a spreading ridge magma chamber. *J. Geophys. Res.*, 86:2593–2644.
- Peterson, J.J., Fox, P.J., and Scriber, E., 1974. Newfoundland ophiolites and the geology of the oceanic layer. *Nature*, 247:194–196.
- Raitt, R.W., 1956. Seismic refraction studies of the Pacific Ocean basin. *Bull. Geol. Soc. Am.*, 67:1623–1640.
- , 1963. The crustal rocks. In Hill, M.N. (Ed.), *The Sea—Ideas and Observations on Progress in the Study of the Seas* (Vol. 3): *The Earth Beneath the Sea*: New York (Wiley-Interscience), 85–102.
- Reuss, A., 1929. Berechnung der Fließgrenze von Mischkristallen auf Grund der Plastizitätsbedingung für Einkristalle, *Z. Agnew. Math. Mech.*, 9:49–54.
- Richards, P.G., and Menke, W., 1983. The apparent attenuation of a scattering medium. *Bull. Seismol. Soc. Am.*, 73:1195–2021.
- Ricker, N., 1953. The form and laws of propagation of seismic wavelets. *Geophysics*, 18:10–40.
- Robinson, P.T., Von Herzen, R., et al., 1989. *Proc. ODP, Init. Repts.*, 118: College Station, TX (Ocean Drilling Program).
- Salisbury, M.H., 1983. Basement logs from the mouth of the Gulf of California, Deep Sea Drilling Project Leg 65. In Lewis, B.T.R., Robinson, P., et al., *Init. Repts. DSDP*, 65: Washington (U.S. Govt. Printing Office), 329–342.
- Salisbury, M.H., and Christensen, N.I., 1978. The seismic velocity structure of a traverse through the Bay of Islands ophiolite complex, Newfoundland, an exposure of oceanic crust and upper mantle. *J. Geophys. Res.*, 83:805–817.
- Salisbury, M.H., Christensen, N.I., Becker, K., and Moos, D., 1985. The velocity structure of Layer 2 at Deep Sea Drilling Project Site 504 from logging and laboratory experiments. In Anderson, R.N., Honnorez, J., Becker, K., et al., *Init. Repts. DSDP*, 83: Washington (U.S. Govt. Printing Office), 529–539.

- Salisbury, M.H., Donnelly, T.W., and Francheteau, J., 1980. Geophysical logging in Deep Sea Drilling Project Hole 417D. *In* Donnelly, T., Francheteau, J., et al., *Init. Repts. DSDP*, 51, 52, 53 (Pt. 1): Washington (U.S. Govt. Printing Office), 705–713.
- Sclater, J.G., Fisher, R.L., Patriat, P., Tapscott, C., and Parsons, B., 1981. Eocene to recent development of the Southwest Indian Ridge: a consequence of the evolution of the Indian Ocean Triple Junction. *Geophys. J. R. Astron. Soc.*, 64:587–604.
- Shearer, P., and Orcutt, J.A., 1985. Anisotropy in the oceanic lithosphere—theory and observations from Ngendei seismic refraction experiment in the southwest Pacific. *Geophys. J. R. Astron. Soc.*, 80:493–526.
- , 1986. Compressional- and shear-wave anisotropy in the oceanic lithosphere—the Ngendei seismic refraction experiment. *Geophys. J. R. Astron. Soc.*, 87:967–1003.
- Shor, G.G., Jr., Menard, H.W., and Raitt, R.W., 1969. Regional observations: the structure of the Pacific basin. *In* Maxwell, A.E. (Ed.), *The Sea—Ideas and Observations on Progress in the Study of the Seas* (Vol. 4): *New Concepts of Sea Floor Evolution*: New York (Wiley-Interscience), 2–27.
- Shor, G.G., Jr., Raitt, R.W., Henry, M., Bently, L.R., and Sutton, G.H., 1973. Anisotropy and crustal structure of the Cocos Plate. *Geofis. Int.*, 13:337–362.
- Spudich, P., and Orcutt, J.A., 1980. Petrology and porosity of an oceanic crust site: results from waveform modeling of seismic refraction data. *J. Geophys. Res.*, 85:1409–1433.
- Stakes, D., Mével, C., Cannat, M., and Chaput, T., 1991. Metamorphic stratigraphy of Hole 735B. *In* Von Herzen, R.P., Robinson, P.T., et al., *Proc. ODP, Sci. Results*, 118: College Station, TX (Ocean Drilling Program), 153–180.
- Stephen, R.A., 1981. Seismic anisotropy observed in the oceanic crust. *Geophys. Res. Lett.*, 8:865–868.
- Sutton, G.H., Maynard, G.L., and Hussong, D.M., 1971. Wide-spread occurrence of a high-velocity basal layers in the Pacific crust found with repetitive sources and sonobuoys. *In* Heacock, J.G. (Ed.), *The Structure and Physical Properties of the Earth's Crust*. Am. Geophys. Union, Geophys. Monogr. Ser., 14:193–209.
- Swift, S.A., Hoskins, H., and Stephen, R.A., 1991. Seismic stratigraphy in a transverse ridge, Atlantis II Fracture Zone. *In* Von Herzen, R.P., Robinson, P.T., et al., *Proc. ODP, Sci. Results*, 118: College Station, TX (Ocean Drilling Program), 219–226.
- Swift, S.A. and Stephen, R.A., 1992. How much gabbro is in ocean seismic layer 3? *Geophys. Res. Lett.*, 19:1871–1874.
- Tapscott, C.R., Patriat, P., Fisher, R.L., Sclater, J.G., Hoskins, H., and Parsons, B., 1980. The Indian Ocean triple junction. *J. Geophys. Res.*, 85:4723–4739.
- Toksöz, M.N., Johnston, D.H., and Timur, A., 1979. Attenuation of seismic waves in dry and saturated rock: I. Laboratory measurements. *Geophysics*, 44:681–690.
- van Andel, T.H., Von Herzen, R.P., and Phillips, J.D., 1971. The Vema fracture zone and the tectonics of transverse shear zones in oceanic crustal plates. *Mar. Geophys. Res.*, 1:261–283.
- Vera, E., Mutter, J., Buhl, P., Orcutt, J., Harding, A.J., Kappus, M.E., Deitrick, R.S., and Brocher, T.M., 1990. The structure of 0- to 0.2-my-old oceanic crust at 9°N on the East Pacific Rise from expanded spread profiles. *J. Geophys. Res.*, 95:15529–15556.
- Voigt, W., 1928. *Lehrbuch der Kristallphysik*: Leipzig (B.G. Teulner).
- Wepfer, W.W., and Christensen, N.I., 1989. Q anisotropy in metamorphic rocks. *Eos, Trans., Am. Geophys. Union*, 70:458. (Abstract).
- White, R.S., and Whitmarsh, R.B., 1984. An investigation of seismic anisotropy due to cracks in the upper oceanic crust at 45°N, Mid-Atlantic Ridge. *Geophys. J. R. Astron. Soc.*, 79:439–467.
- Winkler, K.W., Sinha, B.K., and Plona, T.J., 1998. Effects of borehole stress concentrations on dipole anisotropy measurements. *Geophysics*, 63:11–17.

APPENDIX

Methodology

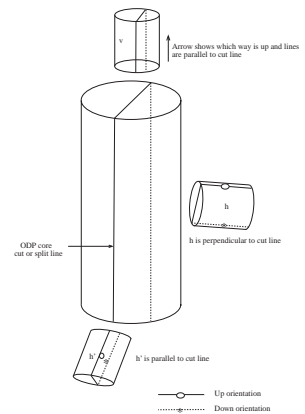
Wet and dry sample weights and volumes were determined for the calculation of porosity as well as bulk and grain densities. After measuring the wet weights, samples were dried at 110°C for a period of 24 hr to drive off water.

Velocity measurements were made at pressures up to 200 MPa by placing the samples in a core holder that consisted of two titanium end pieces. Each end piece houses a stacked plumbum (lead) zirconate titanate ceramic composite transducer containing a compressional and two orthogonally polarized shear elements. The ultrasonic compressional wave and shear waves were sequentially generated from one stack and received by the other stack, and the resulting waveforms recorded with a digital oscilloscope for processing. First arrivals were picked manually and travel times were corrected for known delays in the titanium end pieces (Coyner, 1984). The samples were coupled to each end piece using a non-water soluble resin. Confining and pore pressures were controlled using two hydraulically servo-controlled intensifiers. The samples were hydrostatically loaded, being separated from the confining medium with a soft rubber jacket. Pore pressure access to the sample was made through a small port in one of the core holder end pieces. Pressure history and data collection for each experiment was identical for all tests, being controlled via computer using a predefined script.

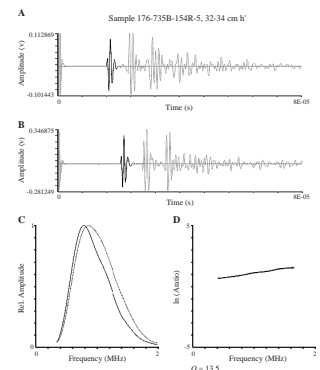
For vertical minicores, V_{s1} was polarized perpendicular to the cut face as shown in Figure AF1 and V_{s2} was always measured at 90° from V_{s1} . One exception is Sample 176-735B-96R-2 (54-58) v, for which the orientation markings were not clearly defined. However, this sample had a clear dipping fabric and S1 was oriented perpendicular to the strike of the fabric. In general, we had difficulties identifying fabrics in the cores, but since the cut face was made perpendicular to the strike of the fabric, the orientations are relatively good for all samples. For horizontal cores, V_{s1} was horizontally polarized and V_{s2} polarized vertically. A few of the horizontal cores were retested rotated 45° from vertical. Values for these types of measurements have a 45° note by the sample identifications in Table T1.

Ultrasonic compressional wave and shear wave Q values were computed using the procedure described by Toksöz et al. (1979). The procedure involves the comparison between the amplitude spectra of the measured waveforms and the spectra of reference waveforms measured on a high Q standard. Waveforms measured on a 2-in-long aluminum sample were used as the high Q reference. Reference waveforms were selected to match the pressure conditions of each measurement. All of the computations were performed using identical windowing parameters. A representative plot documenting the computations for each sample is shown in Figure AF2. In each plot, the entire recorded waveform, the windowed version that was used for the analysis, the reference waveform and its windowed version from a 2-in-long aluminum sample are shown. The amplitude spectra of the waveforms for the standard and the sample, the portion of the amplitude ratio versus frequency which was used for computing Q , and a line indicating the inferred slope are also represented.

AF1. Schematic diagram showing the orientation with respect to the ODP core system of the samples used for laboratory measurements, p. 39.



AF2. A representative plot documenting the computations for each sample, p. 40.



An example of the processed cross-dipole data from the upper 600 m of Hole 735B is shown in Figure AF3. Definitions of curves in the shear wave cross-dipole analyses are the following:

1. $S1_{ISO}/S2_{ISO}$: This curve is a quality control curve for the anisotropy estimate. There are two angles, one referring to the fast shear wave polarization (s1) and one referring to the slow shear wave polarization (s2). The angle associated with s1 has the smallest waveform fitting residue error ($S1_{ERR}$) as compared to the associated with s2 ($S2_{ERR}$). The relative difference between s1/s2 residue error and the wave data fitting residue error for an isotropic formation (ISO_{ERR}) is $S1_{ISO}/S2_{ISO}$. The bigger this value (though positive), the higher the confidence in the estimated anisotropy. Conversely, the smaller the $S1_{ISO}$ value, the lower the confidence. This means that modeling a formation as isotropic fits the data equally well as compared to modeling the formation as anisotropic. A quantitative definition is the following:

$$S1_{ISO} = [(S2_{ERR} - S1_{ERR}) / (S1_{ERR} + S2_{ERR})] \times 100\% \text{ and}$$

$$S2_{ISO} = [(ISO_{ERR} - S2_{ERR}) / (ISO_{ERR} + S2_{ERR})] \times 100\%.$$

2. $S1S2$: This curve is a quality control curve for the determined fast angle or anisotropy azimuth. The s1 angle is determined as the one with the smallest wave data fitting residue error. If, however, the s1 error minimum is comparable to the s2 minimum, it is difficult to determine which is the fast angle and which is the slow angle. Therefore, the relative difference between s1 and s2 residue errors gives a quality indicator for the determined s1 angle and it is accounted for in the $S1S2$ curve. The bigger this ratio, the more reliable the s1 angle. $S1S2$ is then defined as

$$S1S2 = [(S2_{ERR} - S1_{ERR}) / (S1_{ERR} + S2_{ERR})] \times 100\%.$$

AF3. Processed cross-dipole shear wave data, p. 41.

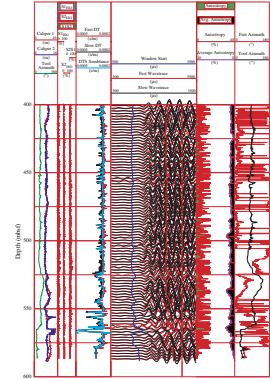


Figure F1. The location of Hole 735B on the Atlantis Bank of the Atlantis II Fracture Zone, Southwest Indian Ridge, is shown on the bathymetric map with a red dot.

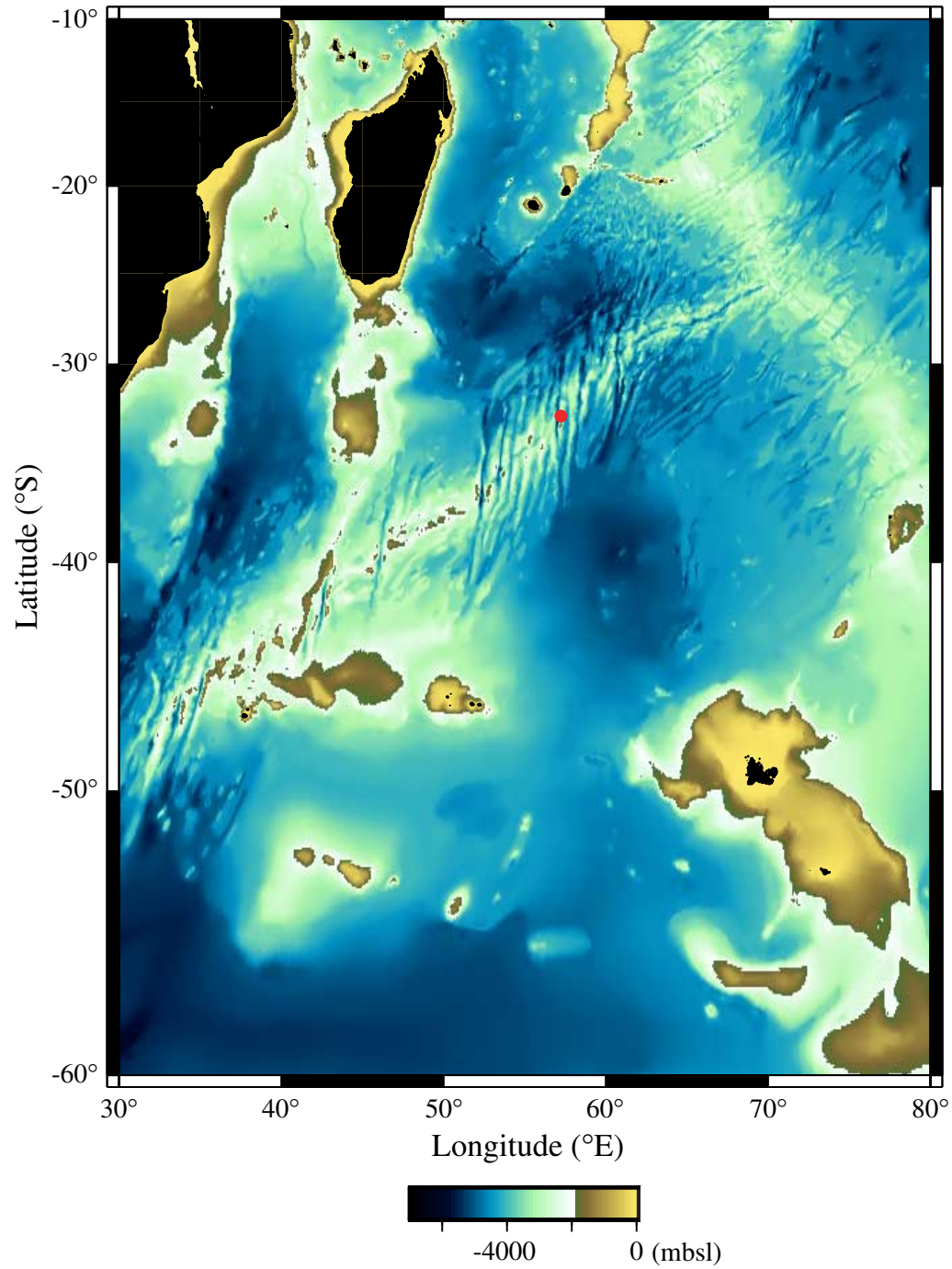


Figure F2. Schematic diagram showing the lithostratigraphy of Hole 735B as a function of depth. The black line at 600 mbsf indicates the approximate location of current hole obstruction and marks the bottom depth of the available logging data. Figure modified from Dick, Natland, Miller, et al. (1999).

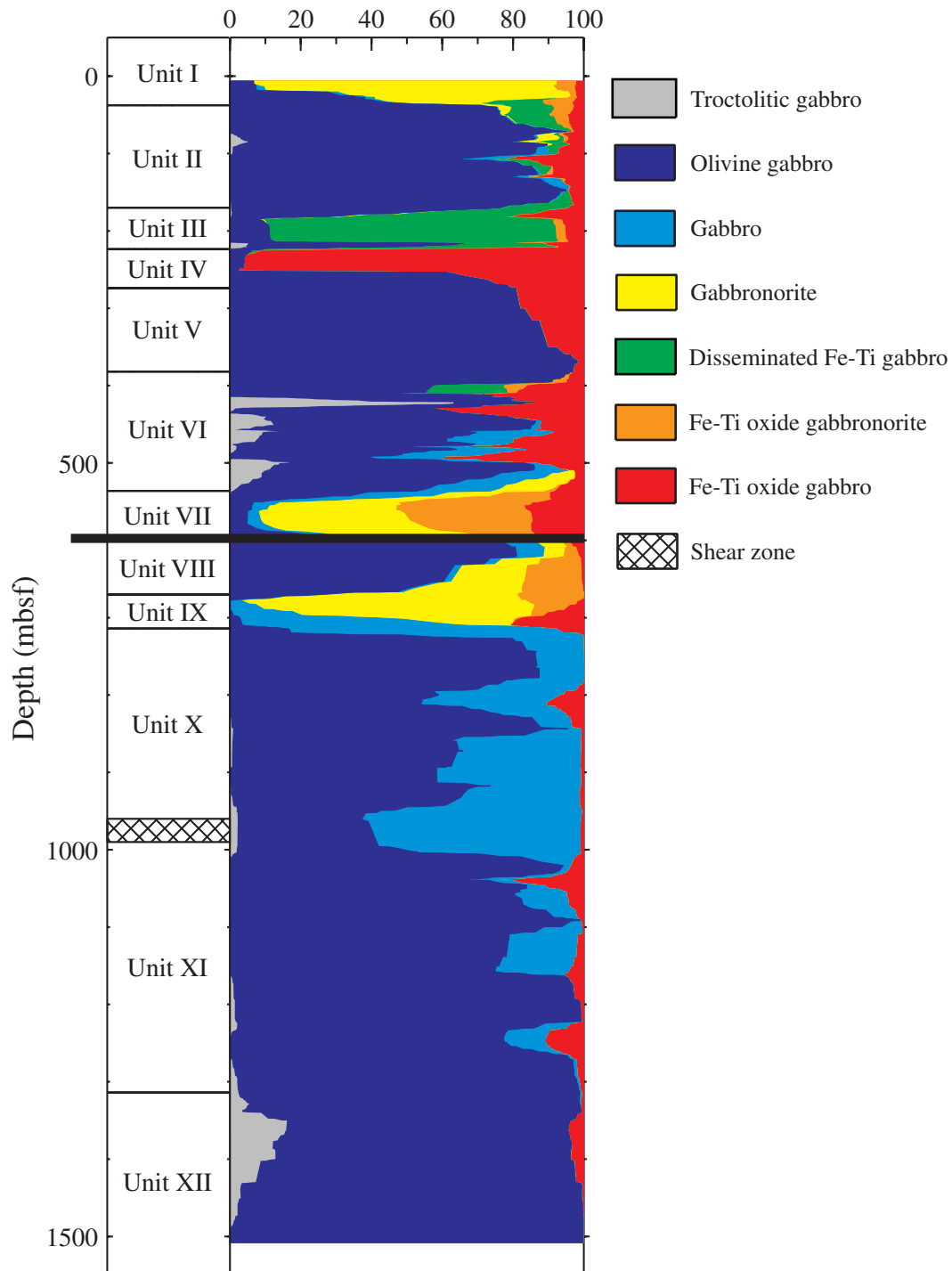


Figure F3. *P*-wave seismic velocity model from north-south trending ocean-bottom seismometer (OBS) data (from Muller et al., 1997). The position of Hole 735B is projected from a distance of 1 km west of the seismic line (CAM101) that was used for this model. The Moho is constrained by wide-angle reflections. OBS locations are shown on the seafloor.

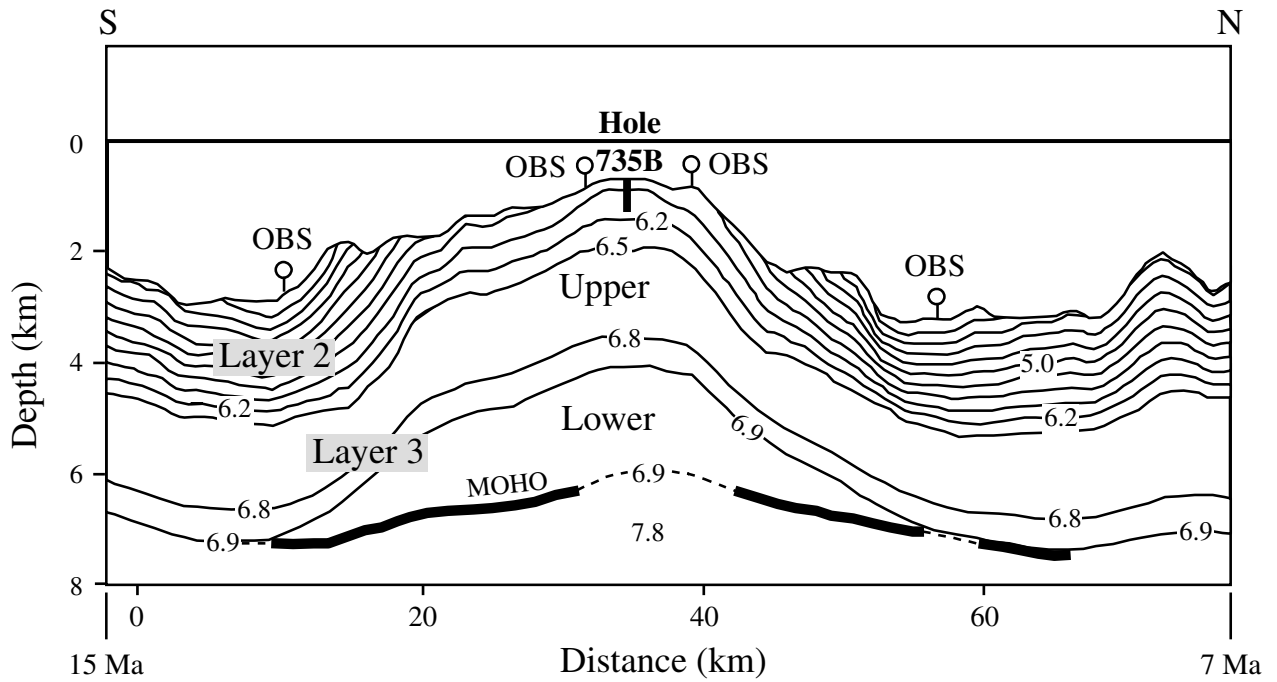


Figure F4. Caliper, compressional wave velocity, bulk density, and porosity logs as a function of depth. Physical properties measurements are also shown for a direct comparison with each log. Discrete velocity measurements were made at atmospheric pressure.

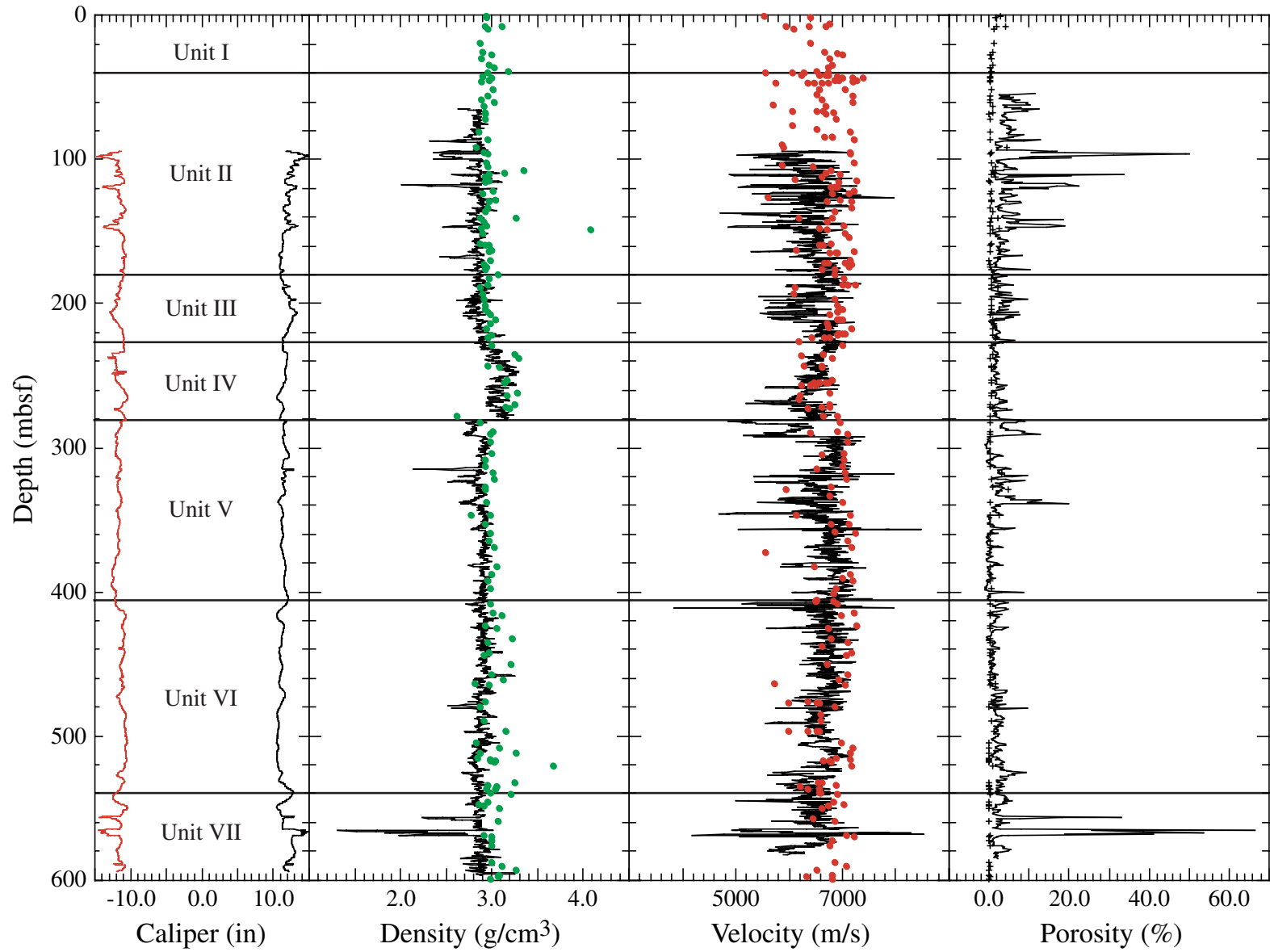


Figure F5. A. Discrete laboratory compressional wave velocity (V_p) measurements are shown as a function of depth. Atmospheric pressure measurements (black) and in situ measurements (red) are shown. B. Comparison between in situ V_p measurements and log measurements for the upper 600 m. Blue lines represent a linear fit to the log data for the large intervals shown. Green lines represent velocity trends for smaller intervals based on log data (V_p = compressional wave velocity and d = depth). C. Comparison between discrete in situ laboratory shear wave velocity (V_s) measurements (red) and log data is shown. Average values for the laboratory V_s data were used. Velocity gradients based on log data are also shown for three intervals (V_s = shear wave velocity and d = depth). Equations defining the V_p and V_s gradients for the entire section are given in the text but are not shown here for clarity of presentation.

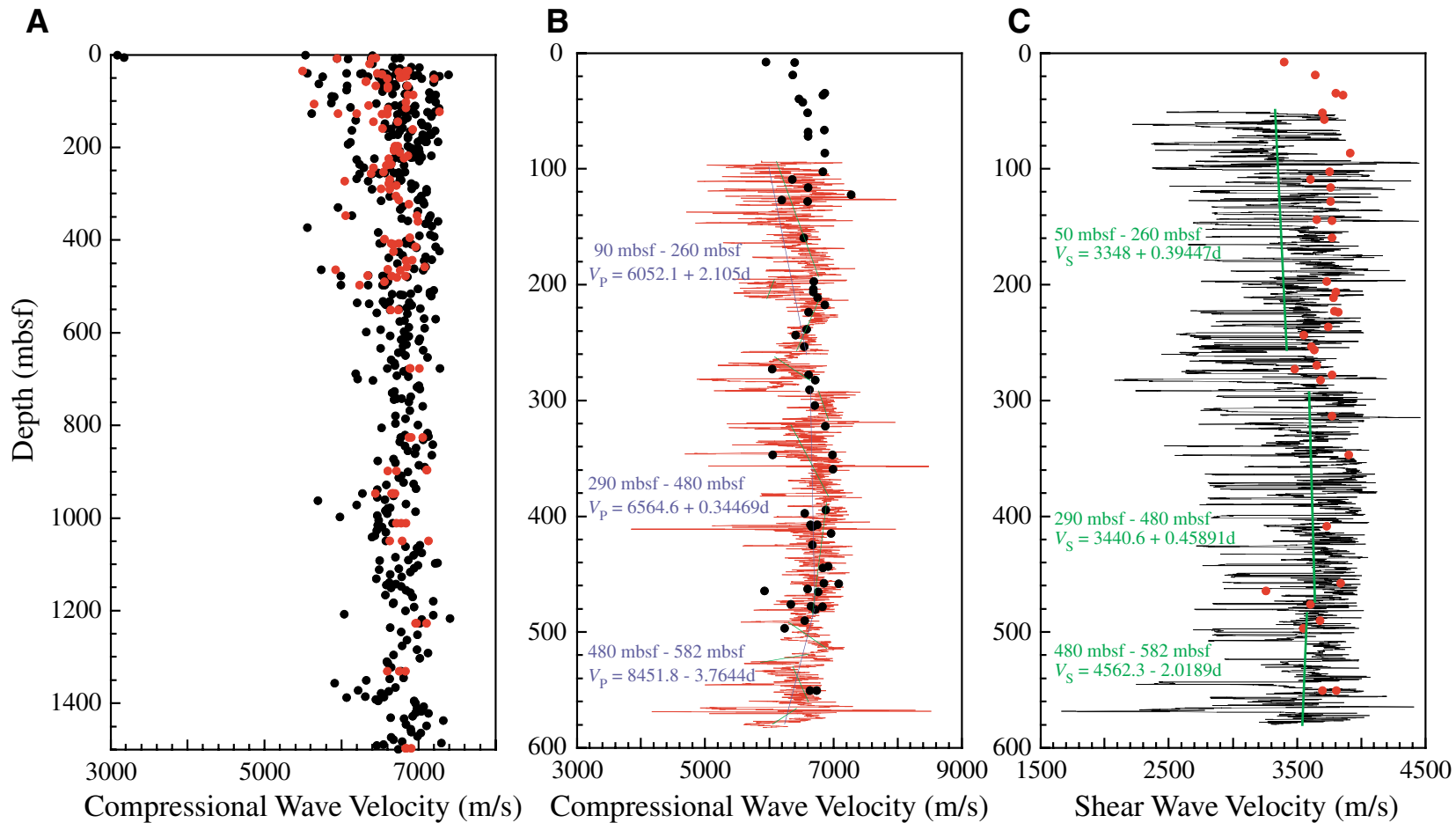


Figure F6. Effect of crack porosity on both (A) compressional wave and (B) shear wave velocities. The velocities of gabbroic samples were measured at 20 MPa because porosity measurements were not available at high pressures.

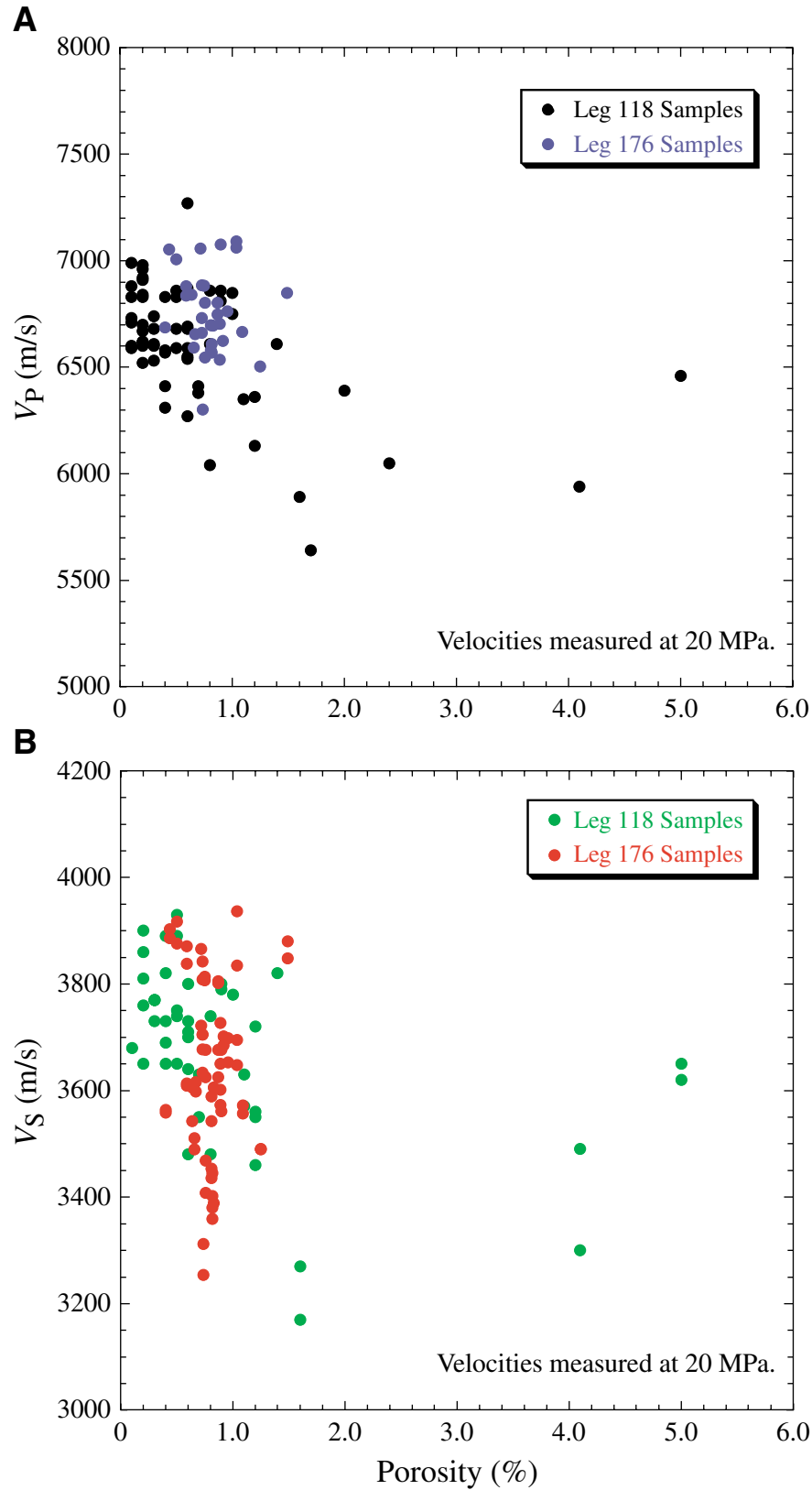


Figure F7. Velocity and density relationship for samples of Hole 735B. (A) Compressional wave and (B) shear wave relationships are shown for values measured at 200 MPa confining pressure. VRH values are also plotted to define the field where isotropic rocks composed of these mineral constituents would fall.

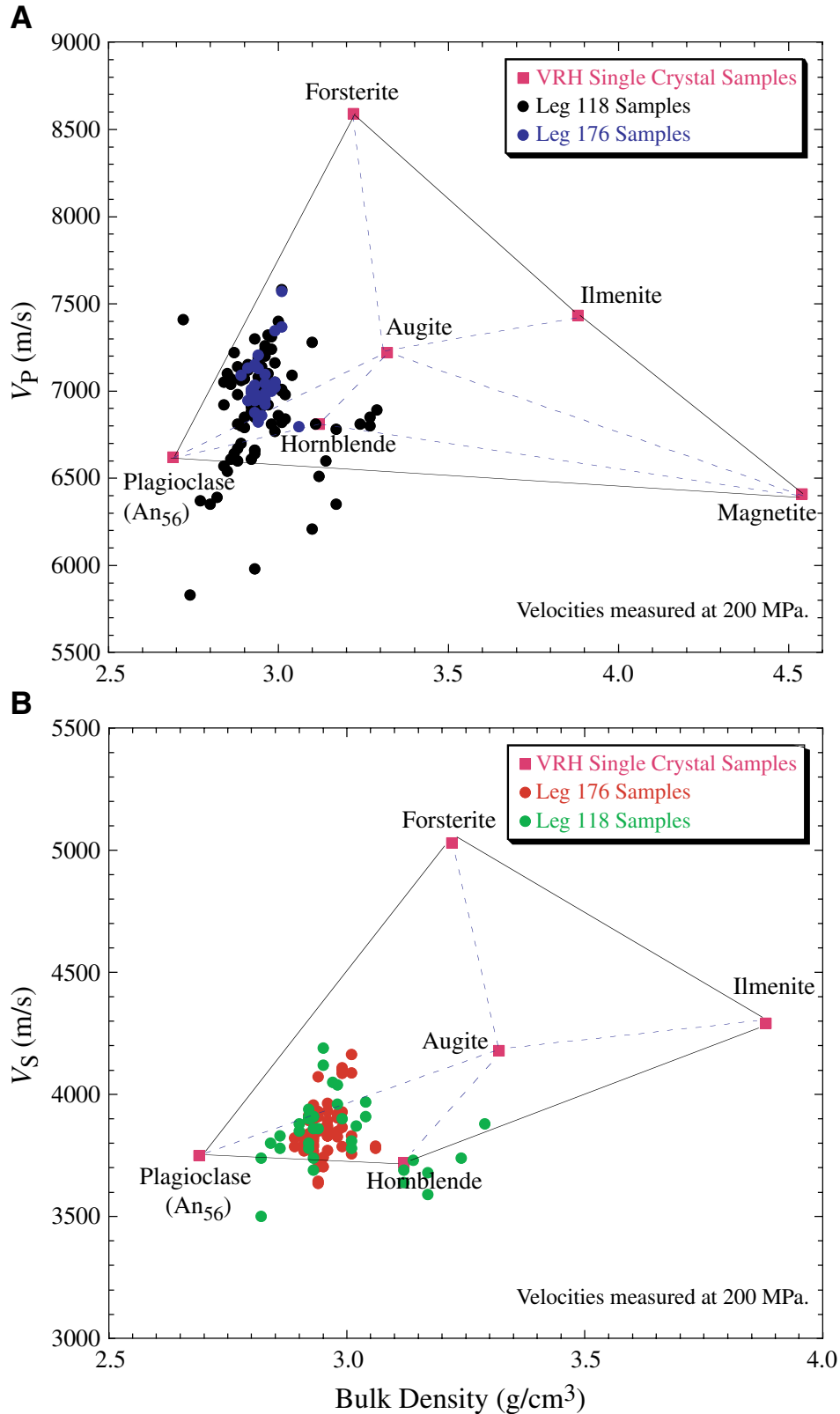
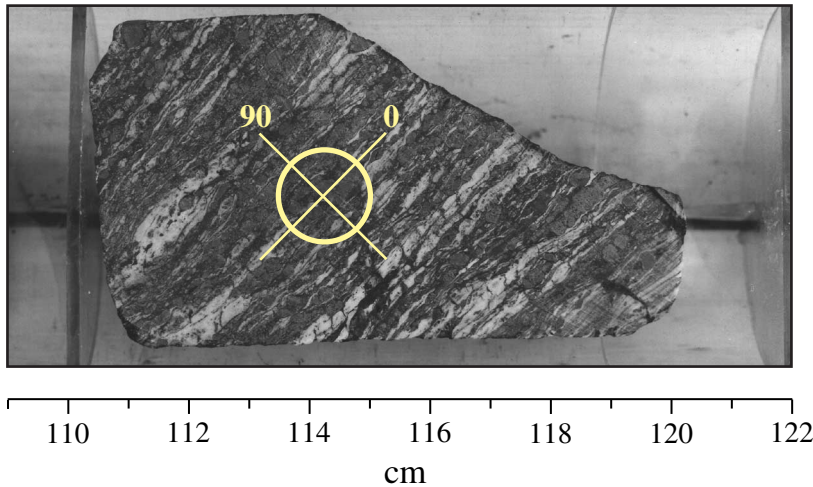
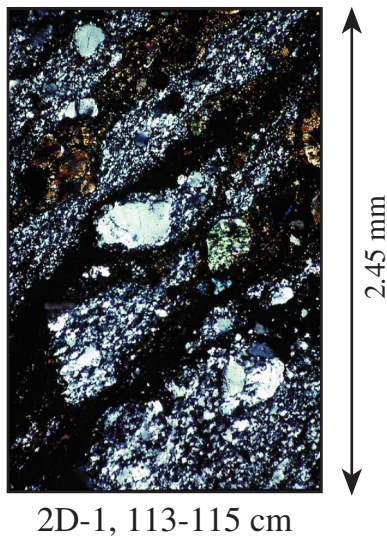


Figure F8. Most of the deformed gabbros recovered from ODP Hole 735B exhibit a well developed foliation dipping at 25°–35° and showing varying degrees of velocity anisotropy in laboratory experiments. **A.** Core photograph of Sample 118-735B-2D-1, 110–121 cm, shows a good example of a typical porphyroclastic foliated metagabbro with the yellow circle marking the location of the minicore used for laboratory velocity measurements as a function of confining pressure. **B.** Photomicrograph of the end piece of the same minicore shows the main mineral constituents (plagioclase-clinopyroxene-hornblende) as well as the well developed foliation. **C.** At a confining pressure of 200 MPa, this particular sample exhibits various degrees of shear wave splitting with the fast and slow directions being parallel and perpendicular to the foliation, respectively. The changes in delay time were obtained by rotating the transducers by 0°, 45°, 60°, and 90° (from Iturrino et al., 1991).

A



B



C

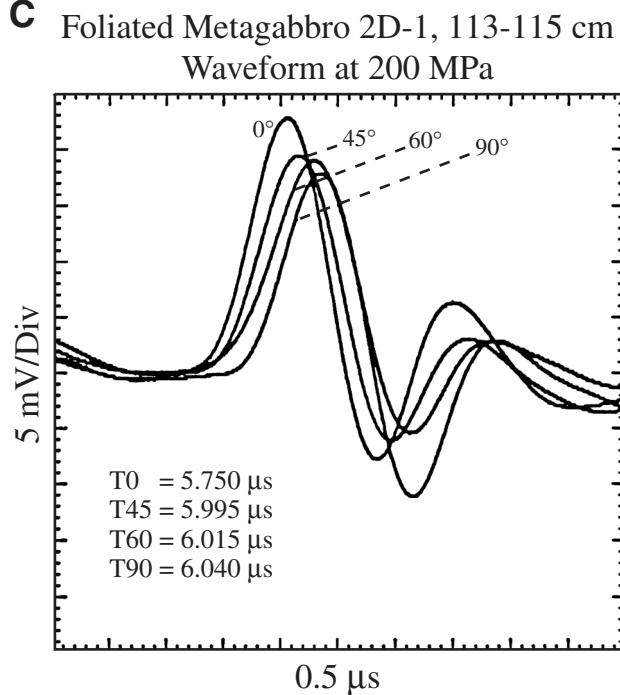


Figure F9. Diagram showing variations in Q_p , Q_{s1} , and Q_{s2} vs. depth in Hole 735B below 600 m. Only values corresponding to 200-MPa pressure intervals are plotted.

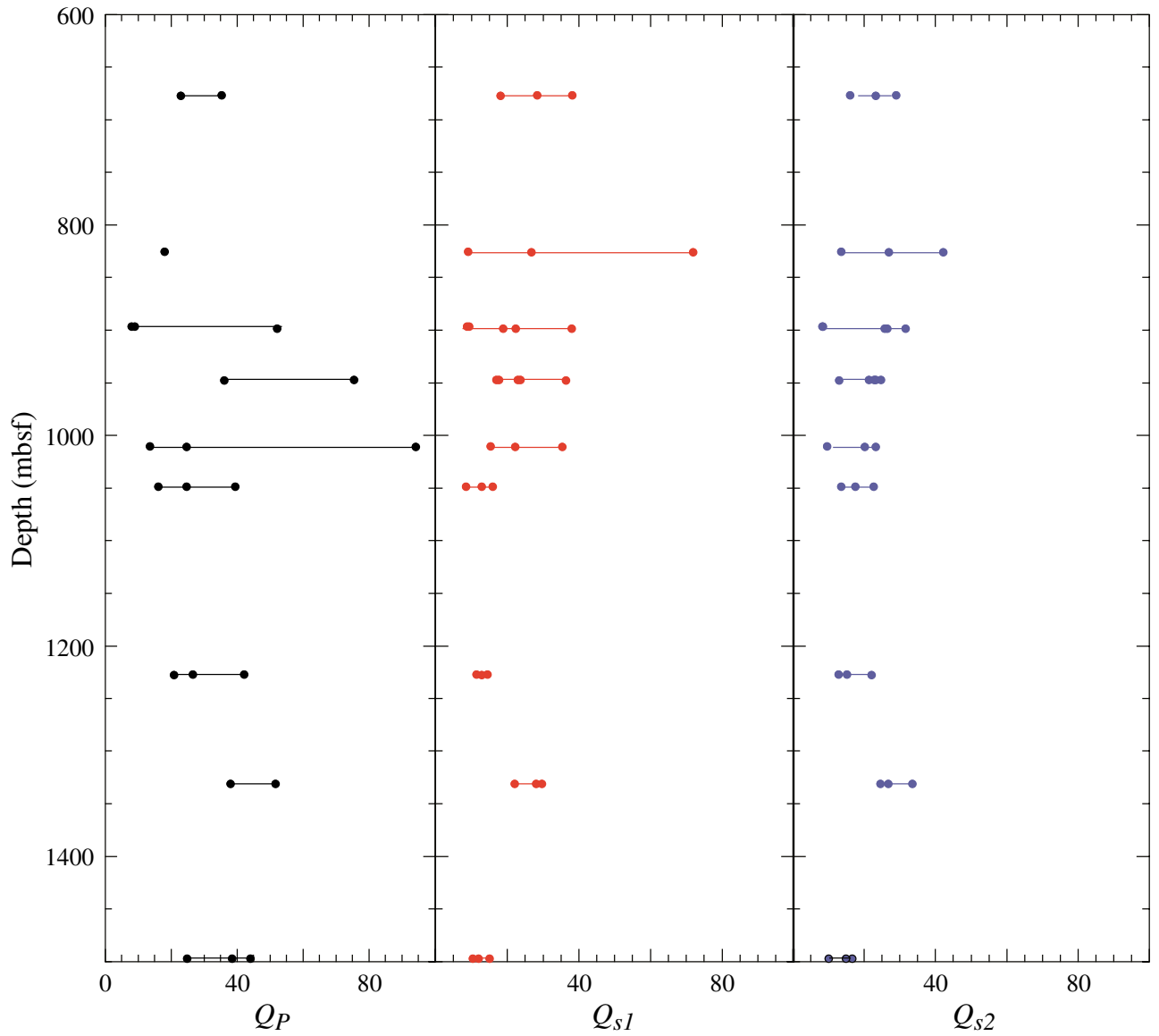


Figure F10. Downhole logs showing the FMS pad 1 azimuth as well as the fast angle azimuth and the average anisotropy determined from DSI analyses. The fast azimuth curve was smoothed using 20 point (blue) and 25-m sliding windows (black). The dashed vertical line (red) represents the average value of 89° for the entire logged section. The solid vertical lines (red) represent the maximum and minimum standard deviation values of 138° and 40° calculated from the smoothed fast azimuth curve (blue).

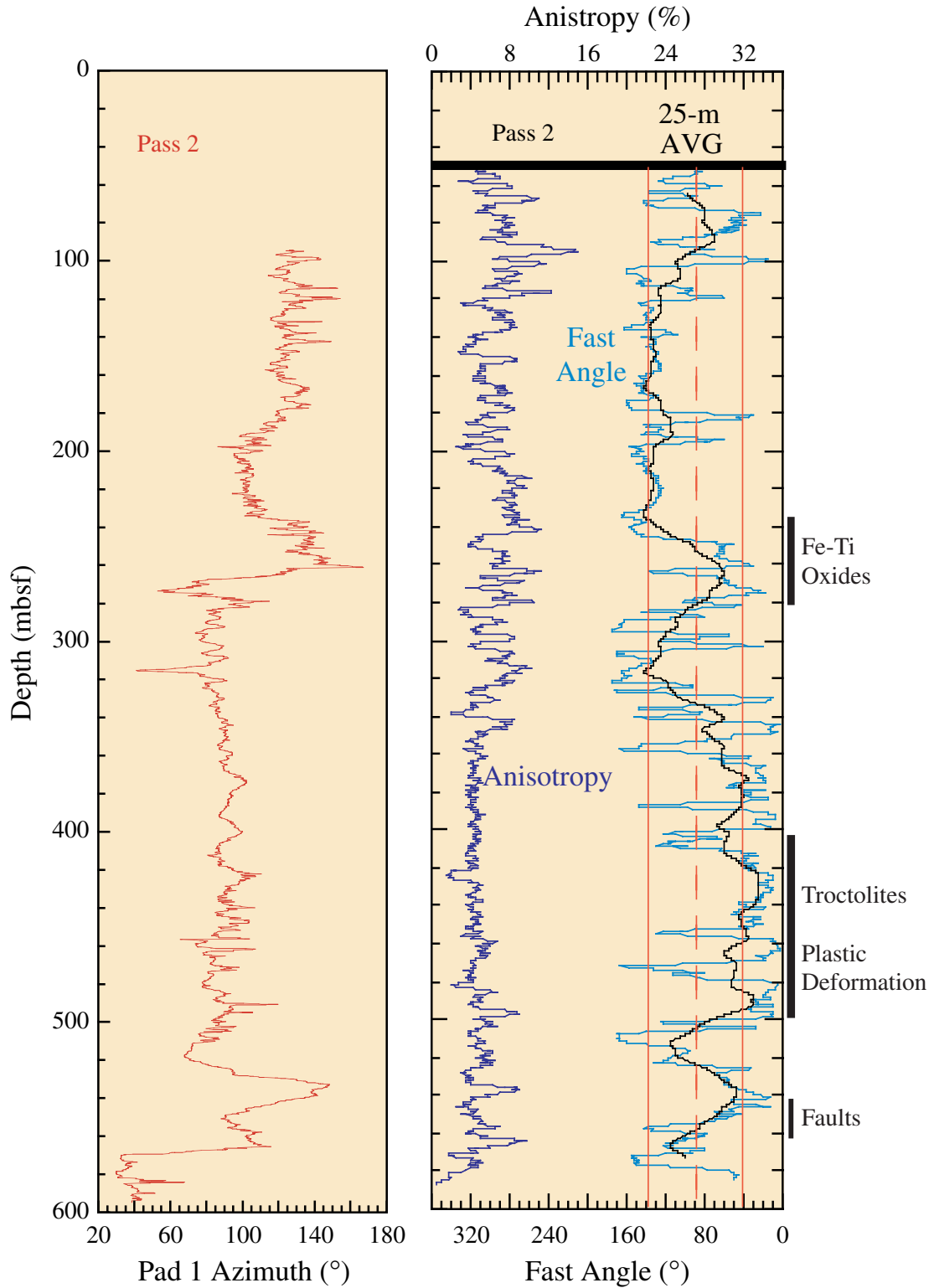


Figure F11. Bathymetric map showing the Atlantis II Fracture Zone and surrounding area. The map was created using the Lamont-Doherty Earth Observatory multibeam bathymetry database. Focal mechanisms and earthquake magnitudes (M_w) are plotted based on the Harvard Centroid Moment Tensor (CMT) solutions (Cornell University GIS Group, 1998). Strike and dip azimuth rose diagrams are based on FMS interpretations of intermediate (30° – 60°) and steep (60° – 90°) dips of foliations and fractures in Hole 735B. Black arrows in the insert represent the maximum and minimum orientations of the shear wave fast directions based on DSI analyses. The black line represents the average fast-angle orientation of the entire logged interval. The red P-axis line shows the approximate orientation of the compressional axis of the three strike-slip events along the Atlantis II Fracture Zone. The location of Hole 735B is marked is also shown (red dot).

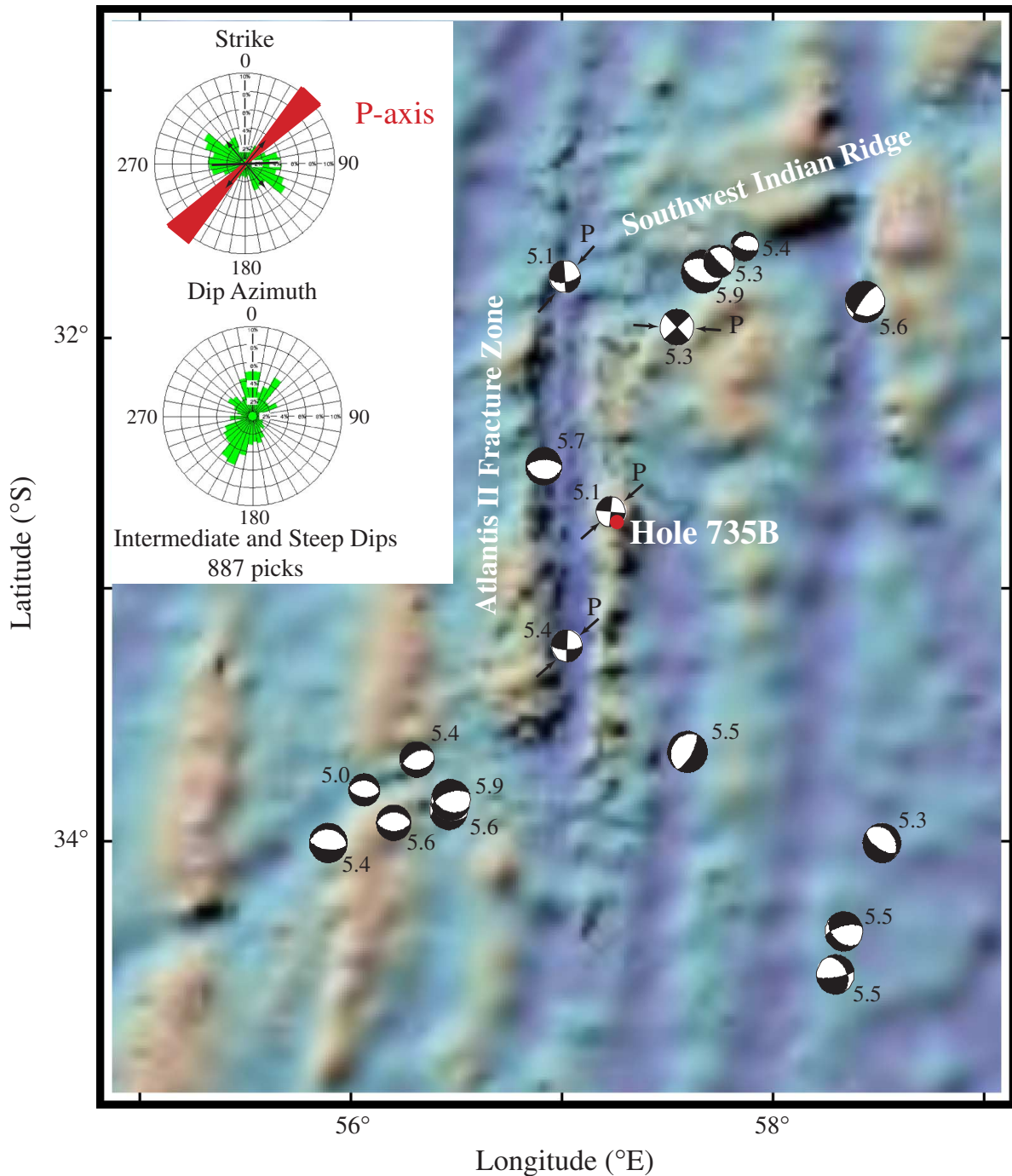


Figure F12. Compressional wave and shear wave synthetic seismograms from logging data collected during Leg 176. The plots show a depth-time relationship, transit time and density curves from the logs, depth and time scales, prominent boundaries, a reflection coefficient series, normal and reverse polarity synthetic traces, and a standard trace consisting of a 30-Hz Ricker wavelet. Yellow horizontal lines show the correlation between reflections and the downhole logs. Red horizontal lines represent the correlation of reflections between the synthetic seismogram using a 30-Hz Ricker wavelet and the results from using lower frequency 10-Hz Ricker and Ormsby (low cut = 2 Hz, low pass = 5 Hz, high pass = 15 Hz, and high cut = 20 Hz) wavelets. (Figure shown on next page.)

Figure F12 (continued). (Caption shown on previous page.)

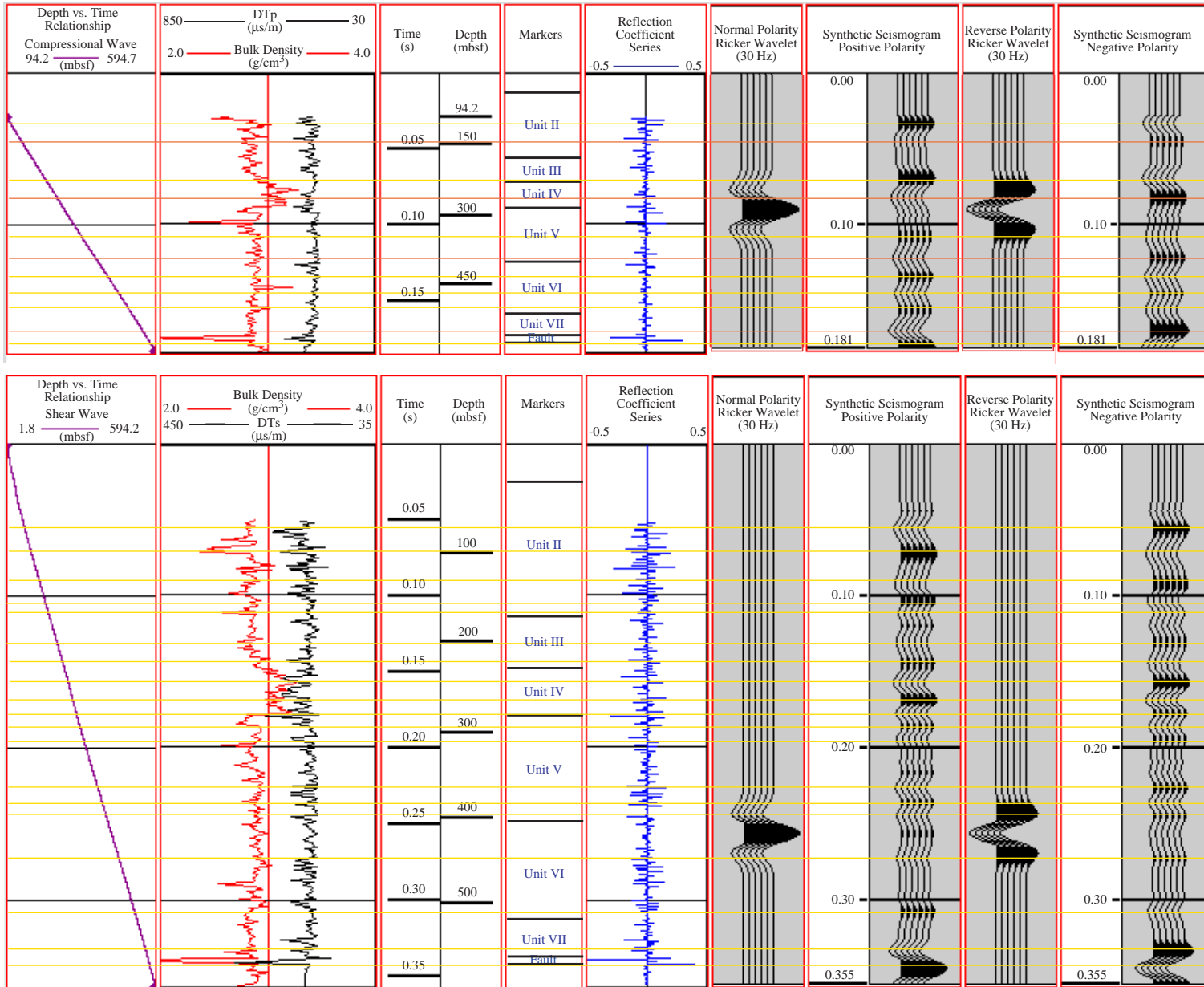


Figure F13. Correlation between the compressional wave synthetic seismograms and the geochemical, density, velocity, porosity, and resistivity logs obtained in Hole 735B during Legs 118 and 176. LLD = deep laterolog, LLS = shallow laterolog. [\(Figure shown on next page.\)](#)

Figure F13 (continued). (Caption shown on previous page.)

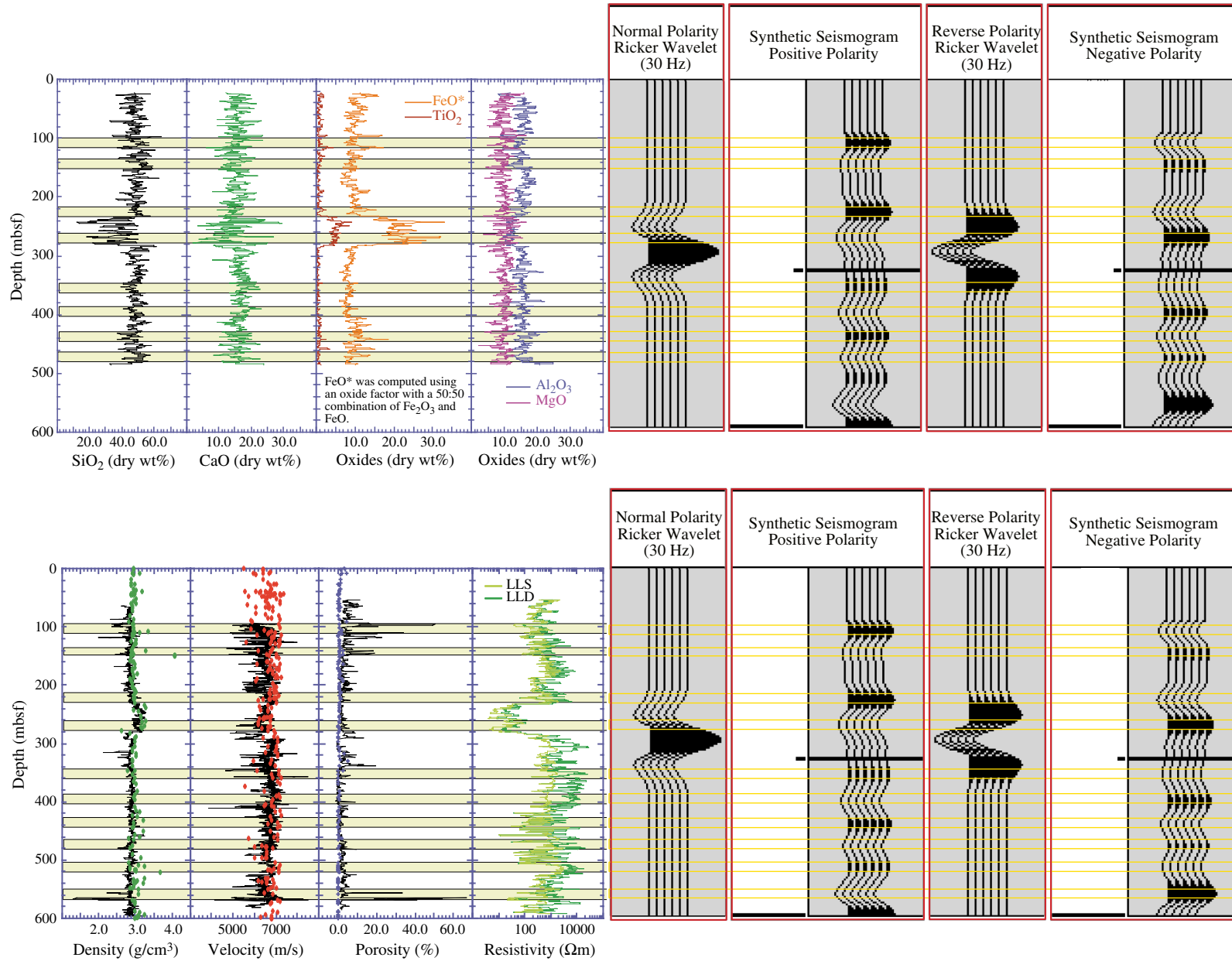


Figure F14. Correlation between Leg 176 synthetic seismograms produced with logging data collected during Leg 176 and VSP results from the experiment carried out during Leg 118 (Robinson, Von Herzen, et al., 1989; Swift et al., 1991). A synthetic seismogram produced with core data for the upper 500 m is also included in the comparison (Iturrino and Christensen, 1991). D = depth (mbsf), V = velocity model (km/s), ρ = density model (g/cm³), RC = reflection coefficient series, SYN = synthetic seismogram consisting of seven identical traces, ST = standard trace representing a +0.1/-0.1 reflection coefficient interface that is provided for comparing amplitudes.

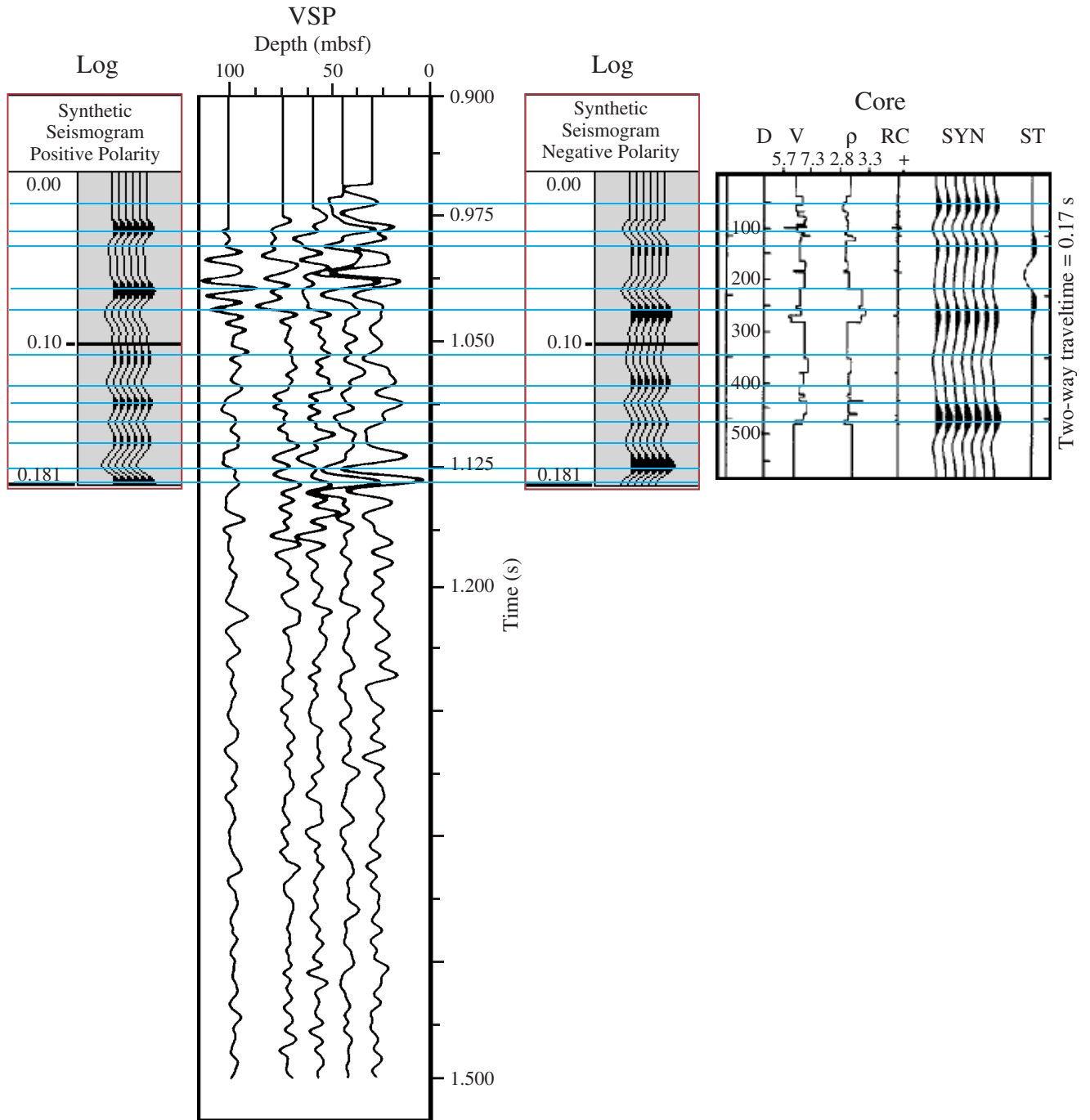


Figure AF1. Schematic diagram showing the orientation, with respect to the Ocean Drilling Program (ODP) core system, of the samples used for laboratory measurements.

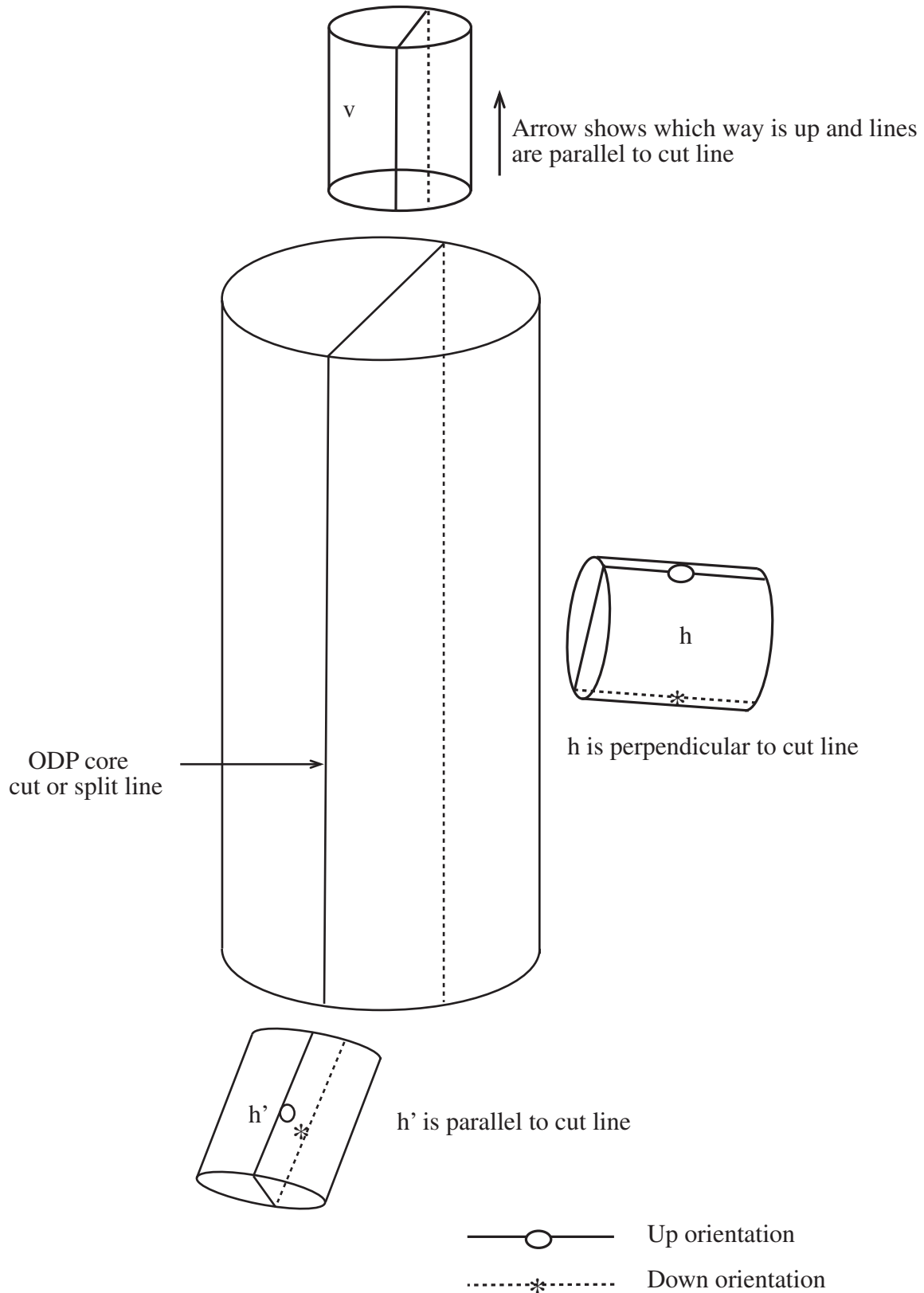


Figure AF2. A. Diagram showing data acquired during Q experiments. The recorded waveform with the gray line being the entire waveform and the black line being the windowed version that was used for the analysis. B. A similar graph displaying the reference waveform (and its windowed version) from a 2-in-long aluminum sample. C. The amplitude spectra of the waveforms for the aluminum (dashed) and sample (solid) are plotted. D. A plot of the portion of the amplitude ratio (Aratio) vs. frequency that was used for computing Q, and a line indicating the inferred slope.

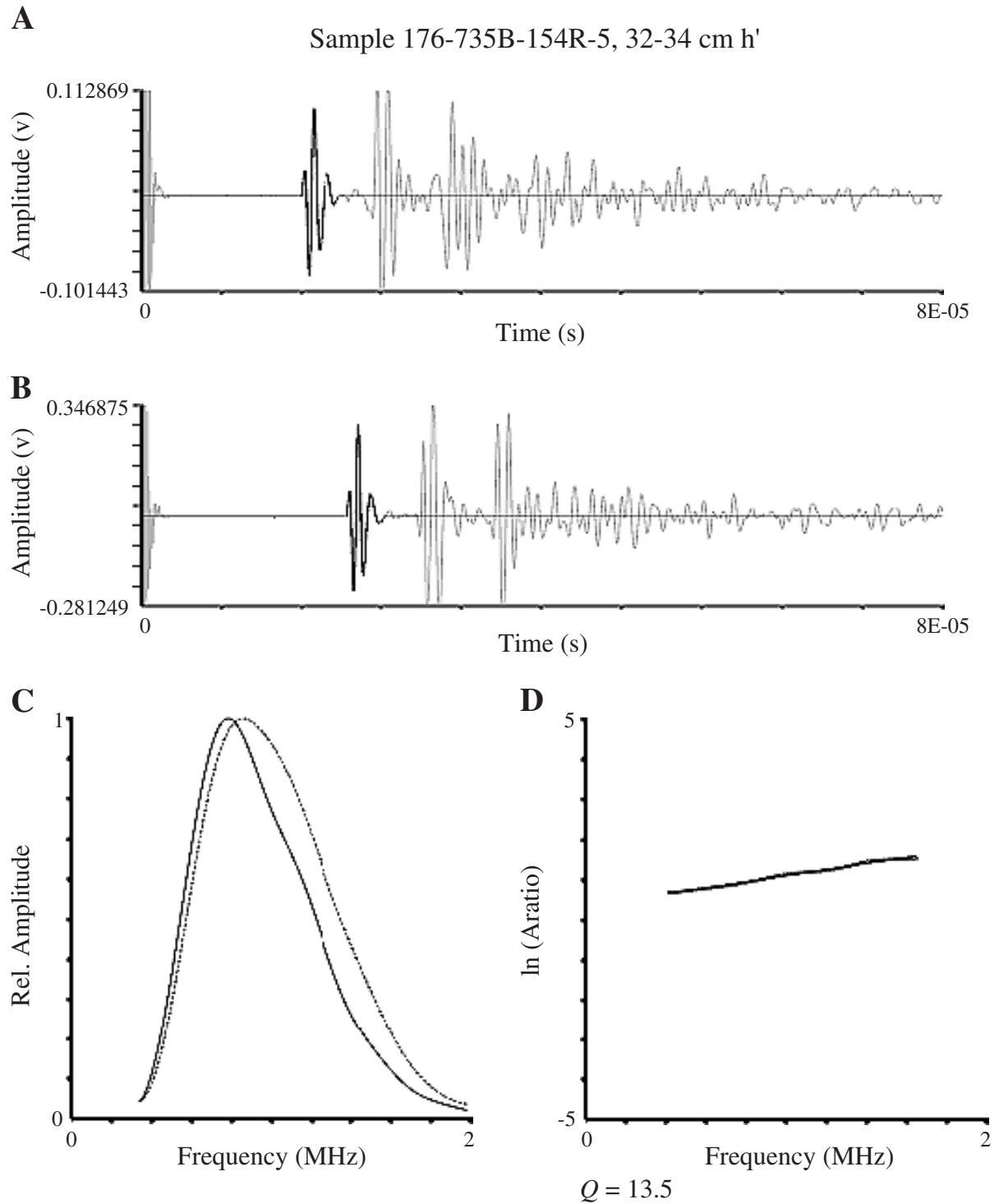


Figure AF3. Processed cross-dipole shear wave data collected during Leg 176 for the upper 600 m of Hole 735B. The plot shows the caliper and tool azimuth measurements, quality curves ($S1_{ISO}$ and $S2_{ISO}$) that were used for the anisotropy estimate ($S1_{ISO}/S2_{ISO}$) and anisotropy azimuth ($S1S2$), fast and slow direction transit time curves (0.152-m sampling interval), semblance, fast (red) and slow (black) shear waveforms, anisotropy and average anisotropy (2.5-m sliding window) curves, and fast-wave orientation and tool azimuths. DT = delta time, DTS = shear slowness.

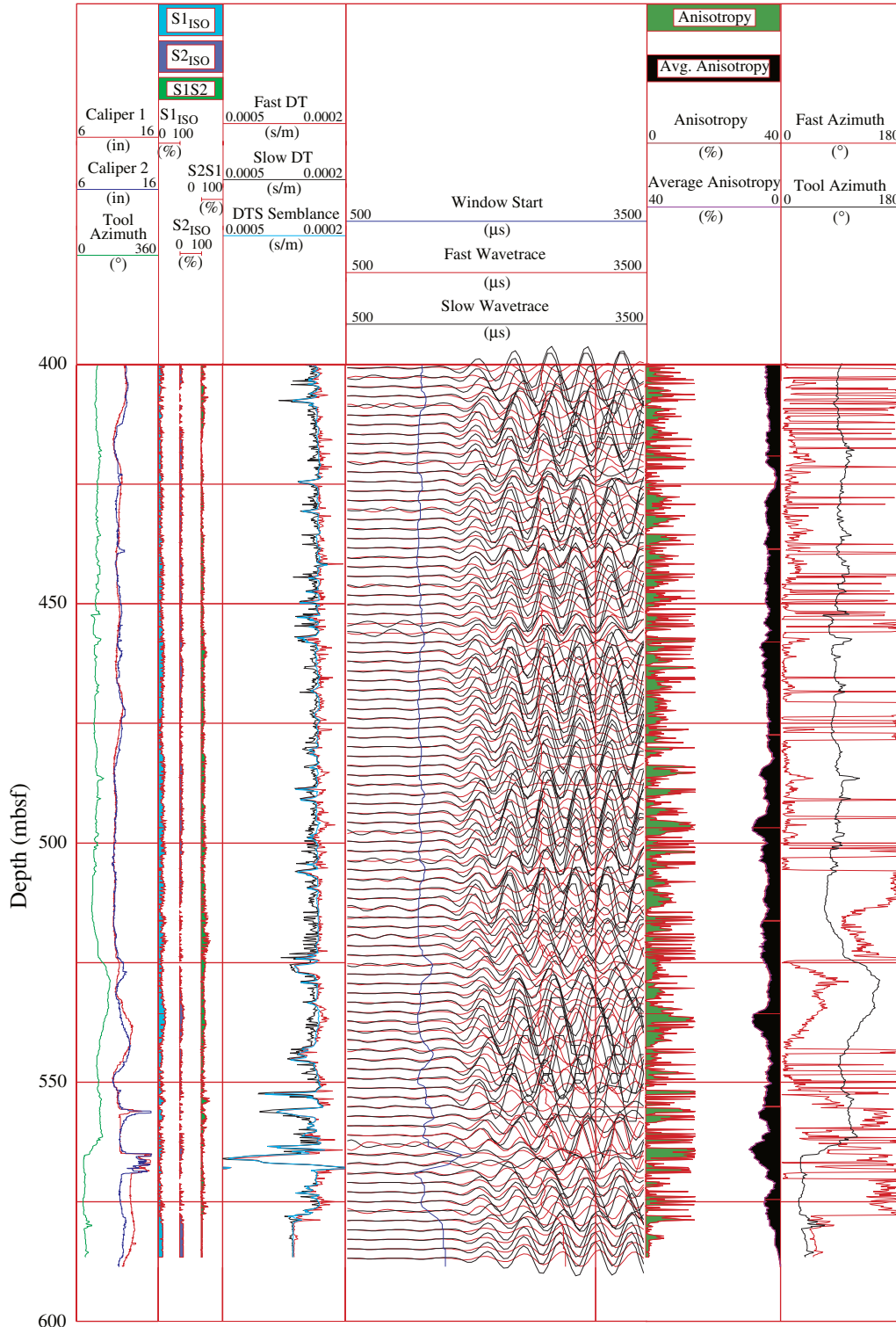


Table T1. Index properties, compressional wave and shear wave velocities, attenuation, mineralogy, and deformation information. (See [table notes](#). Continued on next 27 pages.)

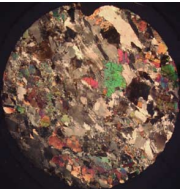
Sample (Leg-Hole-Core-Section-Interval-Orientation)	Depth (mbsf)	Porosity (%)	Bulk density (g/cm ³)	Grain density (g/cm ³)	Pc (MPa)	Pp (MPa)	Ep (MPa)	Vp (m/s)	Vs1 (m/s)	Vs2 (m/s)	Vp Anisotropy	Vs Anisotropy	Vsmax Anisotropy	Qp	Qs1	Qs2			
176-735B-96R-2 (49-51) h'	550.29	0.87	2.95	2.96	10.0	2.1	7.9	6649	3799	3805	-0.7	0.0	0.7						
					20.3	2.0	18.3	6748	3805	3802	1.9	0.0	0.7						
					40.2	2.1	38.1	6669	3791	3796	0.0	0.0	0.5						
					60.4	2.0	58.3	6712	3818	3809	0.6	-0.1	0.6	20.3	14.8	15.2			
					80.2	2.1	78.0	6695	3802	3774	-0.2	-0.2	0.3						
					100.3	2.1	98.2	6744	3830	3789	0.3	-0.3	0.3	30.7	21.6	19.1			
					150.1	2.1	148.0	6811	3841	3825	0.7	-0.1	0.5	38.5	32.5	29.8			
					200.3	2.1	198.2	6859	3857	3860	0.9	0.0	0.5	41.4	32.7	29.9			
					100.4	2.1	98.3	6757	3832	3808	0.2	-0.2	0.5						
					60.2	2.1	58.1	6731	3835	3816	0.7	-0.1	0.5	20.9	16.2	15.5			
					10.5	2.0	8.5	6694	3802	3802	0.7	0.0	0.6						
					176-735B-96R-2 (54-58) v	550.34	0.92	3.06	3.08	10.0	2.1	7.8	6695	3674	3699		-0.2		
20.1	2.1	18.0	6624	3685						3702		-0.1							
39.9	2.2	37.7	6669	3698						3714		-0.1							
60.1	2.1	58.0	6675	3711						3718		0.0		17.9	13.0	14.2			
80.2	2.1	78.1	6706	3729						3729		0.0							
100.2	2.1	98.1	6724	3740						3746		0.0		23.4	16.6	19.6			
150.2	2.1	148.1	6762	3781						3754		0.2		36.5	18.7	21.9			
200.0	2.1	198.0	6796	3788						3779		0.1		44.3	19.2	25.2			
100.1	2.1	98.0	6745	3750						3733		0.1							
60.2	2.1	58.2	6683	3729						3738		-0.1		18.8	13.3	15.4			
10.0	2.1	7.9	6650	3694						3710		-0.1							
176-735B-116R-4 (127-129) h 	677.04	0.59	2.96	2.97						10.0	2.1	7.9	6911	3867	3833	1.0	0.2	0.5	
					20.3	1.9	18.3	6880	3871	3838	1.8	0.2	0.5						
					40.1	2.1	38.0	6881	3880	3825	1.9	0.4	0.6						
					60.2	2.1	58.2	6865	3873	3823	1.7	0.3	0.6	20.2	16.7	11.6			
					80.3	2.0	78.2	6873	3875	3817	1.6	0.4	0.6						
					100.6	2.0	98.6	6893	3886	3810	1.8	0.5	0.8	24.9	24.2	13.2			
					150.3	2.0	148.3	6946	3873	3831	1.8	0.3	0.8	34.6	27.4	15.0			
					200.1	2.1	198.1	6974	3862	3830	1.7	0.2	-0.9	35.2	28.4	16.1			
					100.3	2.1	98.2	6938	3862	3798	1.4	0.4	1.0						
					60.2	2.1	58.1	6866	3852	3795	2.0	0.4	0.8	19.0	16.6	9.9			
					10.2	2.1	8.2	6834	3846	3799	2.4	0.3	0.8						
					176-735B-116R-4 (129-133) v	677.06	0.50	2.96	2.97	10.1	2.2	7.9	6983	3868	3918		0.3		
20.0	2.2	17.8	7007	3876						3917		0.3							
40.1	2.2	37.9	7013	3892						3921		0.2							
60.2	2.2	58.1	6985	3884						3912		0.2		46.1	21.7	14.4			
80.5	2.1	78.4	6985	3928						3915		-0.1							
100.4	2.2	98.2	7016	3906						3934		0.2		66.9	30.3	18.1			
150.3	2.2	148.1	7074	3950						3949		0.0		260.0	37.9	22.9			
200.2	2.1	198.1	7095	3932						3964		0.2		inf	38.2	28.9			
100.4	2.2	98.2	7038	3906						3955		0.3							
60.3	2.1	58.2	7007	3915						3925		0.1		46.4	24.6	14.6			
10.0	2.2	7.9	6999	3906						3925		0.1							
176-735B-116R-5 (7-9) h'	677.27	0.75	2.92	2.93						10.1	2.1	8.0	6905	3803	3783		0.1		
					20.0	2.2	17.8	6882	3814	3807		0.0							
					40.2	2.1	38.1	6913	3846	3822		0.2							
					60.2	2.1	58.1	6876	3837	3835		0.0		14.0	12.5	13.4			
					80.5	2.1	78.5	6829	3851	3850		0.0							
					100.2	2.2	98.1	6850	3870	3868		0.0		21.7	18.9	18.9			
					150.2	2.1	148.0	6939	3886	3895		-0.1		27.9	19.7	24.1			
					200.2	2.1	198.1	6991	3915	3906		0.1		22.9	18.1	23.2			
					100.5	2.1	98.4	6846	3874	3871		0.0							
					60.3	2.1	58.1	6853	3849	3841		0.1		13.9	12.9	12.7			
					10.2	2.1	8.1	6811	3826	3826		0.0							

Table T1 (continued).

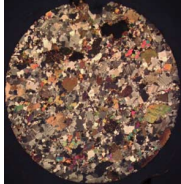
Sample (Leg-Hole-Core-Section-Interval-Orientation)	Depth (mbsf)	Porosity (%)	Bulk density (g/cm ³)	Grain density (g/cm ³)	Pc (MPa)	Pp (MPa)	Ep (MPa)	Vp (m/s)	Vs1 (m/s)	Vs2 (m/s)	Vp Anisotropy	Vs Anisotropy	Vsmax Anisotropy	Qp	Qs1	Qs2					
176-735B-133R-2 (126-128) h'	825.50	0.73	2.93	2.95	10.1	2.2	7.9	6952	3843	3797	0.9	0.3	-0.1								
					20.1	2.2	17.9	6885	3842	3808	0.5	0.2	0.0								
					40.3	2.2	38.1	6913	3871	3815	0.3	0.4	0.2								
					60.2	2.2	58.0	6949	3875	3858	0.7	0.1	0.3	13.4	8.7	9.4					
					80.3	2.2	78.1	6988	3879	3855	1.2	0.2	0.3								
					100.4	2.2	98.1	7024	3895	3882	2.1	0.1	0.4	17.3	8.3	9.5					
					150.3	2.2	148.1	7077	3919	3903	2.1	0.1	0.3	19.8	9.9	12.6					
					200.2	2.3	197.9	7150	3926	3899	2.8	0.2	0.4	17.9	9.1	13.6					
					100.4	2.2	98.1	7002	3956	3897	1.1	0.4	0.4								
					60.3	2.2	58.0	7012	3933	3884	1.5	0.3	0.4	14.1	8.5	9.2					
10.2	2.3	7.9	6885	3884	3864	0.4	0.1	0.1													
176-735B-133R-3 (0-7) v 	825.63	1.49	2.96	2.99	9.8	2.2	7.5	6893	3895	3867			-0.2								
					19.8	2.2	17.6	6849	3880	3848			-0.2								
					40.1	2.2	37.9	6891	3863	3856			0.0								
					60.1	2.2	58.0	6898	3850	3844			0.0	30.7	17.5	17.1					
					80.3	2.1	78.2	6902	3846	3852			0.0								
					100.1	2.2	97.9	6878	3850	3847			0.0	48.9	22.0	21.7					
					150.1	2.1	148.0	6931	3860	3865			0.0	107.0	24.5	27.2					
					200.1	2.1	198.0	6955	3872	3894			0.1	162.0	26.7	26.9					
					100.4	2.1	98.3	6922	3847	3852			0.0								
					60.3	2.1	58.1	6907	3845	3849			0.0	34.4	17.8	16.8					
10.0	2.2	7.8	6860	3883	3853			-0.2													
176-735B-133R-3 (7-9) h	825.70	0.44	2.94	2.95	10.1	2.1	7.9	6973	3872	3882			0.1								
					20.1	2.1	18.0	7052	3903	3886			-0.1								
					40.3	2.1	38.2	7049	3889	3890			0.0								
					60.3	2.1	58.2	7048	3891	3899			0.1	130.0	53.0	30.5					
					80.1	2.2	77.9	7055	3895	3897			0.0								
					100.2	2.1	98.1	7071	3903	3905			0.0	540.0	109.0	39.1					
					150.2	2.1	148.1	7109	3896	3912			0.1	inf	77.5	50.2					
					200.0	2.1	197.9	7130	3909	3930			0.1	inf	71.8	42.2					
					100.3	2.1	98.2	7079	3895	3903			0.1								
					60.2	2.1	58.1	7053	3893	3900			0.0	115.0	65.2	25.3					
10.4	2.0	8.4	7039	3884	3894			0.1													
176-735B-142R-3 (86-88) h'	896.47	1.04	3.01	3.03	10.3	2.1	8.3	7122	3618	3930	8.9	2.1	2.3								
					20.0	2.2	17.9	7090	3695	3936	4.2	1.6	2.9								
					40.1	2.2	37.9	7109	3730	3951	4.2	1.4	3.5								
					60.2	2.1	58.1	7115	3753	3999	4.0	1.6	2.8	6.5	5.3	4.9					
					80.1	2.2	78.0	7125	3748	3981	3.8	1.5	2.5								
					100.2	2.2	98.0	7140	3766	3985	3.8	1.4	2.2	6.4	7.0	6.0					
					150.4	2.1	148.3	7269	3799	4047	4.6	1.6	2.1	8.2	8.3	7.9					
					200.3	2.1	198.2	7367	3831	4088	5.9	1.6	2.6	9.0	8.8	8.4					
					100.6	2.0	98.6	7165	3780	3997	3.4	1.4	1.9								
					60.4	2.1	58.3	7149	3751	3988	3.7	1.5	2.0	7.0	5.6	5.3					
10.4	2.1	8.3	7047	3687	3945	9.0	1.7	2.9													
176-735B-142R-3 (86-88) h' 45°	896.47	1.04	3.01	3.03	10.2	2.1	8.1	6957	3699	3606	6.4	0.6									
					20.2	2.1	18.1	7061	3835	3648	3.8	1.2									
					40.0	2.2	37.8	7114	3981	3734	4.3	1.6									
					60.1	2.1	58.0	7198	3964	3737	5.2	1.5		6.8	8.0	7.3					
					80.3	2.1	78.2	7370	3981	3705	7.3	1.8									
					100.2	2.1	98.1	7370	3964	3685	7.0	1.8		8.0	9.8	7.7					
					150.0	2.1	147.9	7468	4020	3729	7.4	1.9		8.1	10.7	8.5					
					199.9	2.1	197.8	7572	4164	3758	8.8	2.6		8.0	9.4	8.2					
					100.2	2.1	98.1	7168	3981	3691	3.4	1.9									
					60.0	2.2	57.9	7223	3987	3745	4.7	1.6		7.1	7.9	7.0					
10.2	2.1	8.1	7168	3866	3648	10.8	1.5														

Table T1 (continued).

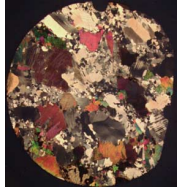
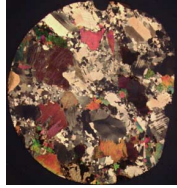
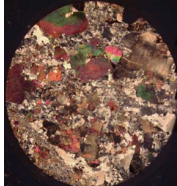
Sample (Leg-Hole-Core-Section-Interval-Orientation)	Depth (mbsf)	Porosity (%)	Bulk density (g/cm ³)	Grain density (g/cm ³)	Pc (MPa)	Pp (MPa)	Ep (MPa)	Vp (m/s)	Vs1 (m/s)	Vs2 (m/s)	Vp Anisotropy	Vs Anisotropy	Vsmax Anisotropy	Qp	Qs1	Qs2				
176-735B-142R-5 (0-6) v	898.44	0.87	2.91	2.93	10.1	2.1	8.0	6525	3580	3530		0.4								
					20.3	2.1	18.2	6802	3676	3625					0.3					
					40.4	2.1	38.4	6820	3691	3647										
					60.3	2.1	58.1	6836	3714	3672								48.4	15.7	17.6
					80.4	2.1	78.3	6858	3741	3687										
					100.6	2.1	98.5	6876	3756	3708										
					150.5	2.1	148.4	6941	3792	3744								107.0	18.3	20.3
					200.3	2.1	198.2	6945	3819	3769								208.0	21.4	25.1
					100.5	2.1	98.3	6928	3787	3734								147.0	22.3	25.7
					60.3	2.1	58.2	6893	3776	3729								89.0	18.9	18.7
					10.3	2.1	8.2	6452	3635	3584										
176-735B-142R-5 (6-8) h 	898.50	0.76	2.93	2.94	10.1	2.1	8.0	6525	3580	3530		0.4								
					20.3	2.1	18.2	6802	3676	3625										
					40.4	2.1	38.4	6820	3691	3647										
					60.3	2.1	58.1	6836	3714	3672								62.4	20.9	17.9
					80.4	2.1	78.3	6858	3741	3687										
					100.6	2.1	98.5	6876	3756	3708										
					150.5	2.1	148.4	6941	3792	3744								133.0	30.8	20.4
					200.3	2.1	198.2	6945	3819	3769								inf	38.9	27.1
					100.5	2.1	98.3	6928	3787	3734								inf	37.9	31.6
					60.3	2.1	58.2	6893	3776	3729								65.0	23.7	18.5
					10.3	2.1	8.2	6452	3635	3584										
176-735B-142R-5 (6-8) h 45° Parallel to foliation 	898.50	0.76	2.93	2.94	10.0	2.2	7.8	6546	3440	3374		0.5								
					20.1	2.2	17.9	6546	3468	3408										
					39.9	2.3	37.6	6622	3496	3456										
					60.2	2.3	57.9	6736	3590	3548								28.5	18.6	12.2
					80.2	2.3	78.0	6781	3654	3603										
					100.2	2.3	98.0	6863	3686	3634										
					150.2	2.3	147.9	6891	3763	3700								36.4	20.8	18.1
					200.1	2.3	197.8	6947	3810	3755								52.8	21.9	23.0
					100.3	2.3	98.0	6863	3743	3689								52.2	18.8	26.4
					60.1	2.3	57.8	6854	3727	3678								39.0	21.5	15.3
					10.0	2.3	7.6	6099	3511	3442										
176-735B-147R-6 (32-39) v	947.26	0.74	2.95	2.96	10.3	2.1	8.2	6135	3253	3173	2.3	0.6	2.3							
					20.3	2.1	18.2	6302	3312	3254	-1.5	0.4	2.3							
					40.2	2.2	38.0	6492	3386	3340	0.7	0.3	2.0							
					60.4	2.1	58.3	6635	3494	3444	0.8	0.4	1.5	18.2	18.0	14.1				
					80.3	2.1	78.2	6730	3576	3524	1.1	0.4	1.1							
					100.7	2.0	98.7	6766	3601	3560	2.0	0.3	0.8	27.5	21.9	15.4				
					150.3	2.1	148.2	6875	3682	3647	0.9	0.2	1.0	51.9	24.1	21.1				
					200.3	2.1	198.3	6951	3742	3705	3.8	0.2	1.0	75.5	23.0	23.2				
					100.4	2.1	98.3	6868	3697	3657	1.4	0.3	1.1							
					60.3	2.1	58.1	6799	3672	3622	0.5	0.3	1.4	19.9	22.7	17.1				
					10.5	2.0	8.5	6043	3422	3311	5.4	0.8	1.1							
176-735B-147R-6 (39-41) h 	947.33	0.81	2.93	2.94	10.1	2.1	8.0	6538	3396	3386		0.1								
					20.2	2.1	18.1	6580	3453	3436										
					39.9	2.2	37.7	6717	3576	3541										
					60.1	2.2	58.0	6804	3675	3641								39.1	18.3	15.8
					80.5	2.0	78.5	6875	3721	3694										
					100.3	2.1	98.1	6879	3729	3717								50.5	22.1	16.0
					150.2	2.1	148.1	6951	3784	3775								152.0	24.3	18.8
					200.1	2.2	197.9	6983	3835	3827								144.0	23.7	21.3
					100.4	2.1	98.2	6920	3789	3779										
					60.2	2.2	58.0	6930	3794	3754								45.0	21.0	14.7
					10.3	2.1	8.3	5914	3435	3424										

Table T1 (continued).

Sample (Leg-Hole-Core-Section-Interval-Orientation)	Depth (mbsf)	Porosity (%)	Bulk density (g/cm ³)	Grain density (g/cm ³)	Pc (MPa)	Pp (MPa)	Ep (MPa)	Vp (m/s)	Vs1 (m/s)	Vs2 (m/s)	Vp Anisotropy	Vs Anisotropy	Vsmax Anisotropy	Qp	Qs1	Qs2						
176-735B-147R-6 (43-45) h'	947.37	0.82	2.93	2.94	9.9	2.2	7.7	6545	3408	3388		0.1										
					20.1	2.1	18.0	6608	3445	3402		0.3										
					40.4	2.1	38.3	6675	3540	3488		0.4										
					60.2	2.1	58.1	6793	3646	3581		0.5						44.8	16.8	14.5		
					80.4	2.1	78.3	6787	3720	3659		0.4										
					100.3	2.1	98.2	6862	3759	3681		0.5						99.3	13.3	15.5		
					150.3	2.1	148.2	6949	3810	3771		0.3						166.0	15.3	21.8		
					200.2	2.1	198.1	6975	3842	3787		0.4						308.0	17.0	24.6		
					100.4	2.1	98.4	6995	3854	3768		0.6										
					60.1	2.2	58.0	6902	3790	3735		0.4						76.1	17.6	15.6		
					10.2	2.1	8.2	6046	3436	3380		0.4										
					176-735B-147R-6 (43-45) h' 45°	947.37	0.82	2.93	2.94	10.1	2.1	8.0	6499	3304	3318		0.1					
										20.1	2.1	18.0	6570	3359	3380		0.2					
39.9	2.2	37.7	6691	3455						3471		0.1										
60.1	2.1	58.0	6861	3562						3586		0.2						32.1	16.4	15.7		
80.1	2.1	78.0	6895	3636						3661		0.2										
100.2	2.1	98.1	6922	3665						3683		0.1						60.7	19.9	19.4		
150.1	2.1	148.0	6984	3736						3765		0.2						167.0	18.0	23.4		
199.9	2.1	197.8	7140	3796						3823		0.2						221.0	17.7	22.8		
100.3	2.1	98.2	7029	3757						3775		0.1										
60.2	2.1	58.1	6957	3723						3752		0.2						43.0	17.5	16.3		
10.2	2.1	8.1	6252	3429						3425		0.0										
176-735B-147R-6 (55-57) h'	947.49	1.09	2.93	2.95						10.1	2.1	7.9	6350	3473	3428		0.3					
										20.1	2.1	18.0	6665	3572	3557		0.1					
					40.2	2.1	38.1	6642	3618	3597		0.1										
					60.2	2.1	58.0	6810	3663	3660		0.0						14.9	14.0	9.4		
					80.3	2.1	78.1	6822	3685	3741		-0.4										
					100.2	2.1	98.1	6783	3682	3744		-0.4						22.8	20.4	10.2		
					150.2	2.1	148.1	6922	3791	3824		-0.2						36.6	35.7	13.1		
					200.0	2.2	197.9	6877	3852	3849		0.0						36.1	36.4	12.9		
					100.4	2.1	98.3	6935	3815	3803		0.1										
					60.3	2.1	58.2	6926	3836	3840		0.0						18.9	18.4	10.7		
					10.2	2.1	8.1	5925	3461	3473		-0.1										
					176-735B-154R-5 (32-34) h'	1010.59	0.96	2.93	2.95	10.1	2.1	8.0	6570	3580	3581	1.9	0.0	0.5				
										20.1	2.1	18.0	6762	3653	3698	2.6	0.3	1.1				
40.0	2.1	37.9	6858	3708						3761	2.0	0.4	1.1									
60.1	2.1	58.0	6907	3790						3832	1.5	0.3	0.9	12.4	10.8	9.6						
80.3	2.1	78.2	6909	3829						3891	0.7	0.4	1.0									
100.2	2.1	98.1	6999	3860						3917	2.4	0.4	1.1	12.9	16.3	12.5						
150.3	2.1	148.2	6983	3881						3932	1.2	0.3	0.9	13.8	15.6	10.7						
200.3	2.1	198.2	7033	3912						3957	0.7	0.3	0.8	13.5	15.4	9.6						
100.4	2.1	98.3	6952	3902						3971	1.2	0.4	1.2									
60.3	2.1	58.2	6982	3889						3910	1.4	0.1	0.8	12.1	11.6	9.9						
10.1	2.1	7.9	6371	3561						3634	3.8	0.5	0.5									
176-735B-154R-5 (42-44) h	1010.69	0.66	2.96	2.97						10.2	2.0	8.2	6443	3449	3459		-0.1					
										20.4	2.0	18.4	6591	3489	3511		-0.2					
					40.2	2.0	38.1	6720	3596	3605		-0.1										
					60.2	2.0	58.2	6804	3697	3710		-0.1						24.7	22.1	13.5		
					80.5	2.0	78.5	6860	3763	3754		0.1										
					100.6	1.9	98.7	6833	3763	3776		-0.1						32.6	20.5	13.5		
					150.2	2.1	148.1	6903	3822	3827		0.0						67.7	22.1	17.5		
					200.1	2.0	198.1	6986	3851	3849		0.0						94.2	22.2	20.1		
					100.3	2.0	98.3	6870	3842	3829		0.1										
					60.2	2.0	58.2	6882	3805	3816		-0.1						24.8	23.9	13.3		
					10.0	2.1	7.9	6130	3509	3541		-0.2										

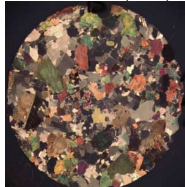


Table T1 (continued).

Sample (Leg-Hole-Core-Section-Interval-Orientation)	Depth (mbsf)	Porosity (%)	Bulk density (g/cm ³)	Grain density (g/cm ³)	Pc (MPa)	Pp (MPa)	Ep (MPa)	Vp (m/s)	Vs1 (m/s)	Vs2 (m/s)	Vp Anisotropy	Vs Anisotropy	Vsmax Anisotropy	Qp	Qs1	Qs2				
176-735B-154R-5 (44-50) v	1010.71	0.81	2.92	2.94	9.9	2.1	7.8	6664	3573	3508			0.5							
					20.0	2.1	17.9	6697	3589	3542				0.3						
					40.0	2.2	37.9	6787	3669	3600										
					60.1	2.1	58.0	6896	3741	3690								22.5	30.1	16.9
					80.2	2.1	78.1	6931	3797	3738										
					100.3	2.1	98.2	6928	3818	3745								23.4	47.5	18.3
					150.2	2.1	148.1	6960	3859	3790								25.8	38.5	20.2
					200.1	2.2	197.9	7009	3894	3839								24.6	35.3	23.2
					100.3	2.1	98.2	6960	3868	3790										
					60.2	2.1	58.1	6965	3846	3789								22.5	35.1	18.1
					10.1	2.2	7.9	6556	3666	3565										
176-735B-158R-4 (65-67) h'	1048.63	0.40	2.96	2.97	10.0	2.1	7.9	6615	3494	3529	4.7	-0.2	0.2							
					19.9	2.1	17.8	6687	3563	3558	5.7	0.0	0.8							
					40.4	2.0	38.4	6606	3626	3598	7.7	0.2	1.5							
					60.2	2.1	58.1	6722	3685	3649	7.9	0.2	1.8	11.1	9.0	9.6				
					80.3	2.1	78.2	6748	3750	3679	7.4	0.5	2.1							
					100.2	2.1	98.1	6751	3759	3671	7.8	0.6	2.3	12.6	10.6	12.9				
					150.3	2.0	148.2	6853	3803	3736	6.8	0.4	2.1	14.4	10.1	15.2				
					200.2	2.0	198.1	6923	3837	3771	5.9	0.4	2.1	16.0	8.4	13.5				
					100.2	2.1	98.1	6804	3770	3744	6.8	0.2	2.1							
					60.2	2.1	58.1	6792	3777	3706	7.3	0.5	2.2	10.7	8.8	10.5				
					10.0	2.1	7.9	6623	3625	3612	-1.6	0.1	-1.3							
176-735B-158R-4 (80-84) v	1048.78	0.83	2.96	2.98	10.1	2.1	8.0	6418	3248	3509			1.9							
					20.0	2.2	17.8	6694	3388	3606				1.6						
					40.1	2.1	37.9	6793	3556	3711				1.1						
					60.2	2.1	58.0	6891	3669	3767				0.7			27.0	12.8	16.0	
					80.2	2.1	78.1	6963	3720	3783				0.4						
					100.3	2.1	98.2	6946	3717	3805				0.6			29.1	15.3	19.4	
					150.2	2.1	148.0	6994	3788	3811				0.2			35.9	18.1	24.3	
					200.1	2.1	198.0	7044	3831	3831				0.0			39.4	15.9	22.6	
					100.4	2.1	98.3	6984	3752	3785				0.2						
					60.3	2.1	58.2	6910	3690	3796				0.7			25.4	12.7	15.5	
					10.1	2.1	8.0	6526	3432	3677				1.7						
176-735B-158R-4 (84-86) h	1048.82	0.90	2.99	3.01	10.0	2.1	7.9	6927	3560	3443			0.8							
					20.1	2.1	18.0	7077	3676	3561				0.8						
					40.1	2.1	38.0	7130	3825	3696				0.9						
					60.1	2.1	58.0	7271	3930	3788				0.9			20.6	10.3	7.7	
					80.1	2.2	78.0	7266	3995	3845				1.0						
					100.3	2.1	98.2	7299	4033	3837				1.2			22.2	13.3	13.1	
					150.3	2.1	148.2	7330	4067	3874				1.2			25.2	13.2	16.5	
					200.4	2.0	198.5	7345	4101	3929				1.1			24.6	12.8	17.5	
					100.1	2.2	98.0	7280	4065	3877				1.2						
					60.1	2.2	57.9	7306	4042	3877				1.0			19.7	10.8	8.6	
					9.9	2.1	7.7	6517	3431	3541				-0.8						
176-735B-179R-5 (90-97) v	1227.35	0.59	2.91	2.92	9.8	2.2	7.7	6641	3569	3570	3.7	0.0	1.8							
					19.9	2.2	17.8	6837	3613	3609	3.1	0.0	1.7							
					40.2	2.1	38.1	6945	3657	3669	2.4	0.1	1.6							
					60.3	2.0	58.3	6965	3699	3709	1.5	0.1	1.8	23.5	13.5	10.4				
					80.2	2.1	78.1	7032	3722	3721	0.3	0.0	1.8							
					100.2	2.1	98.1	7016	3735	3740	0.5	0.0	1.8	31.0	15.6	11.5				
					150.1	2.1	148.0	7044	3773	3766	1.2	0.0	1.7	41.1	13.5	13.5				
					200.1	2.1	198.0	7132	3782	3798	1.6	0.1	1.9	42.1	11.4	12.8				
					100.2	2.2	98.0	7026	3736	3761	1.1	0.2	2.1							
					60.2	2.1	58.2	7003	3715	3731	2.8	0.1	2.2	23.9	13.9	10.3				
					10.2	2.1	8.1	6716	3567	3607	3.0	0.3	1.9							

Table T1 (continued).

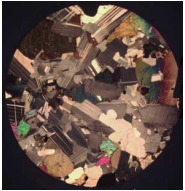

Sample (Leg-Hole-Core-Section-Interval-Orientation)	Depth (mbsf)	Porosity (%)	Bulk density (g/cm ³)	Grain density (g/cm ³)	Pc (MPa)	Pp (MPa)	Ep (MPa)	Vp (m/s)	Vs1 (m/s)	Vs2 (m/s)	Vp Anisotropy	Vs Anisotropy	Vsmax Anisotropy	Qp	Qs1	Qs2				
176-735B-179R-5 (97-99) h 	1227.42	0.64	2.89	2.90	10.1	2.1	8.0	6796	3573	3489		0.6								
					20.1	2.1	18.1	6839	3606	3542		0.4								
					40.0	2.1	37.8	6933	3681	3609		0.5								
					60.2	2.1	58.2	6987	3707	3666		0.3						19.5	13.4	14.1
					80.3	2.0	78.3	7019	3739	3706		0.2								
					100.3	2.1	98.2	7036	3761	3704		0.4						20.7	12.6	14.9
					150.1	2.1	148.0	7056	3787	3746		0.3						26.6	14.1	17.2
					200.0	2.1	197.9	7091	3821	3786		0.2						26.5	14.5	15.2
					100.3	2.1	98.2	7050	3792	3729		0.4								
					60.2	2.1	58.1	7034	3750	3714		0.2						18.7	13.5	14.4
					10.0	2.1	7.9	6630	3628	3580		0.3								
					176-735B-179R-5 (110-112) h' 	1227.55	0.72	2.94	2.96	9.9	2.2	7.8	7052	3836	3722		0.8			
20.1	2.1	17.9	7056	3866						3722		0.9								
40.1	2.1	38.0	7103	3893						3759		0.9								
60.1	2.2	57.9	7096	3969						3802		1.1						14.1	7.9	11.6
80.0	2.2	77.8	7037	4004						3855		0.9								
100.1	2.2	98.0	7070	4009						3832		1.1						16.5	9.1	15.2
150.1	2.2	147.9	7140	4046						3849		1.2						22.6	12.1	22.7
200.0	2.1	197.9	7205	4073						3849		1.4						20.8	12.8	22.1
100.2	2.2	98.0	7125	4065						3832		1.5								
60.1	2.1	58.0	7229	4053						3870		1.2						14.4	8.5	12.4
10.1	2.1	8.0	6829	3849						3722		0.8								
176-735B-190R-4 (67-69) h' 	1330.90	0.73	2.98	2.99						10.0	2.1	7.9	6621	3656	3645	2.3	0.1	1.3		
					20.0	2.1	17.8	6661	3705	3705	2.4	0.0	1.5							
					40.0	2.2	37.9	6758	3780	3758	2.8	0.1	1.9							
					60.3	2.1	58.2	6879	3783	3793	4.0	-0.1	1.8	25.7	14.3	15.2				
					80.6	2.0	78.6	6912	3808	3810	3.7	0.0	1.8							
					100.4	2.0	98.4	6887	3826	3817	2.7	0.1	1.7	53.1	19.5	20.0				
					150.4	2.0	148.3	6976	3880	3876	3.0	0.0	1.8	55.0	28.0	29.0				
					174.0	2.1	171.9	6999	3921	3904		0.1		51.6	28.1	33.5				
					100.6	2.0	98.5	6945	3874	3867	3.7	0.0	2.0							
					60.5	2.0	58.5	6889	3855	3869	4.3	-0.1	2.2	31.0	14.5	14.9				
					10.4	2.1	8.3	6429	3647	3641	-1.3	0.0	1.2							
					176-735B-190R-4 (80-86) v 	1331.03	0.67	2.94	2.95	10.1	2.1	8.0	6594	3585	3564		0.1			
20.1	2.1	17.9	6656	3616						3598		0.1								
40.6	1.9	38.7	6732	3622						3615		0.0								
60.3	2.1	58.1	6757	3644						3643		0.0					64.6	26.8	18.0	
80.3	2.1	78.2	6774	3655						3638		0.1								
100.1	2.2	98.0	6742	3666						3649		0.1						132.0	28.9	19.7
150.3	2.1	148.2	6805	3699						3683		0.1						137.0	30.5	23.2
200.0	2.2	197.8	6848	3725						3704		0.1						106.0	29.7	24.5
100.4	2.1	98.3	6775	3651						3638		0.1								
60.3	2.1	58.2	6726	3633						3627		0.0						59.9	25.9	17.8
10.3	2.1	8.2	6614	3601						3585		0.1								
176-735B-190R-4 (87-89) h 	1331.10	1.25	2.94	2.97						10.0	2.0	8.0	6469	3464	3476		0.1			
					20.2	2.0	18.3	6504	3490	3489		0.0								
					39.9	2.1	37.8	6573	3502	3510		0.1								
					60.1	2.1	58.0	6609	3522	3535		0.1						24.1	16.1	20.2
					80.2	2.1	78.1	6663	3548	3557		0.1								
					100.4	2.0	98.5	6702	3568	3571		0.0						36.1	19.1	21.3
					150.1	2.1	148.0	6770	3606	3615		0.1						40.8	21.6	25.4
					200.0	2.1	197.9	6823	3636	3645		0.1						38.0	22.1	26.7
					100.3	2.1	98.2	6691	3572	3570		0.0								
					60.2	2.1	58.1	6599	3526	3538		0.1						25.2	16.0	19.4
					10.2	2.1	8.1	6516	3482	3487		0.0								

Table T1 (continued).

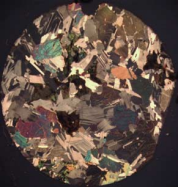
Sample (Leg-Hole-Core-Section-Interval-Orientation)	Depth (mbsf)	Porosity (%)	Bulk density (g/cm ³)	Grain density (g/cm ³)	Pc (MPa)	Pp (MPa)	Ep (MPa)	Vp (m/s)	Vs1 (m/s)	Vs2 (m/s)	Vp Anisotropy	Vs Anisotropy	Vsmax Anisotropy	Qp	Qs1	Qs2				
176-735B-209R-7 (97-99) h'	1497.16	0.89	2.99	3.01	10.1	2.1	7.9	6386	3527	3615	-2.9	0.6	0.2							
					20.3	2.1	18.2	6535	3650	3727	-3.0	0.5	0.6							
					40.3	2.1	38.2	6766	3747	3847	-1.9	0.7	1.0							
					60.3	2.1	58.2	6892	3858	3926	-0.3	0.4	1.4	8.4	4.9	4.7				
					80.1	2.2	77.9	6934	3879	3961	-0.4	0.5	1.6							
					100.2	2.2	98.0	6968	3897	3980	-0.2	0.5	1.6	14.0	6.3	7.7				
					150.3	2.1	148.1	7073	4011	4072	0.3	0.4	2.0	27.1	8.5	8.9				
					200.1	2.1	198.0	7050	4086	4110	0.4	0.1	2.0	38.4	10.4	10.0				
					100.4	2.1	98.3	7050	3951	4044	0.8	0.6	1.9							
					60.3	2.1	58.2	6919	3942	3994	-0.9	0.3	1.6	8.5	5.4	5.2				
					10.1	2.1	8.0	6108	3650	3640	-7.6	-0.1	0.2							
176-735B-209R-7 (100-102) h 	1497.19	0.73	2.99	3.00	10.0	2.1	7.9	6576	3599	3587		0.1								
					20.1	2.1	18.0	6732	3677	3633		0.3								
					40.1	2.1	37.9	6897	3734	3696		0.3								
					60.1	2.1	58.0	6916	3768	3718		0.3						21.3	10.0	12.3
					80.4	2.1	78.3	6965	3784	3716		0.5								
					100.2	2.2	98.1	6982	3809	3729		0.5						28.5	9.6	13.7
					150.0	2.2	147.8	7050	3855	3754		0.7						39.8	11.1	15.5
					200.0	2.2	197.8	7022	3865	3787		0.5						44.0	11.9	16.7
					100.3	2.2	98.1	6993	3792	3753		0.3								
					60.1	2.2	57.9	6980	3792	3750		0.3						23.5	10.6	12.5
					10.1	2.2	7.9	6601	3630	3617		0.1								
176-735B-209R-7 (102-108) v	1497.21	0.89	2.98	3.00	10.0	2.2	7.9	6594	3534	3537		0.0								
					20.0	2.2	17.9	6704	3573	3601		-0.2								
					39.9	2.2	37.7	6790	3655	3633		0.2								
					60.0	2.2	57.8	6907	3703	3684		0.1						19.0	14.1	10.0
					80.2	2.2	78.0	6937	3740	3726		0.1								
					100.3	2.1	98.2	6937	3776	3739		0.2						22.3	14.9	12.2
					150.1	2.1	148.0	6987	3809	3782		0.2						24.9	15.8	15.2
					200.0	2.1	197.9	7028	3848	3828		0.1						24.9	15.0	14.9
					100.2	2.2	98.0	6949	3784	3756		0.2								
					60.2	2.2	58.0	6945	3767	3733		0.2						20.4	14.5	10.4
					10.1	2.1	8.0	6660	3622	3609		0.1								

Table T1 (continued).

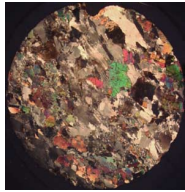
Sample (Leg-Hole-Core-Section-Interval-Orientation)	Depth (mbsf)	Igneous Interval	Lithology	Macroscopic Core Observations					Background alteration (%)
				Plagioclase (%)	Augite (%)	Olivine (%)	Opx/Plag (%)	Opaques (%)	
176-735B-96R-2 (49-51) h'	550.29	524	opx-bearing oxide gabbro	65	35	8	-	0.5	12
176-735B-96R-2 (54-58) v	550.34	524	opx-bearing oxide gabbro	65	35	8	-	0.5	12
176-735B-116R-4 (127-129) h 	677.04	573	opx-bearing gabbro	50	35	3	3	0.7	18
176-735B-116R-4 (129-133) v	677.06	573	opx-bearing gabbro	50	35	3	3	0.7	18
176-735B-116R-5 (7-9) h'	677.27	575	gabbronorite	55	35	1	7	0.8	10

Table T1 (continued).

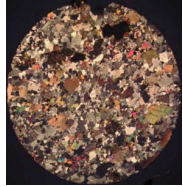
Sample (Leg-Hole-Core-Section-Interval-Orientation)	Depth (mbsf)	Igneous Interval	Lithology	Macroscopic Core Observations					
				Plagioclase (%)	Augite (%)	Olivine (%)	Opx/Plag (%)	Opaques (%)	Background alteration (%)
176-735B-133R-2 (126-128) h'	825.50	662	olivine gabbro	65	35	6	-	0.5	40
176-735B-133R-3 (0-7) v 	825.63	662	olivine gabbro	65	35	6	-	0.5	~60
176-735B-133R-3 (7-9) h	825.70	662	olivine gabbro	65	35	6	-	0.5	~60
176-735B-142R-3 (86-88) h'	896.47	693	olivine gabbro	65	35	8	-	0.5	10
176-735B-142R-3 (86-88) h' 45°	896.47	693	olivine gabbro	65	35	8	-	0.5	10

Table T1 (continued).

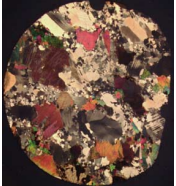
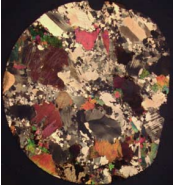
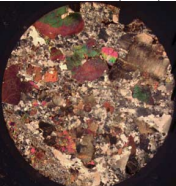
Sample (Leg-Hole-Core-Section-Interval-Orientation)	Depth (mbsf)	Igneous Interval	Lithology	Macroscopic Core Observations					Background alteration (%)
				Plagioclase (%)	Augite (%)	Olivine (%)	Opx/Plag (%)	Opaques (%)	
176-735B-142R-5 (0-6) v	898.44	693	olivine gabbro	65	35	8	-	0.5	12
176-735B-142R-5 (6-8) h 	898.50	693	olivine gabbro	65	35	8	-	0.5	12
176-735B-142R-5 (6-8) h 45° Parallel to foliation 	898.50	693	olivine gabbro	65	35	8	-	0.5	12
176-735B-147R-6 (32-39) v	947.26	710	gabbro	55	30	2	-	0.6	40
176-735B-147R-6 (39-41) h 	947.33	710	gabbro	55	30	2	-	0.6	40

Table T1 (continued).

Sample (Leg-Hole-Core-Section-Interval-Orientation)	Depth (mbsf)	Igneous Interval	Lithology	Macroscopic Core Observations					
				Plagioclase (%)	Augite (%)	Olivine (%)	Opx/Plag (%)	Opaques (%)	Background alteration (%)
176-735B-147R-6 (43-45) h'	947.37	710	gabbro	55	30	2	-	0.6	40
176-735B-147R-6 (43-45) h' 45°	947.37	710	gabbro	55	30	2	-	0.6	40
176-735B-147R-6 (55-57) h'	947.49	710	gabbro	55	30	2	-	0.6	40
176-735B-154R-5 (32-34) h'	1010.59	731	olivine gabbro	65	35	8	-	0.5	8
176-735B-154R-5 (42-44) h'	1010.69	731	olivine gabbro	65	35	8	-	0.5	8



Table T1 (continued).

Sample (Leg-Hole-Core-Section-Interval-Orientation)	Depth (mbsf)	Igneous Interval	Lithology	Macroscopic Core Observations					Background alteration (%)
				Plagioclase (%)	Augite (%)	Olivine (%)	Opx/Plag (%)	Opaques (%)	
176-735B-154R-5 (44-50) v	1010.71	731	olivine gabbro	65	35	8	-	0.5	8
176-735B-158R-4 (65-67) h'	1048.63	768	olivine gabbro	55	35	6	-	0.5	6
176-735B-158R-4 (80-84) v	1048.78	768	olivine gabbro	55	35	6	-	0.5	6
176-735B-158R-4 (84-86) h	1048.82	768	olivine gabbro	55	35	6	-	0.5	6
176-735B-179R-5 (90-97) v	1227.35	845	olivine gabbro	55	25	20	-	0.5	2

Table T1 (continued).

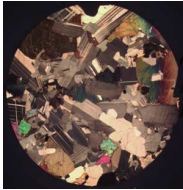

Sample (Leg-Hole-Core-Section-Interval-Orientation)	Depth (mbsf)	Igneous Interval	Lithology	Macroscopic Core Observations					Background alteration (%)
				Plagioclase (%)	Augite (%)	Olivine (%)	Opx/Plag (%)	Opaques (%)	
176-735B-179R-5 (97-99) h 	1227.42	845	olivine gabbro	55	25	20	-	0.5	2
176-735B-179R-5 (110-112) h'	1227.55	845	olivine gabbro	55	25	20	-	0.5	2
176-735B-190R-4 (67-69) h'	1330.90	890	troctolitic gabbro	65	15	12	-	0.7	5
176-735B-190R-4 (80-86) v	1331.03	890	troctolitic gabbro	65	15	12	-	0.7	5
176-735B-190R-4 (87-89) h 	1331.10	890	troctolitic gabbro	65	15	12	-	0.7	5

Table T1 (continued).

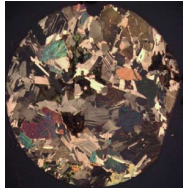
Sample (Leg-Hole-Core-Section-Interval-Orientation)	Depth (mbsf)	Igneous Interval	Lithology	Macroscopic Core Observations					
				Plagioclase (%)	Augite (%)	Olivine (%)	Opx/Plag (%)	Opaques (%)	Background alteration (%)
176-735B-209R-7 (97-99) h'	1497.16	952	olivine gabbro	60	30	10	-	-	3
176-735B-209R-7 (100-102) h	1497.19	952	olivine gabbro	60	30	10	-	-	3
 176-735B-209R-7 (102-108) v	1497.21	952	olivine gabbro	60	30	10	-	-	3

Table T1 (continued).

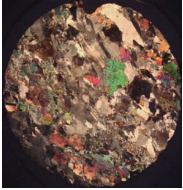
Sample (Leg-Hole-Core-Section-Interval-Orientation)	Depth (mbsf)	Deformation Analysis						Cf	Plag grain size		CPX grain size		OI grain size		OPX grain size	
		Mf intensity	Mf strike	Mf dip	Pf intensity	Pf strike	Pf dip		min (mm)	max (mm)	min (mm)	max (mm)	min (mm)	max (mm)	min (mm)	max (mm)
176-735B-96R-2 (49-51) h'	550.29	2	16	36E	1	0	45E	0	5	30	2	25	1	10		
176-735B-96R-2 (54-58) v	550.34	2	16	36E	1	0	45E	0	5	30	2	25	1	10		
176-735B-116R-4 (127-129) h 	677.04	1	90	42S	1	45	39E	0	10	25	3	25	1	2	1	3
176-735B-116R-4 (129-133) v	677.06	1	90	42S	1	45	39E	0	10	25	3	25	1	2	1	3
176-735B-116R-5 (7-9) h'	677.27	1	12	46E	2	11	37E	0	10	30	3	15	1	2	2	10

Table T1 (continued).

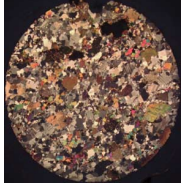
Sample (Leg-Hole-Core-Section-Interval-Orientation)	Depth (mbsf)	Deformation Analysis							Plag grain size		CPX grain size		OI grain size		OPX grain size	
		Mf intensity	Mf strike	Mf dip	Pf intensity	Pf strike	Pf dip	Cf	min (mm)	max (mm)	min (mm)	max (mm)	min (mm)	max (mm)	min (mm)	max (mm)
176-735B-133R-2 (126-128) h'	825.50	1	23	36E	2			0	5	30	2	25	1	3		
176-735B-133R-3 (0-7) v 	825.63	0			2	0	45E	0	5	30	2	25	1	3		
176-735B-133R-3 (7-9) h	825.70	0			2	0	45E	0	5	30	2	25	1	3		
176-735B-142R-3 (86-88) h'	896.47	0			1			0	5	30	2	25	1	10		
176-735B-142R-3 (86-88) h' 45°	896.47	0			1			0	5	30	2	25	1	10		

Table T1 (continued).


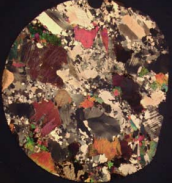
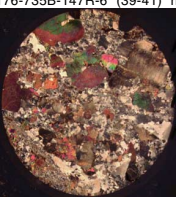
Sample (Leg-Hole-Core-Section-Interval-Orientation)	Depth (mbsf)	Deformation Analysis							Cf	Plag grain size		CPX grain size		Ol grain size		OPX grain size	
		Mf intensity	Mf strike	Mf dip	Pf intensity	Pf strike	Pf dip	min (mm)		max (mm)	min (mm)	max (mm)	min (mm)	max (mm)	min (mm)	max (mm)	
176-735B-142R-5 (0-6) v	898.44	2	16	36E	1	0	45E	0	5	30	2	25	1	10			
176-735B-142R-5 (6-8) h 	898.50	2	16	36E	1	0	45E	0	5	30	2	25	1	10			
176-735B-142R-5 (6-8) h 45° Parallel to foliation 	898.50	2	16	36E	1	0	45E	0	5	30	2	25	1	10			
176-735B-147R-6 (32-39) v	947.26	0			2	0	52E	0	3	20	2	40	1	3			
176-735B-147R-6 (39-41) h 	947.33	0			2	0	52E	0	3	20	2	40	1	3			

Table T1 (continued).

Sample (Leg-Hole-Core-Section-Interval-Orientation)	Depth (mbsf)	Deformation Analysis							Cf	Plag grain size		CPX grain size		Ol grain size		OPX grain size	
		Mf intensity	Mf strike	Mf dip	Pf intensity	Pf strike	Pf dip	min (mm)		max (mm)	min (mm)	max (mm)	min (mm)	max (mm)	min (mm)	max (mm)	
176-735B-147R-6 (43-45) h'	947.37	0			2	0	52E	0	3	20	2	40	1	3			
176-735B-147R-6 (43-45) h' 45°	947.37	0			2	0	52E	0	3	20	2	40	1	3			
176-735B-147R-6 (55-57) h'	947.49	0			2	0	52E	0	3	20	2	40	1	3			
176-735B-154R-5 (32-34) h'	1010.59	2	333	48E	1	350	50E	0	2	15	0.2	25	1	4			
176-735B-154R-5 (42-44) h'	1010.69	2	333	48E	1	350	50E	0	2	15	0.2	25	1	4			



Table T1 (continued).

Sample (Leg-Hole-Core-Section-Interval-Orientation)	Depth (mbsf)	Deformation Analysis						Cf	Plag grain size		CPX grain size		OI grain size		OPX grain size	
		Mf intensity	Mf strike	Mf dip	Pf intensity	Pf strike	Pf dip		min (mm)	max (mm)	min (mm)	max (mm)	min (mm)	max (mm)	min (mm)	max (mm)
176-735B-154R-5 (44-50) v	1010.71	2	333	48E	1	350	50E	0	2	15	0.2	25	1	4		
176-735B-158R-4 (65-67) h'	1048.63	2	5	41E	1	0	45E	0	5	40	0.5	50	1	4		
176-735B-158R-4 (80-84) v	1048.78	0			0			0	5	40	0.5	50	1	4		
176-735B-158R-4 (84-86) h	1048.82	0			0			0	5	40	0.5	50	1	4		
176-735B-179R-5 (90-97) v	1227.35	0			0			0	4	20	6	25	1	10		

Table T1 (continued).

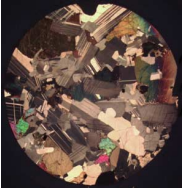
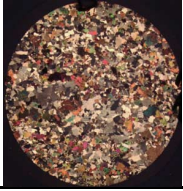
Sample (Leg-Hole-Core-Section-Interval-Orientation)	Depth (mbsf)	Deformation Analysis						Cf	Plag grain size		CPX grain size		OI grain size		OPX grain size	
		Mf intensity	Mf strike	Mf dip	Pf intensity	Pf strike	Pf dip		min (mm)	max (mm)	min (mm)	max (mm)	min (mm)	max (mm)	min (mm)	max (mm)
176-735B-179R-5 (97-99) h 	1227.42	0			0			0	4	20	6	25	1	10		
176-735B-179R-5 (110-112) h'	1227.55	0			0			0	4	20	6	25	1	10		
176-735B-190R-4 (67-69) h'	1330.90	1(2)	0	45E	1	0	50E	0	3	20	0.2	12	1	3		
176-735B-190R-4 (80-86) v	1331.03	1(2)	0	45E	1	0	50E	0	3	20	0.2	12	1	3		
176-735B-190R-4 (87-89) h 	1331.10	1(2)	0	45E	1	0	50E	0	3	20	0.2	12	1	3		

Table T1 (continued).

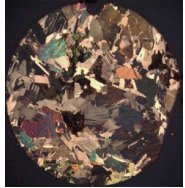
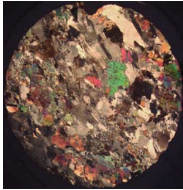
Sample (Leg-Hole-Core-Section-Interval-Orientation)	Depth (mbsf)	Deformation Analysis							Cf	Plag grain size		CPX grain size		Ol grain size		OPX grain size	
		Mf intensity	Mf strike	Mf dip	Pf intensity	Pf strike	Pf dip	min (mm)		max (mm)	min (mm)	max (mm)	min (mm)	max (mm)	min (mm)	max (mm)	
176-735B-209R-7 (97-99) h'	1497.16	0			0			0	5	25	5	30	1	8			
176-735B-209R-7 (100-102) h	1497.19	0			0			0	5	25	5	30	1	8			
 176-735B-209R-7 (102-108) v	1497.21	0			0			0	5	25	5	30	1	8			

Table T1 (continued).

Sample (Leg-Hole-Core-Section-Interval-Orientation)	Depth (mbsf)
176-735B-96R-2 (49-51) h'	550.29
176-735B-96R-2 (54-58) v	550.34
176-735B-116R-4 (127-129) h 	677.04
176-735B-116R-4 (129-133) v	677.06
176-735B-116R-5 (7-9) h'	677.27

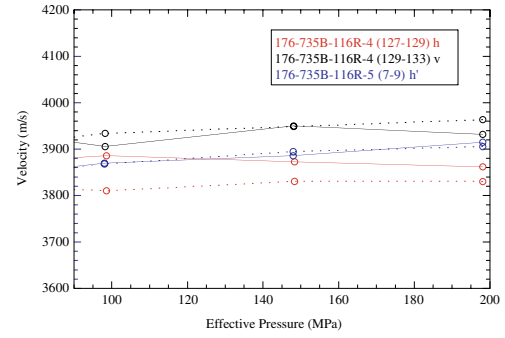
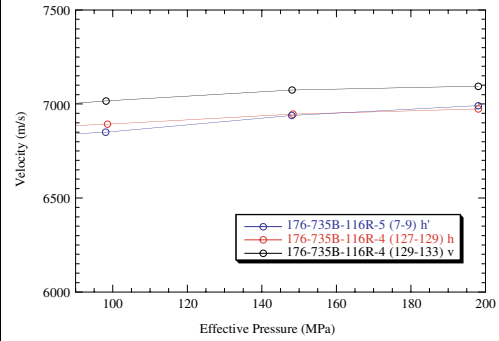
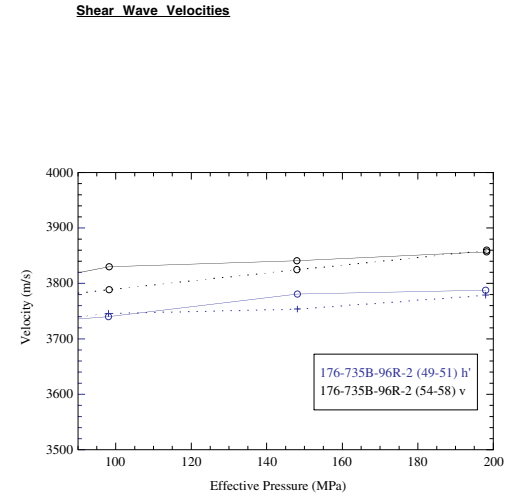
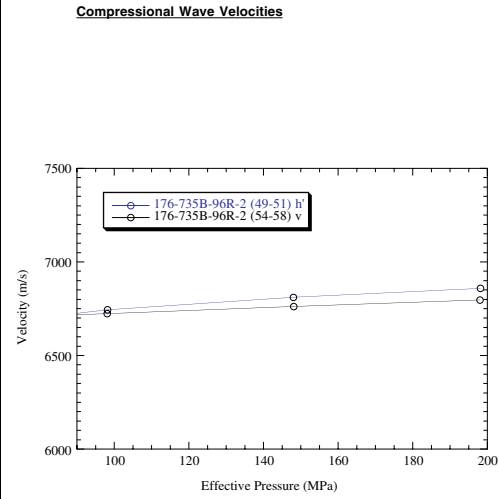
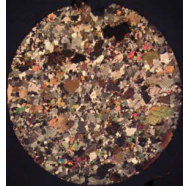
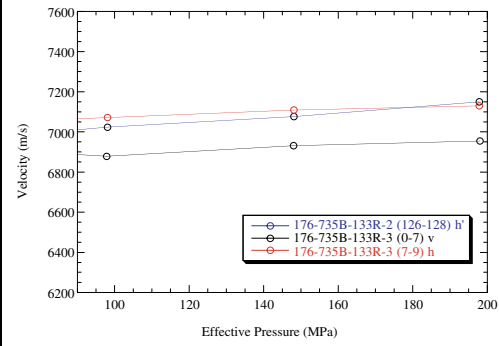


Table T1 (continued).

Sample (Leg-Hole-Core-Section-Interval-Orientation)	Depth (mbsf)
176-735B-133R-2 (126-128) h'	825.50
176-735B-133R-3 (0-7) v 	825.63
176-735B-133R-3 (7-9) h	825.70
176-735B-142R-3 (86-88) h'	896.47
176-735B-142R-3 (86-88) h' 45°	896.47

Compressional Wave Velocities



Shear Wave Velocities

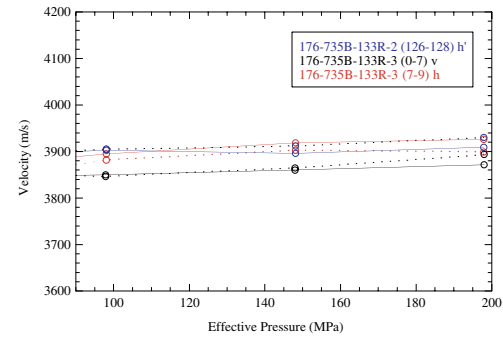
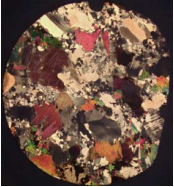
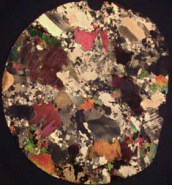
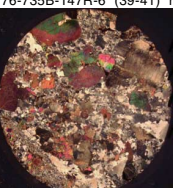
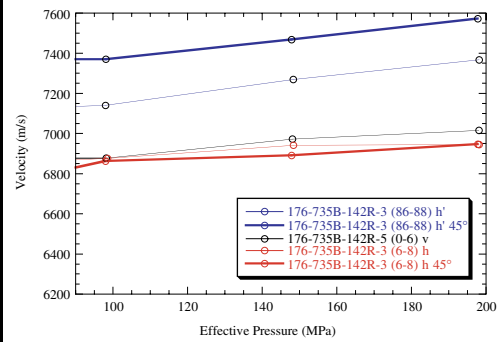


Table T1 (continued).

Sample (Leg-Hole-Core-Section-Interval-Orientation)	Depth (mbsf)
176-735B-142R-5 (0-6) v	898.44
176-735B-142R-5 (6-8) h 	898.50
176-735B-142R-5 (6-8) h 45° Parallel to foliation 	898.50
176-735B-147R-6 (32-39) v	947.26
176-735B-147R-6 (39-41) h 	947.33

Compressional Wave Velocities



Shear Wave Velocities

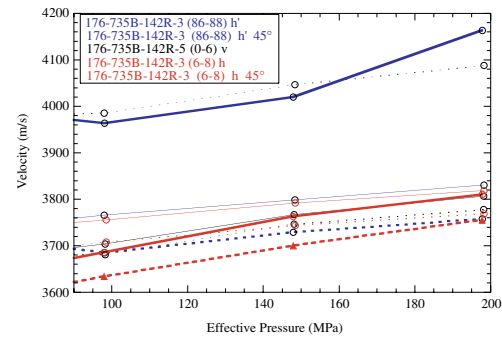
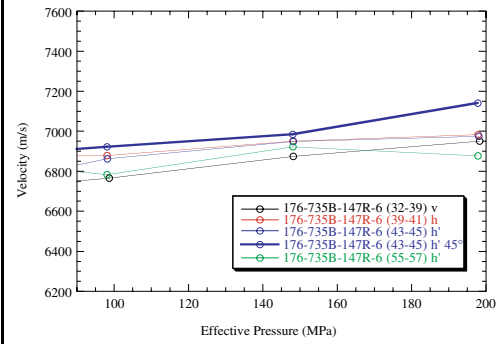


Table T1 (continued).

Sample (Leg-Hole-Core-Section-Interval-Orientation)	Depth (mbsf)
176-735B-147R-6 (43-45) h'	947.37
176-735B-147R-6 (43-45) h' 45°	947.37
176-735B-147R-6 (55-57) h'	947.49
176-735B-154R-5 (32-34) h'	1010.59
176-735B-154R-5 (42-44) h'	1010.69



Compressional Wave Velocities



Shear Wave Velocities

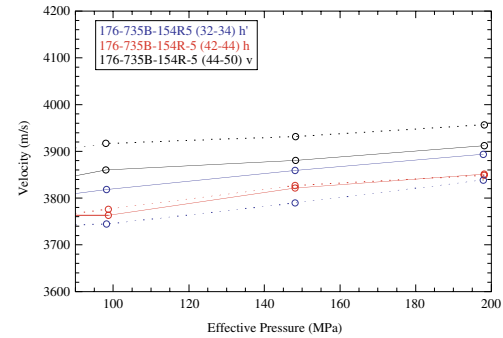
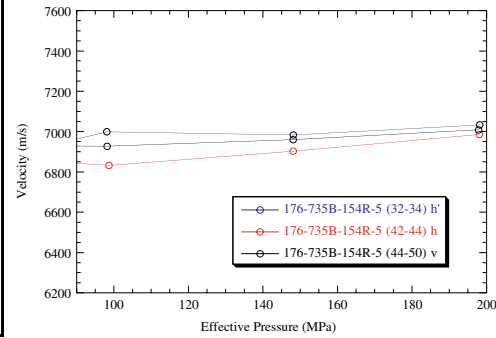
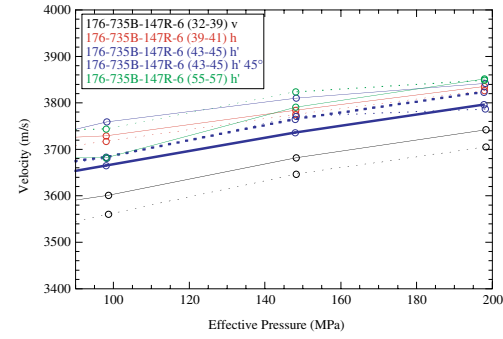
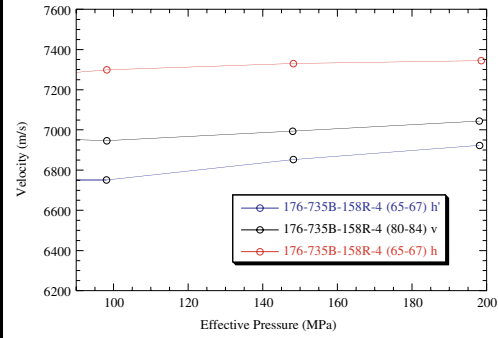


Table T1 (continued).

Sample (Leg-Hole-Core-Section-Interval-Orientation)	Depth (mbsf)
176-735B-154R-5 (44-50) v	1010.71
176-735B-158R-4 (65-67) h'	1048.63
176-735B-158R-4 (80-84) v	1048.78
176-735B-158R-4 (84-86) h	1048.82
176-735B-179R-5 (90-97) v	1227.35

Compressional Wave Velocities



Shear Wave Velocities

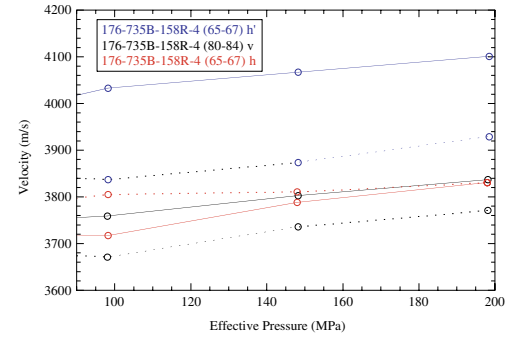
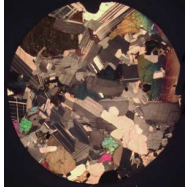
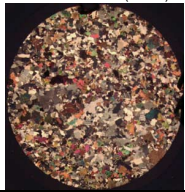
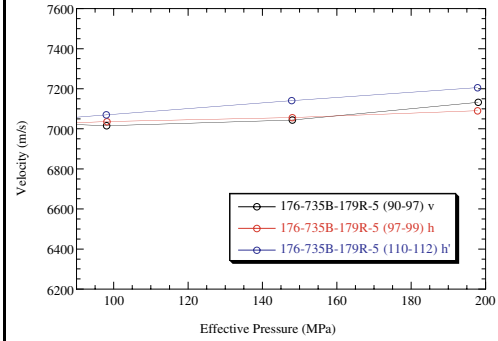


Table T1 (continued).

Sample (Leg-Hole-Core-Section-Interval-Orientation)	Depth (mbsf)
176-735B-179R-5 (97-99) h 	1227.42
176-735B-179R-5 (110-112) h'	1227.55
176-735B-190R-4 (67-69) h'	1330.90
176-735B-190R-4 (80-86) v	1331.03
176-735B-190R-4 (87-89) h 	1331.10

Compressional Wave Velocities



Shear Wave Velocities

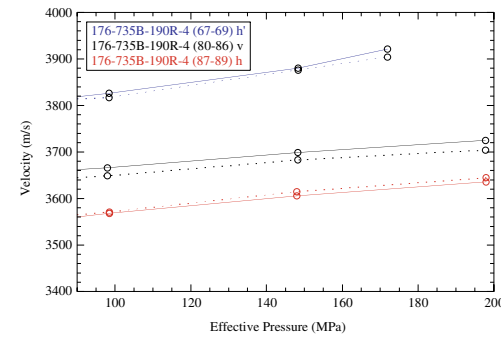
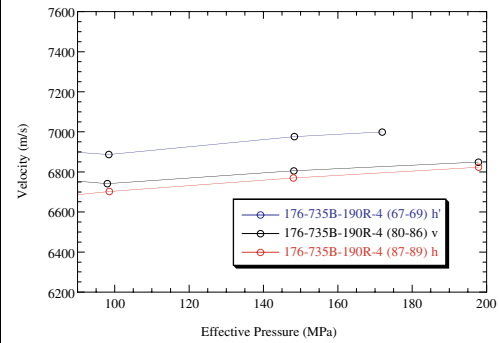
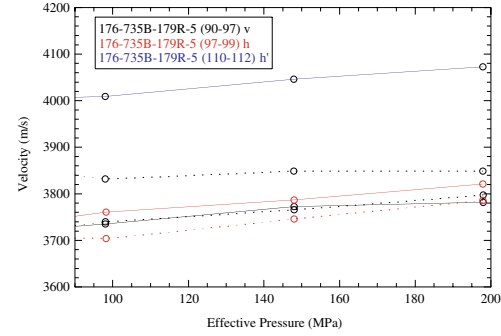
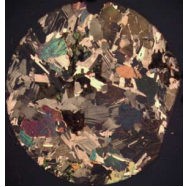
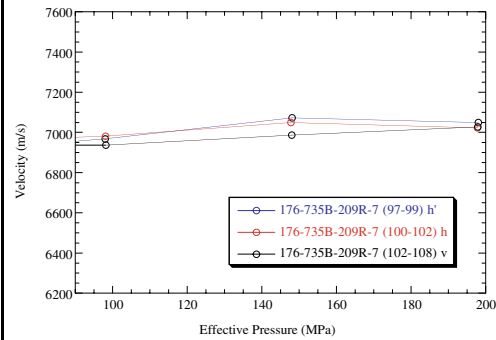


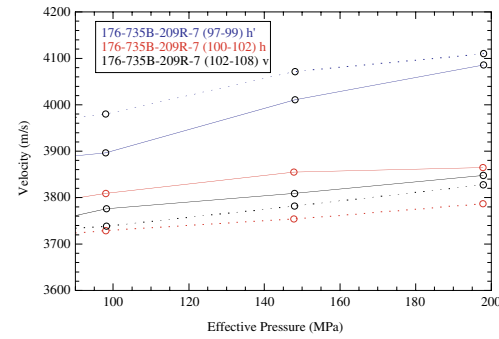
Table T1 (continued).

Sample (Leg-Hole-Core-Section-Interval-Orientation)	Depth (mbsf)
176-735B-209R-7 (97-99) h'	1497.16
176-735B-209R-7 (100-102) h 	1497.19
176-735B-209R-7 (102-108) v	1497.21

Compressional Wave Velocities



Shear Wave Velocities



V_{S1} for the h' (blue), h (red), and v (black) orientations are represented by solid lines.
 V_{S2} for the same orientations are shown as dashed lines.

Notes:

P_c = confining pressure; P_p = pore pressure; E_p = effective pressure = $(P_c - P_p)$; V_p = compressional wave velocity; V_{S1} and V_{S2} = shear wave velocity polarized according to description below and in Appendix;
 Q_p = compressional wave attenuation; Q_{S1} = attenuation of S1; Q_{S2} = attenuation of S2; v= vertically oriented sample (see Appendix); h = horizontally oriented sample and perpendicular to the core cut face (see Appendix); h' = horizontally oriented sample and parallel to the core cut face (see Appendix).

In vertical samples V_{S1} was polarized perpendicular to the cut face (V_{S2} is always 90 degrees from V_{S1}); for horizontal cores, V_{S1} was horizontally polarized and V_{S2} was polarized vertically; 45° = polarized at 45 degrees from conventional measurements (in most cases is parallel to foliation).

$$V_p \text{ Anisotropy} = [(V_{pmax} - V_{pmin}) / (V_{pavg})] * 100 \text{ at } 200 \text{ MPa}$$

$$V_S \text{ Anisotropy} = [(V_{Smax} - V_{Smin}) / (V_{Savg})] * 100 \text{ at } 200 \text{ MPa for one sample only}$$

$$V_{Smax} \text{ Anisotropy} = [(V_{Smax} - V_{Smin}) / (V_{Savg})] * 100 \text{ at } 200 \text{ MPa for all samples in a core (9.5-m section)}$$

Plag = plagioclase; CPX = clinopyroxene

OPX = orthopyroxene; Ol = olivine

The deformation analysis follows the criteria described in the explanatory notes section of Dick, Natland, Miller, et al., 1999.

Mf = Magmatic Fabrics
Pf = Crystal-Plastic Fabrics
Cf = Cataclastic fabric

Magmatic Intensity Scale:
0 = Isotropic; no shape fabric
1 = Weak shape fabric
2 = Moderate shape fabric
3 = Strong shape fabric

Crystal-Plastic Intensity Scale:
0 = Undeformed
1 = Weakly foliated
2 = Strongly foliated
3 = Porphyroclastic (proto-mylonite)
4 = Mylonite
5 = Ultramylonite

Cataclastic Intensity Scale:
0 = Undeformed
1 = Minor fracturing; no significant grain-size reduction
2 = Moderate fracturing; no significant grain-size reduction
3 = Dense anastomosing fracturing and incipient breccia (<20% matrix)
4 = Well-developed fault brecciation; rotation of clasts (20% to 70% matrix)
5 = Cataclasite (>70% matrix)

Table T2. Statistical analyses of Q_p , Q_{S1} , and Q_{S2} measurements for samples collected during Leg 176.

	Q_p	Q_{S1}	Q_{S2}
Points	30 (24)	33	33
Min	8 (8)	71.8	42.2
Max	308 (94.2)	8.4	8.2
Mean	64.3 (35.1)	22	21
Median	38.9 (35.7)	18.8	22.6
Standard deviation	69 (20.1)	12.7	7.9
Standard error	12.6 (4.1)	2.2	1.4

Notes: Mean = $\bar{x} = \frac{1}{n} \sum_{i=1}^n x_i$

$$\text{Standard deviation} = \sqrt{\frac{\sum_{i=1}^n x_i^2 - n(\bar{x})^2}{n-1}}$$

$$\text{Standard error} = \frac{\text{Standard Deviation}}{\sqrt{n}}$$

Statistics based on Q measured at 200 MPa confining pressure. Statistics in parenthesis for Q_p are based on values less than 100. Sampling interval is from 600 to 1500 mbsf.

Table T3. Average core and log measurements, Hole 735B.

	Interval (mbsf)	Density (g/cm ³)	Porosity (%)	V _p [*]	V _s [†]	V _{s1} [*]	V _{s2} [*]
Logging data	0–600	2.88 ± 0.14	3.2 ± 5.2	6520 ± 418	3518 ± 393	—	—
Core data	0–500	2.96 ± 0.11 (84)	0.64 ± 0.67 (60)	6895 ± 307 (84)	3840 ± 142 (36)	3851 ± 129 (27)	3807 ± 180 (9)
	0–500	2.96 ± 0.11 (84)	0.64 ± 0.67 (60)	6895 ± 307 (84)	3840 ± 142 (36)	3851 ± 129 (27)	3807 ± 180 (9)
	0–1500	2.95 ± 0.10 (117)	0.70 ± 0.55 (93)	6819 ± 937 (117)	3850 ± 118 (102)	3862 ± 117 (60)	3834 ± 119 (42)

Notes: * = laboratory velocity measurements averaged at 200 MPa confining pressure. † = average of V_{s1} and V_{s2} at 200 MPa for laboratory samples. For logs it represents the average V_s from the Dipole Sonic Imager. Number in parentheses represents the number of samples used to calculate the mean and standard deviation values. Sampling interval for logging tools is 0.15 cm.